2-1-2012

Engineered quantum dots for infrared photodetectors

Jiayi Shao

Jiayi Shao
_____
Candidate

Electrical and Computer Engineering
_____
Department

This dissertation is approved, and it is acceptable in quality and form for publication:

Approved by the Dissertation Committee:

Prof. Sanjay Krishna   , Chairperson
_____

Prof. Luke F. Lester
_____

Prof. Majeed M. Hayat
_____

Prof. Mansoor Sheik-Bahae
_____

_____

_____

_____

_____

ENGINEERED QUANTUM DOTS FOR INFRARED PHOTODETECTORS

by

JIAYI SHAO

M.S., Engineering
University of New Mexico

DISSERTATION

Submitted in Partial Fulfillment of the
Requirements for the Degree of

**Doctor of Philosophy
Engineering**

The University of New Mexico
Albuquerque, New Mexico

December 2011

DEDICATION

This dissertation would not have been possible without the love, moral support and encouragement of my husband, Chun Wang, my daughter, Anna, and my son, Joshua.

ACKNOWLEDGEMENTS

ENGINEERED QUANTUM DOTS FOR INFRARED
PHOTODETECTORS

by

JIAYI SHAO

M.S., Engineering
University of New Mexico

ADSTRACT OF DISSERTATION

Submitted in Partial Fulfillment of the
Requirements for the Degree of

Doctor of Philosophy
Engineering

The University of New Mexico
Albuquerque, New Mexico

December 2011

ENGINEERED QUANTUM DOT FOR INFRARED PHOTODETECTOR

by

JIAYI SHAO

B.A., Electrical Engineering, Beijing Polytechnic University, 1996

M.S., Electrical Engineering, University of New Mexico, 2006

ABSTRACT

Quantum Dot Infrared Photodetector (QDIP) Focal Plane Arrays (FPAs) have been proposed as an alternative technology for the 3rd generation FPAs. QDIPs are emerging as a competitive technology for infrared detection and imaging especially in the midwave infrared (MWIR) and longwave infrared (LWIR) regime. These detectors are based on intersubband transitions in self-assembled InAs quantum dots (QDs) and offer several advantages such as normal incidence detection, low dark currents and high operating temperatures, while enjoying all the benefits of a mature GaAs fabrication technology. However, due to Stranski-Krastanov (SK) growth mode and the subsequent capping growth, the conventional SK QDs are "pancake shaped" with small height to base ratio due to interface diffusion. Thus they cannot fully exploit the 3D "artificial atom" properties. This dissertation work investigates two approaches for shape engineered QDs: (1) Selective capping techniques of Stranski-Krastanov QDs, and (2) Growth of Sub-Monolayer (SML) QDs. Using Molecular Beam Epitaxy (MBE) growth, engineered QDs have been demonstrated with improved dot geometry and 3D quantum confinement to more closely resemble the 3D "artificial atom". In SK-QDs, the results have demonstrated an increased dot height to base aspect ratio of 0.67 compared with 0.23 for conventional SK-QD using Transmission Electron Microscope (TEM) images, enhanced s-to-p polarized spectral response ratio of 37% compared with 10% for conventional SK-QD, and improved SK-QDIP characterization such as: high operating

temperature of 150K under background-limited infrared photodetection (BLIP) condition, photodetectivity of 1×10^9 cmHz$^{1/2}$/W at 77K for a peak wavelength of 4.8 μm, and photoconductive gain of 100 (V_b=12V) at 77 K. In SML-QDs, we have demonstrated dots with a small base width of 4~6 nm, height of 8 nm, absence of wetting layer and advantage optical property than the SK-QDs. SML-QD shows adjustable dot height to base aspect ratio of 8nm/6nm, increased s-to-p polarized spectral response ratio of 33%, and a narrower full width at half maximum (FWHM), long wavelength 10.5 μm bound-to-bound intersubband transition, and higher responsivity of 1.2 A/W at -2.2 V at 77K and detectivity of 4×10^9 cmHz$^{1/2}$/W at 0.4 V 77K.

TABLE OF CONTENTS

LIST OF FIGURES

LIST OF TABLES

Chapter 1 INTRODUCTION

Introduction

The applications for infrared Focal Plane Array (FPA) IR imaging systems have been developed into three distinct generations: in the 1st generation, linear arrays for scanning systems were demonstrated; in the 2nd generation, two-dimensional arrays for staring systems were developed; in the 3rd generation, the main requirements are enhanced capabilities such as the non-cryogenic operation temperature, good uniformity, low cost, larger number of pixels, higher frame rates, better thermal resolution, multicolor functionality, and/or on-chip signal-processing functions. Quantum Dot Infrared Photodetecctors (QDIPs) FPAs have been proposed as a competitive technology for the 3rd generation FPAs. They are based on intersubband transitions in self-assembled InAs quantum dots (QDs) and offer several advantages such as normal incidence detection, low dark currents and high operating temperatures, high detectivity, while enjoying all the benefits of a mature GaAs fabrication technology. However, due to Stranski-Krastanov (SK) growth technology and the subsequent capping growth, conventional SK QDs are pancake shaped with a small height to base ratio and interface diffusion inhibiting full exploitation of the 3D "artificial atom". This dissertation work investigates two approaches for shape engineered QDs: (1) Selective capping techniques of Stranski-Krastanov QDs, and (2) Sub-Monolayer (SML) QDs in Molecular Beam Epitaxy (MBE) growth to engineer the dot geometry and 3D quantum confinement to resemble more closely a 3D "artificial atom". The results have demonstrated an increased dot height to base aspect ratio using Transmission Electron Microscope (TEM) images, enhanced s-to-p polarized spectral response ratio, and improved QDIP characterization such as: high operating temperature, photodetectivity and photoconductive gain. Moreover, SML-QDs with a smaller base width, adjustable height, and attractive optical properties offers an alternative novel technology in the QDIPs.

The layout of dissertation is as follows:

In Chapter 1, the general concepts of electromagnetic radiation and infrared detection are introduced. Different types of infrared detectors and competing technologies and their advantages/disadvantages are covered. Pros and cons of competitive technologies for

1

focal plane array (FPA) based on mercury cadmium telluride (MCT), InSb, InAs/InSb type II superlattice, Quantum Well Infrared Photodetector (QWIP) and Quantum Dot Infrared Photodetector (QDIP) are presented and analyzed. The concept of QDs, formation of self-assembled SK-QDs and SML-QDs, and Dot-in-a-well (DWELL) QDIP are introduced. Finally, the objective and contribution of this dissertation is described.

In Chapter 2, a variety of characterization techniques utilized in this work are described. To thoroughly understand the operating principle of the device and be able to design detectors with required characteristics, a lot of information about material and detector properties has to be available, beginning with parameters of as-grown material in Molecular Beam Epitaxy (MBE) growth and ending with characteristics of detector performance. We have characterized structural, optical and morphological properties of as-grown material using Photoluminescence (PL), Atomic Force Microscopy (AFM), Transmission Electron Microscopy (TEM)/Scanning Transmission Electron Microscopy (STEM), X-ray diffraction measurement (XRD) and polarized spectral response techniques, respectively. The electrical behavior of processed detectors was investigated with current-voltage measurements. Detector performance also was characterized using spectral response, responsivity and detectivity measurements.

In Chapter 3, the improvement in the operating temperature and the s-to-p ratio of the polarized spectral response in an engineered Stranski-Krastanov quantum dot-in-a-well- (DWELL) based infrared photodetector are demonstrated. This improvement was achieved through engineering the dot geometry and the quantum confinement via post growth capping of QDs with select overlying materials under various growth conditions. The effect of the capping procedures was determined by examining the optical properties of the QDs such as photoluminescence and the s-to-p ratio of the polarized spectral response in the QDIP detector, and structural properties of the QDs such as AFM and TEM. The results show the InAs QD with the $In_{.15}Al_{.1}Ga_{.75}As$ quaternary well has the best over all performance. By examining the dot geometry using TEM, the TEM image shows a quantum dot with a reduced base of 12 nm and an increased height of 8 nm. Therefore the dot height to base aspect ratio is increased to 0.67, which is much higher than the conventional SK dot with the aspect ratio of 0.25 (with height 4 nm/ base 20 nm). The ratio of s-polarization (TE) to p-polarization (TM) 45° facet side incidence

2

spectral photoresponse increases to 37% from 10% in a DWELL based infrared photodetector. These engineered QDs in a Well were then introduced into the active region of a DWELL IR photodetector. This detector worked at high BLIP operating temperature of 150K, with a peak photodetectivity of 1×10^9 cmHz$^{1/2}$/W at 77K for a peak wavelength of 4.8 μm, and 7.2×10^7 cmHz$^{1/2}$/W at 250K for a peak wavelength of 3.2 μm. The dark current density is as low as 6.3×10^{-7} A/cm^2 (V_b=7V) and 2×10^{-4} A/cm^2 (V_b=12V) at 77 K, and the photocurrent gain is 100 (V_b=12V) at 77 K.

In Chapter 4, the optimization of the growth condition of the Sub-Monolayer QD QDIP detectors is demonstrated. In contrast to "pancake-shaped" SK QDs, the "cylinder-shaped" SML QDs have several advantages including small base diameter, better 3-D quantum confinement, high dot density, adjustable height of the dot geometry, controllable aspect ratio, and the absence of the wetting layer.

There are three approaches for shape engineered SML QDIP explored in this work.

For the first approach in Section 4.1, the InAs/InGaAs SML QDs were formed as 2 layers of 0.5 ML InAs evenly embedded in 5.1 nm GaAs quantum well, and the growth temperature is changed from 460 °C to 540 °C. The growth temperature effects to the Indium interface diffusion, dot geometry, 3D quantum confinement, and strain distribution in the whole system. By examining the dot geometry using TEM, the SML-QDs grown at 460 °C have a small base diameter of 6 nm. When grown at 540 °C, the SML-QDs have a large base diameter of 30 nm. The XRD RADS simulation shows the latter's structural property is similar to that of a QWIP. The results of the s/p polarization spectral response ratio and the dot geometry height to base aspect ratio corroborate with each other. The SML-QD detector grown at 480 °C has a small base diameter of 6 nm, and has the highest s/p ratio of 9% in this study. The SML-QD detector grown at 540 °C has the largest base diameter of 30 nm, and has the low s/p ratio less than 1%. At 77K, #2916 (grown at 540 °C) had the highest responsivity of 0.40 A/W, and the highest detectivity of 5×10^8 cmHz$^{1/2}$/W at 0.25 V for a peak wavelength of 10.3 μm. These results are due to the GaAs Quantum Well (QW) requires the high growth temperature for the high crystal quality, low defect density, and improved optical absorption, even the dot has a large base diameter, significant interface diffusion between dot and the surrounding QW material.

For the second approach described in Section 4.2, the InAs/InGaAs SML QDs were formed as 2 layers of 0.5 ML InAs evenly embedded in 5.1 nm $In_{.1}Ga_{.9}As$ quantum well, and the growth temperature is kept as 500°C. The $In_{.1}Ga_{.9}As$ quantum well prevented the Indium interface diffusion, improved the quantum confinement, and the full width at half maximum (FWHM) is narrower than the first approach.

For the third approach described in Section 4.3, the InAs/InGaAs SML QDs were formed as 4 layers of 0.3 ML InAs evenly embedded in 5.1 nm $In_{.15}Ga_{.85}As$ quantum well, and the growth temperature is kept as 500°C. The SML-QD has the small base diameter of 4 nm and height of 5nm, and the s/p ratio of spectral response has increased to 33%. This SML-QD QDIP have improved 3D quantum confinement, and better detector performance.

In Chapter 5, conclusion and future work of this dissertation are discussed.

1.1 Introduction to Infrared Radiation

All objects with a temperature higher then 0 Kelvin have thermal energy. Since electrons and protons are charged particles and constituents of atoms, all atoms can emit and absorb light energy. The emitted energy is an electromagnetic wave with certain wavelength and/or polarization. If the electromagnetic wave emitted from the object can be measured, the characterization of the object such as material, temperature, i.e. can be known. Infrared (IR) radiation is a form of radiated electromagnetic energy, obeying the same laws as those for Gamma ray, X-ray, ultraviolet, visible light, microwave, and radio waves, but with different wavelength that is shown in figure 1.1 [1].

A description of the radiation spectrum from the source is not complete without knowing the media of propagation of electromagnetic radiation. The spectral transmittance of IR radiation in atmosphere is shown in Figure 1.1. The high transmission bands are called atmospheric windows that are comparatively transparent from 3 to 5 μm and 8 to 13 μm region and are commonly used by IR detectors. Windows in atmospheric absorption are used to classify IR radiation in the following manner: Near Infrared Radiation (NIR) corresponding to wavelengths from 0.7 to 1.5 μm; Short Wavelength Infrared Radiation (SWIR) corresponding to wavelengths from 1.5 to 2.5 μm; Medium Wavelength Infrared Radiation (MWIR) corresponding to wavelengths from 3 to 5 μm;

Long Wavelength Infrared radiation (LWIR) corresponding to wavelengths from 8 to 12 μm; Very Long Wavelength Infrared radiation (VLWIR) corresponding to wavelengths from 12 to about 32 μm.

The radiant flux of a "glowing body" is selectively absorbed by the gaseous constituents of the atmosphere. Water vapor, carbon dioxide, and ozone are the most significant absorbers for each absorption band. Infrared radiation in several regions between 1 and 3 μm, and 6.3 μm is absorbed by water vapor. Strong absorption in the neighborhood of 2.7, 4.3, and 15 μm is mainly due to carbon dioxide. Ozone has an absorption band in the 9.6 μm region.
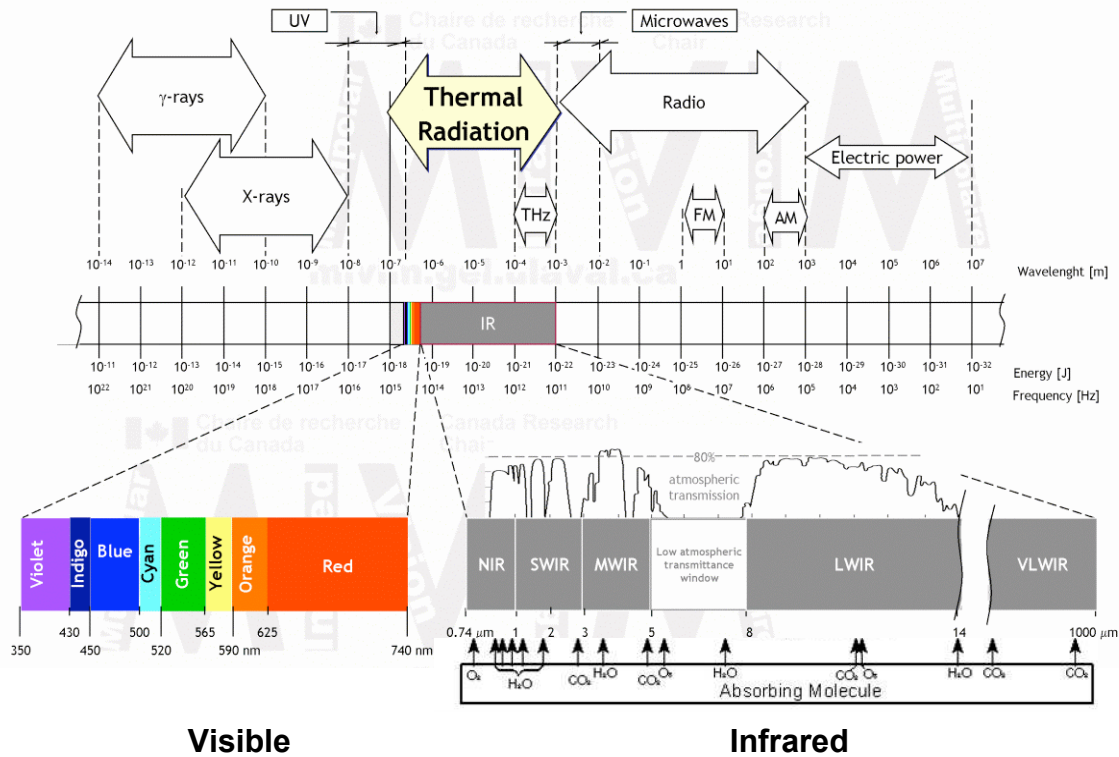
Figure 1.1: The Electromagnetic Spectrum with Transmission of Infrared Spectrum in atmosphere

1.2 Concept of Black Body Radiation

A Black Body (BB) is an idealized body that is a perfect absorber and radiator of electromagnetic radiation. The black body radiation was first accurately described empirically by Max Planck in 1900. It is the relationship between the temperature and the

distribution of emission wavelength. BB laws are applicable to real objects by introducing a parameter called "emissivity", which is the ratio of the spectral exitance of the source to that of a blackbody of the same temperature and can be written as equation 1.1:

$$\varepsilon(\lambda,T) = \frac{M_\lambda(\lambda,T)_{source}}{M_\lambda(\lambda,T)_{blackbody}} \tag{1.1}$$

Generally, emissivity is a function of wavelength and temperature. A true black body would have an $\varepsilon = 1$ while any real object would have $\varepsilon < 1$.

There are three main laws describing BB radiation:

1.2.1 Planck's law

The Planck's law [2] describes probability distribution of emitted wavelengths at a given temperature from a black body in a cavity in the thermodynamic equilibrium and can be written as equation 1.2:

$$W(\lambda,T) \equiv \frac{2hc^2}{\lambda^5} \cdot \frac{1}{e^{\frac{hc}{\lambda kT}} - 1} \tag{1.2}$$

where h is the Planck's constant, k is the Boltzmann's constant and c is the speed of light. Units of $W(\lambda, T)$ are $(W/m^2 \mu m\ sr)$. Blackbody radiation versus temperature plot is shown in Figure 1.2 [3]. It is inferred from the figure that lower temperatures require measurements at longer wavelengths. For the BB at ambient temperature (300K) the great part of spectral emittance is located in the infrared region whereas for the BB at high temperature (1000K or 5000K) the predominant part of spectrum is located in the visible region.

The consequence of Planck's Law is that energy is not continuous, but rather has discrete values or quanta. This phenomenon initiated the development of quantum physics. Today, it is understood that every object emits radiation proportional to its temperature because of atomic oscillations. Most simply, the hotter the object, the faster the frequency of the atoms oscillations and therefore the higher the frequency of radiation emitted by the object.
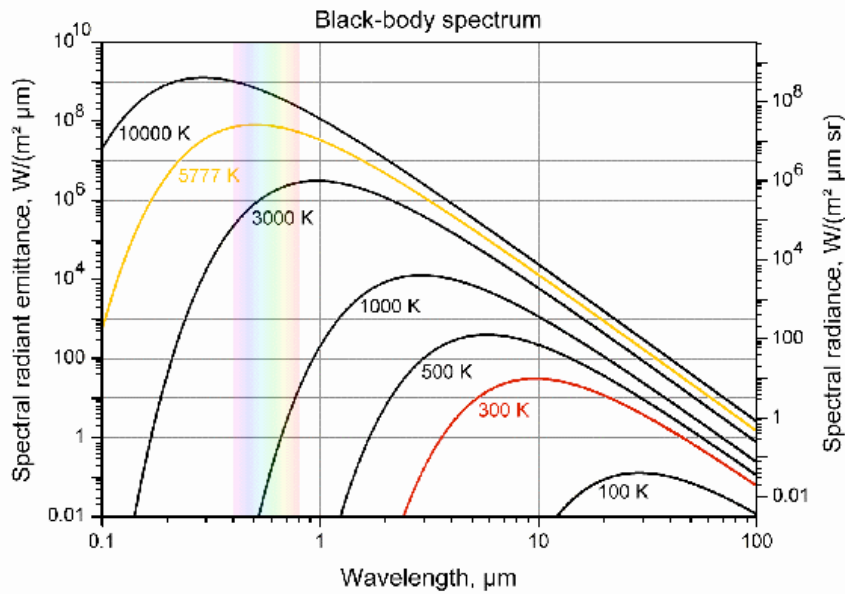
Figure 1.2: Black-body spectrum for temperatures between 100 K and 10000 K in a log-log diagram.

1.2.2 Wien's law

Wien's law [4] at equation 1.3 states a relationship between the temperature T of a black body and wavelength λ_{max} at which the intensity of the radiation it produces is a maximum.

$$\lambda_{max} = \frac{b}{T} \qquad (1.3)$$

where the constant b known as Wien's displacement constant, is equal to 2.8977685×10^{-3} m·K. The peak of the Planck's function moves to shorter wavelengths with increasing temperature.

1.2.3 Stefan-Boltzmann Law

The total power per unit area of the surface radiated by a blackbody at temperature T is given by equation 1.4 [4]

$$j^* = \sigma T^4 \qquad (1.4)$$

7

where $j*$ is the total power radiated per unit area, σ is the Stefan-Boltzmann constant (5.67×10^{-8} W/m^{2}K^4).

1.3 Infrared Detectors

Infrared (IR) detectors convert incident electromagnetic radiation energy falling upon it into a measurable electrical output (current or voltage). IR detectors fall into two broad categories, namely thermal and photon.

1.3.1 Thermal detector

Thermal detectors respond to the heat generated by the absorbed energy of the optical radiation. The temperature change of the device produced by the absorbed energy induces a change in physical or electrical properties of the device that can be measured. This parameter change can be detected by external instrumentation. The thermal effects are generally wavelength independent (shown as Figure 1.3) since it depends upon the radiant power but not upon the photon nature of the incident radiation. Therefore, the spectral dependence is directly related to the emissivity. Generally, the wavelength
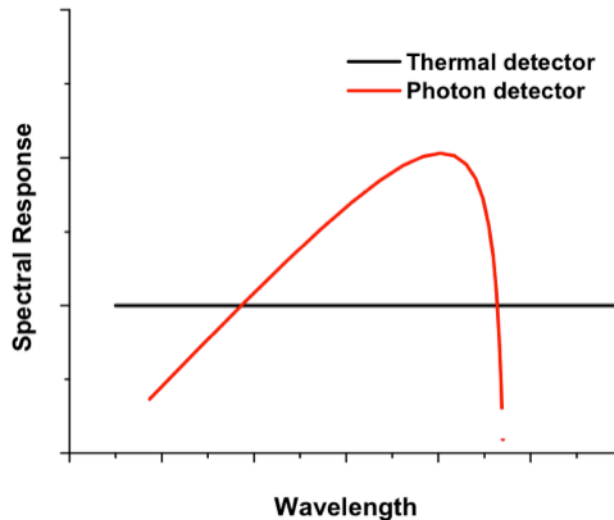
Figure 1.3 Relative spectral response for a photon and thermal detector.

8

response can range from the visible region to 40 μm in the far-infrared range for a thermal detector. Also, these thermal detectors are typically operated at room temperature. They are usually characterized by modest sensitivity and slow response. They have found widespread use in low cost applications, which do not require high performance and speed. A list of thermal detector is included in table 1.1.

Bolometers consist of semiconductor film, thin metal or other type of materials with an absorbing film. This single bolometer chip is mounted to heat dissipating thermal sinks. When the device temperature increases, owing to absorbed IR radiation, the film resistance increases in the case of the metallic film. On the contrary, the film resistance decreases for the semiconductor film. These resistance changes are measured and processed into the temperature change.

Thermocouples are based on the thermo-voltaic effect in which a junction of two dissimilar metals react with a change in voltage according to the amount of incident radiation. These two metals form a hot and cold junction. An incident IR wave falls on the hot junction surface having the high absorption surface with thermal isolation from a thermal heat sink. Conversely, the cold junction is used as a reference junction connected to a thermal heat sink.

Pyroelectricity is known to generate a temporary voltage across the crystal because of the change of polarization of material due to heat generation. Electrical polarization change is related to a change in surface charge, which is dependent on a material time constant. Thus, a pyroelectric effect can be observed only when the temperature rises or falls. Pyroelectric detectors have a broad spectral response for infrared detection and rely on a fast change of polarization in the material; high detectivity can be obtained under high frequency chopping, in contrast to other thermal detectors.

Table 1.1 Infrared thermal detectors

Detector	Method of operation

Bolometer
 	
  Metal
 	
  Semiconductor
 	
  Superconductor
 	
  Ferroelectric
 	
  Hot electron
	Change in electrical conductivity

Thermocouple/Thermopile	Voltage generation, caused by change in temperature of the junction of two dissimilar materials
Pyroelectric	Changes in spontaneous electrical polarization
Golay cell/Gas microphone	Thermal expansion of a gas
Absorption egde	Optical transmission of a semiconductor
Pyromagnetic	Changes in magnetic properties
Liquid crystal	Changes of optical properties

1.3.2 Photon detector

For photon detectors, the radiation is absorbed within the material by interaction with electrons (see Fig. 1.4) [5] that are either bound to lattice or impurity atoms or free electrons. The class of photon detectors that utilizes the generation of electron-hole pairs across the semiconductor band gap is called intrinsic detectors, whereas detectors that utilize transitions of charge carriers from impurity states in the band gap to nearby energy bands are called extrinsic detectors. The main mechanism of photon detectors relies on the concept of energy band gap theory. Photon detectors require incident photons to have a certain minimum energy (equal to the energy band gap of the detector material) before they can be detected.

The observed electrical output signal results from the changed electronic energy distribution. Photon detectors show a selective wavelength dependence of response per unit of incident radiation power (Fig. 1.2). They exhibit both perfect signal-to-noise performance and a very fast response. But to achieve this, the present photon detectors require cryogenic cooling.
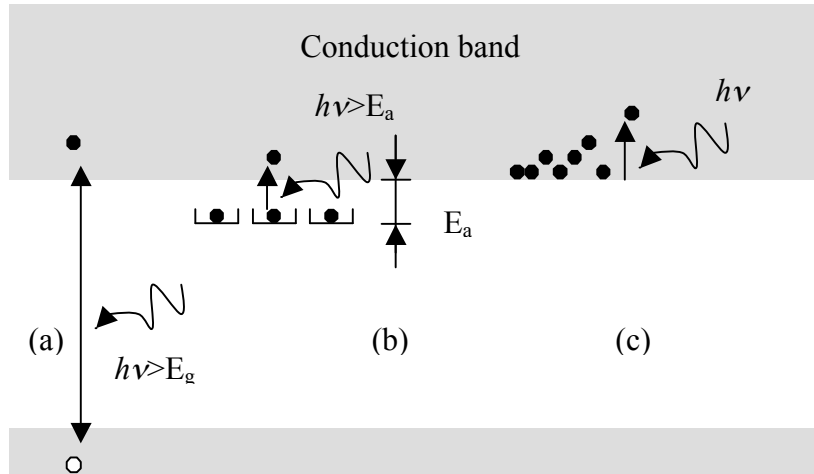
Figure 1.4 Fundamental optical excitation processes in semiconductors: (a) intrinsic absorption, (b) extrinsic absorption, and (c) free-carrier absorption.

Most IR photodetector must be cooled to achieve a high sensitivity. The detection of long-wave infrared (LWIR) radiation, which is characterized by low photon energy, requires the electron transitions to be free-charge carriers of energy lower than the photon energy. Therefore, at near room temperatures, the thermal energy kT is comparable to the transition energy. The direct consequence of this is a very high rate of thermal generation by the charge carriers. The statistical nature of this process generates noise. As a result, long-wavelength detectors become very noisy when operated at near room temperature. Cooling is a direct, straightforward, and very efficient way to suppress the thermal generation of charge carriers, while at the same time being a very impractical method because it adds considerably to the cost, weight, power consumption, and inconvenience of an IR system. The need for cooling is a major limitation of photodetectors and inhibits the more widespread application of IR technology. Affordable high-performance IR imaging cameras require cost-effective IR detectors that operate without cooling, or at least at temperatures compatible with long-life, low-power, and low-cost coolers. Thus, it is highly desirable to eliminate or reduce the cooling requirements in an IR system.

The class of photodetectors is further subdivided into different types based on the nature of the detector's interaction. The most important types are intrinsic detectors, extrinsic detectors, photoemissive (metal silicide Schottky barriers) detectors, quantum well detectors and quantum dot detectors. Depending on how the electric or magnetic

fields are developed, there are various modes of operation such as photoconductive, photovoltaic, photoelectromagnetic (PEM), and photoemissive. Each material system can be used for different modes of operation.

Photovoltaic detectors are made by creating a p-n or p-i-n junction in a semiconductor. A photodiode is sensitive to incoming optical radiation, producing a voltage or current output in response to the input wavelength. The absorbed photons generate electron hole pairs that are guided by an internal electrical field and extracted with an external bias. These photodiodes are characterized by an energy band gap (Eg) and a cutoff wavelength (λc). A photodiode having an intrinsic layer between the n and p material is called a PIN photodiode. The thickness of an intrinsic layer has to be optimized according to the desired spectral response, frequency response, quantum efficiency, and dark current of the detector.

Photoconductive detectors employ transition processes mainly caused by the photoconductive effect. A change in the number of incident photons on a semiconductor causes a change in the average number of free charged carriers in the material. The electrical conductivity of the semiconductor is directly proportional to the average number of these carriers. Therefore, the change in electrical conductivity is directly proportional to the number of photons incident on the semiconductor. Photoconductive devices tend to have somewhat higher signal (responsivity) and sometimes slightly better signal-to-noise ratio than photovoltaic equivalents when operated at optimum frequencies. On the other hand, photoconductors exhibit excess noise at low frequencies - called 1/f or flicker noise, are often slower in frequency response, and the low noise bias circuit costs money. And in advantage, photoconductors can be made with larger active areas than PV devices, so sometimes the need for larger area will prevail over the other advantages of PV devices and make PC the right choice.

1.3.3 Focal Plane Array

The Focal Plane Array (FPA) applications for infrared IR imaging system have been developed generation by generation as Figure 1.5 [6]. In the 1st generation, linear arrays for scanning systems and staring systems are demonstrated. A typical example of the scanning system is a linear photoconductive array. In which an electrical contact to each

element of a multielement array is connected from the cryogenically cooled focal plane to the outside, where there is one electronic amplifying channel at ambient temperature for each detector element. The U.S. common-module HgCdTe arrays employ 60, 120, or 180 photoconductive elements, depending on the application.

In the 2nd generation, two-dimensional arrays for staring systems are developed.

1970s	1970s - 1990s	1990s - on going
1st generation: Linear array	2nd generation: 2D FPA + ROIC	3rd generation: 2D FPA + ROIC with enhanced capabilities
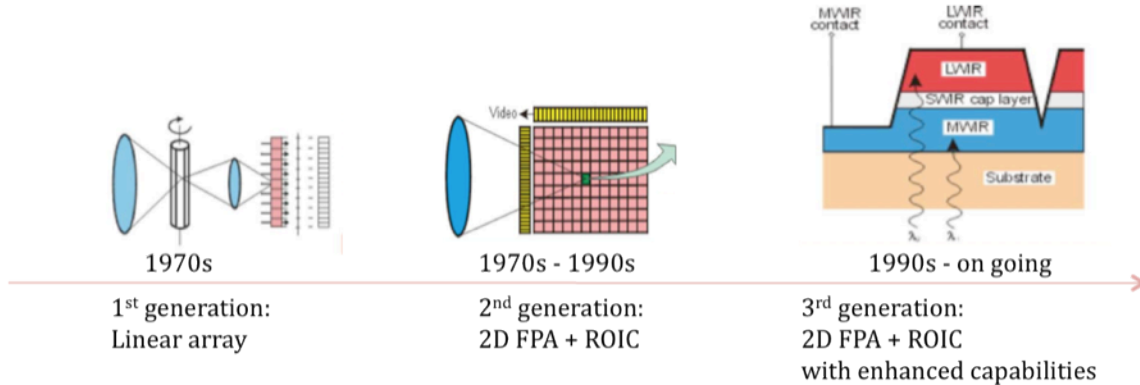
Figure 1.5 History of the development of IR Focal Plane Array detectors and systems. First generation: linear scanning and staring systems. Second generation: staring systems—electronically scanned with 2D FPA and ROIC. Third generation: multicolor functionality and other on-chip functions.

Second-generation systems (full-framing systems) typically have three orders of magnitude more elements ($>10^6$) on the focal plane than first-generation systems, and the detector elements are configured in a two-dimensional array format. These staring arrays are scanned electronically by readout integrated circuits (ROICs) that are hybrid packaged with indium bumps to the arrays. These readout integrated circuits (ROICs) include, e.g., pixel deselecting, antiblooming on each pixel, subframe imaging, output preamplifiers, and some other functions. The detector array can be illuminated from either the front or the back with photons passing through the transparent detector array substrate. In general, the latter approach is the more advantageous, for the multiplexer will typically have areas of metallization and other opaque regions, which can reduce the effective optical area of the structure. Figure 1.6 shows a hybrid IR FPA with independently optimized signal detection and readout.
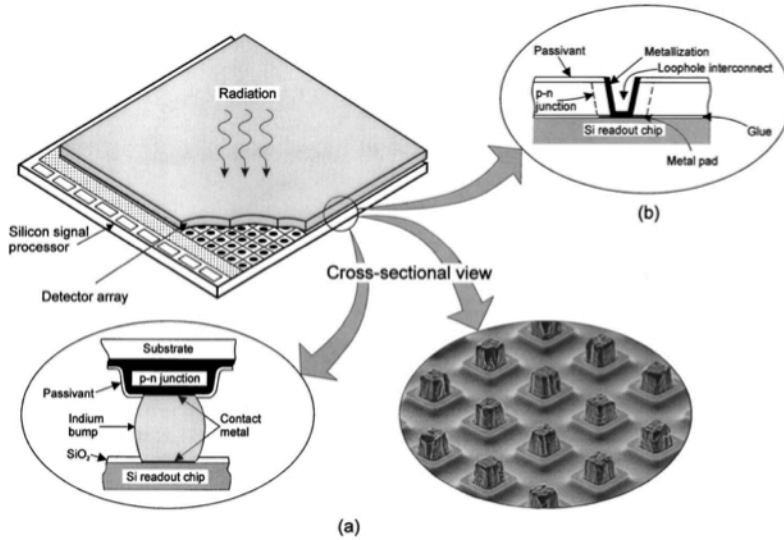
Figure 1.6 Hybrid IR FPA with independently optimized signal detection and readout: (a) indium bump technique, (b) loophole technique.

In the 3rd generation, the main requirements are enhanced capabilities such as the non-cryogenic operation temperature, good uniformity, low cost, larger numbers of pixels, higher frame rates, better thermal resolution, multicolor functionality, and/or other on-chip signal-processing functions. According to Reago et al. [7], the third generation is defined by the requirement to maintain the current advantage enjoyed by the U.S. and allied armed forces. This class of devices includes both cooled and uncooled FPAs: (i) high performance, high resolution cooled imagers having multicolor bands; (ii) medium-to high-performance uncooled imagers; (iii) very low cost, expendable uncooled imagers.

1.3.4 Types of Photon Detectors for Third Generation Focal Plane Array

Several types of photon detectors important for third generation FPA imaging can be distinguished: HgCdTe (MCT) detectors, InSb and InAsSb detectors, GaAs/AlGaAs QWIPs. In the following, we will discuss the current status of different detector materials individually.

1.3.4.1 HgCdTe (MCT) detectors

HgCdTe (commonly pronounced "mer-cad-telluride") has been the dominant FPA for the IR region. Belonging to the II-VI family in the periodic table, $Hg_{1-x}Cd_xTe$ detector is grown by molecular beam epitaxy on CdZnTe substrates that crystallizes in a zinc blende structure. $Hg_{1-x}Cd_xTe$ has a direct bandgap and its energy band gap can be changed as a function of the mole fraction of cadmium to mercury, x, and temperature, T. Therefore, MCT based detectors span all IR (1-30 μ m) range [8]. The independence of lattice parameter on composition is a major advantage of MCT over any other bulk materials. Large optical absorption coefficients enable high quantum efficiency and favorable inherent recombination mechanisms that lead to high operation temperature are other advantages of MCT detectors.

The MCT infrared detector has a currently acceptable operating temperature (80K-200K), but it possesses some serious drawbacks. The sensitive dependence of the energy gap on the alloy composition ratio, requiring a precise control over the growth temperature (ΔT=1-5∘C) during the growth; large tunneling currents due to low electron effective mass; large non-uniformity over large area in LWIR; the CdZnTe substrates currently limited to 7 cm × 7 cm (sufficient for a 4 k×4K and 15 μm detector array), that limits the increasing in detector size. These factors lead to high costs, non-uniformity, and unfulfilled performance promises. Furthermore, the problems magnify as cutoff wavelength increases [9].

1.3.4.2 InSb detectors

Indium antimonide (InSb) was used widely in high-performance near infrared photodiodes. InSb has a direct band gap because the valence band maximum and conduction band minimum are positioned at the center of the Brillouin zone. At 77 K, the energy gap of 0.23 eV corresponds to a MWIR response cutoff of around 5.5μm. At room temperature, the energy band gap is decreased to 0.17 eV, which corresponds to the cutoff of ~ 7 μm [10][11]. The p-n junction can be formed by the controlling the In to Sb ratio. If more antimony is used, an n-type material is formed, while if more indium is used, the material becomes p-type.

InSb is relatively easier to produce than HgCdTe since relatively large-diameter InSb wafers can be obtained from single crystal ingots. This capability extends the current InSb technology to larger FPAs than HgCdTe FPA, and thus, high-quality thermal images with large pixel areas are readily available. In addition, InSb is an equally sensitive alternative to HgCdTe for high-sensitivity MWIR applications that require good, corrected uniformity.

InSb detector arrays are fabricated from large, monocrystalline boules of InSb material. The material is mechanically cut into thin slices that get polished and surface treated before implanting the diode array. After hybridization to the multiplexer and epoxy backfill, the InSb material in excess of the diode implant area is thinned away, usually by mechanical diamond milling or etching. The resulting thin layer of InSb is mechanically much weaker than the multiplexer that it is bump-bonded to, and therefore complies with the multiplexer's thermal expansion. This hybridization and thinning process is well developed and thermally very reliable hybrid arrays are being produced.

1.3.4.3 GaAs/AlGaAs QWIPs

Quantum wells (QW) are two dimensional analogs of the classic quantum mechanical potential wells created by layering two semiconductor materials with two different bandgaps. The material with the smaller bandgap is the "well", and the larger bandgap material serves as the "barrier" of the well. The electrons in the conduction band of the well material become confined and create discrete levels. Detection occurs when
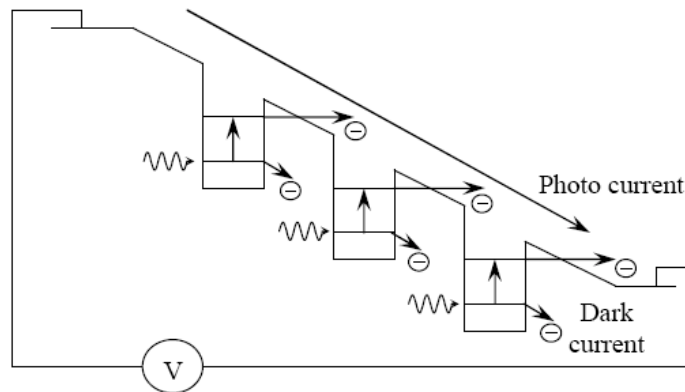
Figure. 1.7 Schematic diagram of GaAs/AlGaAs QWIP

electrons in the well are excited into the bulk conduction band. The distance between these energy levels is smaller than the bandgap of the material and thus allows for detection of photons into the MWIR and LWIR and can be tuned by adjusting the thickness of the well layer. Multiple quantum wells design with barrier layers thick enough to prevent electron tunneling is shown in Figure 1.7.

With respect to MCT and InSb detectors, GaAs/AlGaAs Quantum Well Infrared Photodetectors (QWIPs) are a new approach to create thermal imaging due to mature GaAs growth, device processing, uniform material growth for large diameters (6 inch), high yield and low cost. Uniformity and stability were the key parameters that led to the selection of this technology for thermal cameras.

Another widely claimed advantage for QWIPs is the versatility of the band-gap engineering and of the III-V processing allowing the custom design of quantum structures to fulfill the requirements of specific applications such as: very long wavelength (VLWIR); multi-spectral detection; and polarimetric detection.

However, relatively high values of thermally generated dark current in QWIPs is caused by electron tunneling between wells, which results in a low signal-to-noise ratio. Also, due to absorption selection rules, QWIPs cannot couple photons at normal incidence. They thus require gratings on the surface. As a consequence, the quantum efficiency of QWIP detectors is as low as 20%-30%. The current state-of-the-art QWIP FPA size is the 1024×1024 mega pixels with $25\mu m^2$ pixel size. It is demonstrated with maximal operational temperature of 120K and noise equivalent temperature difference (NETD) equal to 17mK at 95K (f/2.5 optics) [12].

1.3.4.4 InAs/InSb type II Strained Layer

Type II InAs/InSb short period strained layer superlattices (SLS's) have attracted increasing interest for applications in infrared (IR) imaging in the MW and LW region. The key feature that made this material attractive for infrared energy ranges is the high quantum efficiency (QE) and low dark current. Type-II band alignment occurs at the InAs and GaSb hetero-interface.

The InAs/InSb infrared (IR) superlattice consisting of alternating ultra thin semiconductor layers with its period less than the electron mean path is grown by MBE

on GaSb substrates. The heterojunction formed between InAs and GaSb and principle of photons absorption in SL is shown in the Figures 1.8. The bottom of the conduction band of InAs in below the top of the valence band of GaSb. The superlattice energy band gap is created via the separation between the confined hole states in the valence band of GaSb and the confined electron states in the conduction band of InAs. This forms a direct energy band gap that can be adjusted by widths of the individual layers. By changing thickness of constituent layers, the effective separation between the lowest confined conduction subband and the highest valence subband can be tuned in the 3-30 μm range.
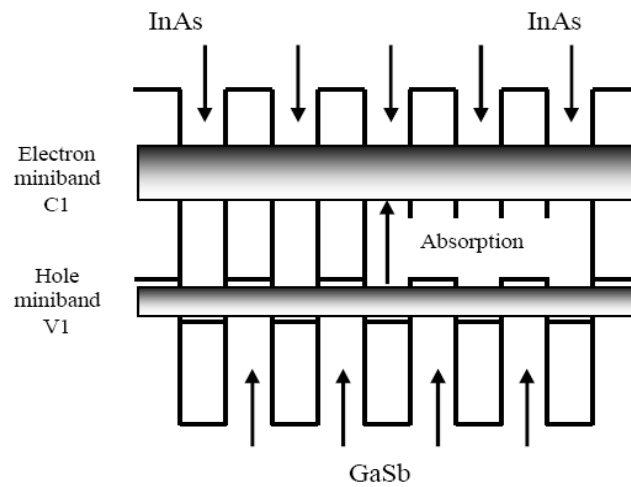
Figure 1.8: Schematic diagram and absorption in InAs/GaSb Supperlattice

Theoretical models of SLS performance predict MWIR device dark current levels to be 1-10% of modern HgCdTe and InSb devices [13]. SLS devices experience a reduction in dark current due to reduced Auger recombination and lower tunneling rates due to higher electron effective masses. SLS are expected to have intrinsically higher quantum efficiency than QWIPs, in which the optical selection rules for intersubband transitions forbid the absorption of normally incident light. Finally, multicolor detection can also be achieved by stacking several of these devices separated with a barrier layer.

1.4 Quantum Dot Infrared Photodetectors

1.4.1 Concept of Quantum Dot

In bulk semiconductors, excited electrons may have any energy over a continuous energy spectrum. Quantum confinement, an abrupt energy change over a small spatial region comparable with the electron wave function, will lead to quantization of energy, causing the energy states available to electrons changing from continuous to discrete. Electrons can occupy over a unit energy range that can be calculated as the density of state (DOS) [14]. Figure 1.9 shows the DOS for systems with different levels of confinement. Bulk semiconductors, a 3D structure without any confinement, have a continuous DOS. Quantum wells, a 2D structure with one-dimensional confinement, have step like DOS. Quantum wires, a 1D structure with two-dimensional confinement, have a palm like DOS. Quantum dots, a 0D structure with the ultimate three-dimensional confinement provides delta function like DOS. The DOS of the bulk, quantum well, quantum wire, and quantum dot can be represented as equations listed at Figure 1.10, where Θ is the Heavyside step function, and δ is the Dirac delta function. The total electron

$$DOS_{3D}(E) = \frac{1}{2\pi^2}\left(\frac{2m}{\hbar^2}\right)^{\frac{3}{2}}\sqrt{E}$$

$$DOS_{2D}(E) = \frac{m}{\pi\hbar^2}\sum_{i}\Theta(E - E_i)$$

$$DOS_{1D}(E) = \frac{1}{\pi}\left(\frac{m}{2\hbar^2}\right)^{\frac{1}{2}}\sum_{i,j}\frac{1}{E - E_{ij}}$$

$$DOS_{0D}(E) = 2\sum_{i,j,k}\delta(E - E_{ijk})$$
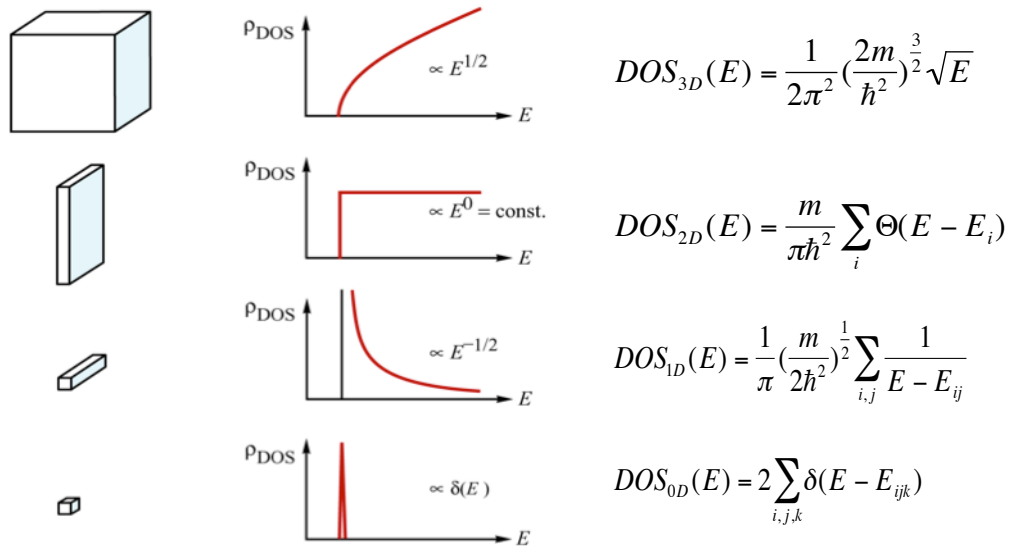
Figure 1.9 Electronic density of states of semiconductors with 3D, 2D, 1D, and 0D degrees of freedom for electron propagation

concentration in a band (equation 1.5) is then obtained by integration over the product of state density and the probability that the state is occupied, that is

$$n = \int_{E_{bottom}}^{E_{top}} \rho_{DOS}(E) f(E) dE \qquad (1.5)$$

where $f(E)$ is the (dimensionless) probability that a state of energy E is populated. The limits of the integration are the bottom and the top energy of the band, since the electron concentration in the entire band is of interest. The probability of occupation (equation 1.6), $f(E)$, is given by the Maxwell–Boltzmann distribution which also frequently referred to as the Boltzmann distribution,

$$f_B(E) = \exp(-\frac{E - E_F}{kT}) \qquad (1.6)$$

where E_F is the Fermi energy .

Quantum confinement gives discrete energy states, which is similar to atoms with discrete states due to strong confinement and Coulomb interaction. The exact energy of the discrete states depends on the strength of confinement, size and shape of QDs, which can be controlled in the material growth. It is possible to make QDs with controllable discrete states, so QDs are also called "artificial atoms". Usually the size of the confinement in a few to tens of nm, and the energy change is a few hundred or thousand meV in QDs. Due to this strong confinement in a size smaller than the electron de-Broglie wavelength, the wave function of exciton is localized in a confined area within a QD.

The low density of states and small size of the dots means that fewer carriers are needed to invert the carrier population, which results in easily saturated absorption due to the finite density of states in QDIP detectors. Compared to QWIPs, QDIPs have obvious advantages such as: the ability to absorb normally incident light due to three dimensional confinement, high temperature operation due to the reduced dependence of the density of states on temperature, and carrier lifetimes 10-100 times longer than QWIPs, giving rise to a lower dark current. For real devices made of QDs, however, the density of states has a line broadening due to variations in dot size.

1.4.2 Phonon Bottleneck and Effective Carrier Lifetime in QDs

The carrier dynamics in 3-D, quantum-confined heterostructures differ significantly from those of bulk material and QWs. In particular, while first-order, electronphonon interactions cause rapid relaxation in bulk and QW semiconductor materials, electron-phonon coupling is suppressed in QDs due to the magnitude of the intraband energy spacing between confined levels in QDs [15][16]. More specifically, the intraband energy spacing is > 50 meV for practical QD sizes, while the longitudinal-optical (LO) phonon energy is < 40 meV [17]. Thus the conservation of the electron energy and momentum cannot be maintained by the emission of a single, LO phonon. Similarly, single, longitudinal-acoustic (LA) phonon emission (achieved by coupling with the deformation potential) is reduced for intraband energy spacings greater than a few meV [18]. This reduction of electron-phonon scattering for QDs, which leads to longer electron lifetimes in QDs (and increased photoconductive gain in detectors), is known as the phonon bottleneck.

Several experiments have been conducted to confirm the existence of the phonon bottleneck, including electroluminescence and time-resolved photoluminescence measurements of InGaAs/GaAs QDs [19], high frequency electrical impedance measurements in $In_{0.4}Ga_{0.6}As$/GaAs QD lasers [20], and time-resolved differential transmission spectroscopy (DTS) measurements of $In_{0.4}Ga_{0.6}As$/GaAs QDs [21]. DTS measurements have resolved two time constants for relaxation from the excited state to the ground state in $In_{0.4}Ga_{0.6}As$/GaAs QDs. The short time constant (~7 ps) is governed by Auger, e-h, and multiphonon scattering in a geminate carrier configuration. The long time constant (~750 ps) is governed by phonon-mediated scattering in a non-geminate carrier configuration [22], and is evidence of the phonon bottleneck in QDs. In addition to the long electron lifetime in the QD excited states, the phonon bottleneck also promises temperature-independent performance since the electron is energetically de-coupled from the optical phonon, the properties of which depend very heavily on the temperature. Thus, the suppression of phonon scattering in QDs suggests that electron relaxation lifetimes are significantly longer than those in QWs (~1-10 ps), which are dominated by scattering due to the emission of single optical phonons.

The phonon bottleneck also affects the effective carrier lifetime in QDs. The effective carrier lifetime is essential to QDIP performance in that if the lifetime is too short, a

photoexcited carrier will relax to the ground state before it has a chance to be collected as photocurrent. However, if the effective carrier lifetime is long enough, an efficient detector can be realized since photoexcited carriers are more likely to contribute to the photocurrent.

1.4.3 Formation of Self-Assembled Quantum Dots

The research efforts of the last decades established a number of experimental techniques for self-assembled QD growth [23]-[26], such as molecular-beam epitaxy (MBE), metalorganic chemical vapor deposition (MOCVD), liquid-phase deposition (LPD), and metalorganic vapor phase epitaxy (MOVPE). Good conditions for systematic investigations of QD growth are given in the case of MBE: The substrates are prepared atomically clean in ultra-high vacuum (UHV) in contrast to MOCVD where residues of reactant gases are unavoidable. This dissertation work has discussed both of the selective capping techniques of Stranski-Krastanov QDs and the optimized growth technology of Sub-Monolayer (SML) QDs in Molecular Beam Epitaxy (MBE) growth to engineer the dot geometry and 3D quantum confinement more close to the 3D "artificial atom".

1.4.3.1 Stranski-Krastanov Quantum Dots

There are three generally accepted principal growth modes of thin solid films: Frank-van der Merve (FM) or layer growth mode, Volmer-Weber (VW) or island growth mode, and Stranski-Krastanov (SK) or layer-plus-island growth mode [27]. The growth of epitaxial (homogenous or heterogeneous) thin films on a single crystal surface depends critically on the interaction strength between adatoms and the surface. As seen in Figure 1.10, when the strain between the epitaxial layer and the substrate is minimal, adatoms attach preferentially to surface sites resulting in atomically smooth, fully formed two-dimensional layer growth, called as Frank-van der Merwe mode. The strain that is referred here is compressive strain which is caused by deposition of an epitaxial layer with a larger lattice constant than the substrate. As the strain increases, beyond a certain critical thickness of the epitaxial layer, it is energetically favorable to increase surface area by forming 3D islands than by relaxing the strain through dislocation generation. This growth regime is referred to as Stranski-Krastanow mode of growth and starts

initially with 2D growth followed by 3D island growth. Transition from the layer-by-layer to island-based growth occurs at a critical layer thickness which is highly dependent on the chemical and physical properties, such as surface energies and lattice parameters, of the substrate and film. If the lattice mismatch between the epitaxial layer and the substrate is very high, adatom-adatom interactions are stronger than those of the adatom with the surface, leading to the formation of three-dimensional adatom clusters or islands. Growth of these clusters, along with coarsening, will cause rough multi-layer films to grow on the substrate surface, or direct formation of 3D islands, called Vollmer-Weber growth. Figure 1.10 is a schematic representation of the three main growth modes for various surface coverages. Each mode is shown for several different amounts of surface coverage, Θ, which is larger or less than 1 or 2 monalayer (ML). Stranski-Krastanov growth mode is the widely used growth mode to from high crystal and optical quality Quantum Dot.

Stranski-Krastanov growth mode is a generally accepted principal growth mode to form Quantum Dot. SK QDs has high crystal quarlity, good opotical property, has wide applications in infrared detectors, lasers, and solar cells.
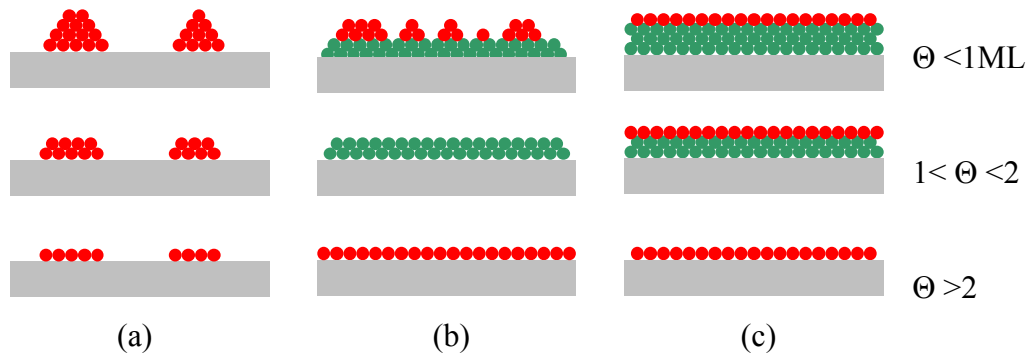
Figure 1.10 The schematic representation of the three main growth modes for variation of surface coverage (a) Volmer-Weber (VW), (b) Stranski-Krastanov (SK) (c) Frank-van der Merve (FM)

1.4.3.2 Capping of SK QDs

Although self-assembled QDs have performed impressively in a variety of electronic and optoelectronic devices, their full potential has not been achieved. This is due in part of the fact that the epitaxially grown quantum dots tend to be "pancake" shaped due to

the flattening of the dots via intermixing during the growth of the capping layer and the loss of discrete quantum mechanical confinement [28][29].
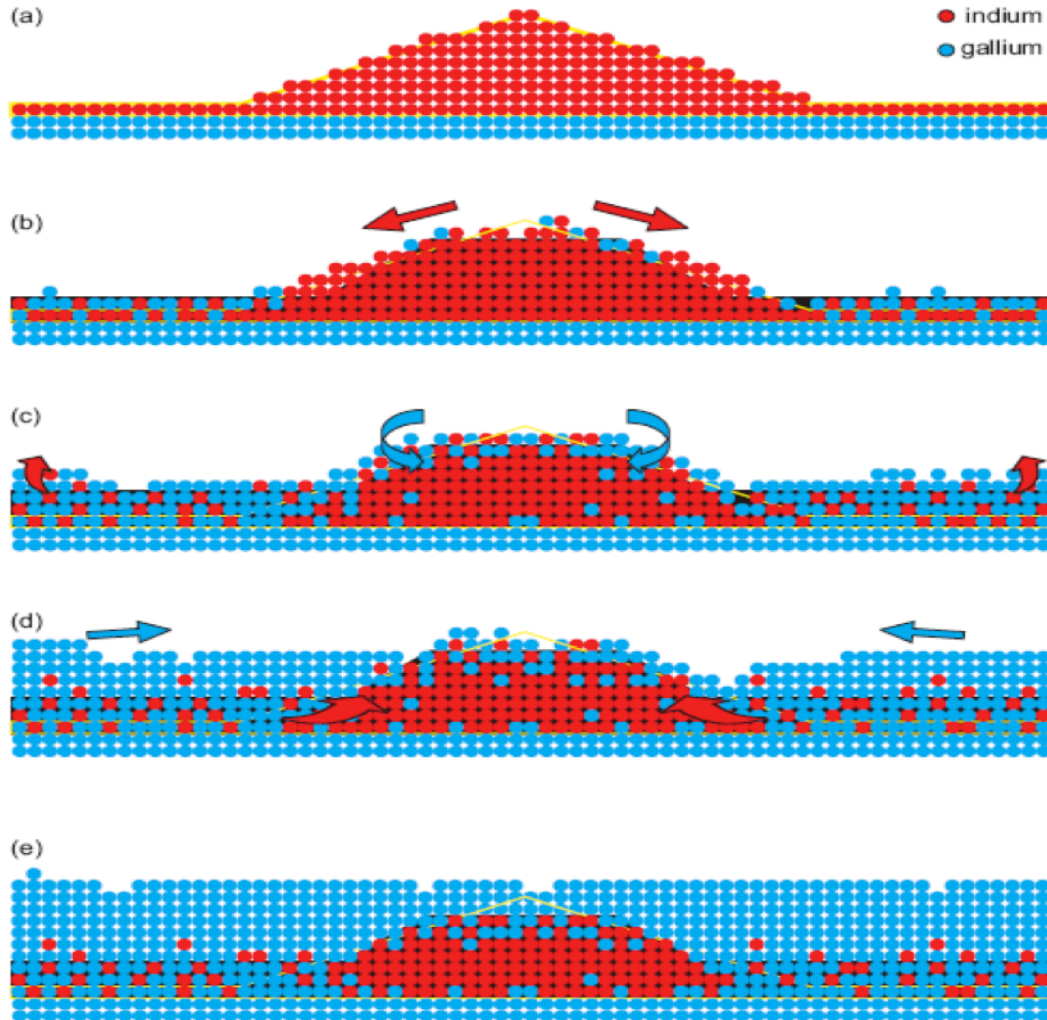
Figure 1.11 Atomistic model for the capping growth process. Arsenic atoms are not drawn in terms of simplicity. (a) Uncapped InAs QD with a triangular cross-sectional shape (b) Initial GaAs cap layer deposition is draged towards the edges of the wetting layer. (c) Gallium atoms are incorporated at the surrounding InAs wetting layer and afterwards at the QD, resulting in intermixing of indium and gallium at the interface. (d) After completing the capping growth of the wetting layer, the quantum dot is further capped starting at its sides (e) After the capping growth process, QD shows pancake shape with intermixed side facets and reduced indium content in the QD and wetting layer.

The atomistic model for the capping growth progress of the InAs QD with GaAs QW is shown in Figure 1.11 [30]. In order to keep the model as simple as possible only the indium (red) and gallium (cyan) atoms are shown. The capping growth process starts with the pyramidal quantum dot shape (a), and indicated by the yellow contour line. The highest strain in this system is found at the bottom edge of the quantum dot, while the apex is almost relaxed with a local lattice constant close to the one of bulk InAs.

Consequently the gallium atoms from the first Monolayer (ML) GaAs cap will not be incorporated at the quantum dot top due to the large lattice mismatch, but they drag the indium atoms from the apex to the quantum dot edges, as indicated by the red arrows (b). A segregation-induced exchange of indium and gallium at the wetting layer reduces the strain and the lattice mismatch, since an intermixed wetting layer is energetically more favorable than a pure InAs wetting layer. During further capping growth the gallium atoms will easier be incorporated into the InGaAs wetting layer and only afterwards at the quantum dot [Fig. 1.11 (c)]. The indium segregation to the wetting layer is indicated in (c) by the red arrows, while the intermixing of gallium and indium at the QD top is shown by the cyan arrows. After completing the capping growth of the wetting layer the quantum dot is further capped starting at its sides [Fig. 1.11 (d), cyan arrows]. In addition indium atoms from the strained quantum dot sides segregate to the upper side flanks as indicated in (d) by the red arrows. In this way the reversed-cone indium distribution develops, especially observed for quantum dots containing higher indium amounts. Finally the shape of the quantum dot has changed from a triangular to a pancake shape as indicated by the black background (e).

The capped QD shows pancake like shape with low height to base aspect ratio and steeper side facets intermixing with the capping material. That inhibits QDs from behaving like "artificial atoms" by modifying the discrete density of states and thereby suppressing interesting phenomenon like the "phonon bottleneck". Moreover, the s-polarization (TE mode or equivalent to top normal incidence) spectral photoresponse in quantum dot detectors is typically as low as 10% of the p-polarization (TM mode) [31]. Thus in normal incidence quantum dot imagers without gratings, 90% of the signal is not utilized.

In this dissertation, the result demonstrate our success in shape engineering the QDs by selective capping technology to grow QD with small base width, increased height, reduced intermixing between the dots and the capping materials. This has enabled us to evolve from "pancake" shaped dots to "cone-shaped" dots, which is closer to the 3D "artificial atom" with improved quantum confinement, increase normal incidence absorption, low dark current, longer carrier lifetime, high operating temperature.

1.4.3.3 Sub-Monolayer Quantum Dot

Another alternative novel technology to grow QD with small base width, high height and improved 3D quantum confinement is the sub-monolayer quantum dot (SML-QD) growth technology. Sub-Monolayer (SML) Quantum Dot has attracted more attention recent years due to small base diameter (6-8nm), better three-dimensional quantum confinement, large dot density, tailorable aspect ratio, and absence of the wetting layer [32]-[34]. In this dissertation we demonstrate the growth and application of the SML QDs, which are formed as stacked layers of InAs with GaAs or $In_xGa_{1-x}As$ QW on a GaAs(001) substrate, therefore, the $InAs/In_xGa_{1-x}As$ matrix is functionally working as a 3D quantum dot.

This SML growth progress regime is shown in Figure 1.12. As seen in Figure 1.12 (a), when the amount of the InAs material is greater than that required to form a smooth 2D layer, due to the strain between the epitaxial material and the substrate, 3D islands are formed. Followed by deposition of the same epitaxial materials as the substrate, the 3D islands are buried and the substrate surface turned back to smooth again as shown in Figure 1.12 (b). If the process (a) is repeated (Figure 1.12 (c)), the second layer of 3D islands should automatically vertically self align to the first layer of 3D islands due to the surface strain. Repeat process (b) the 3D islands are buried and the substrate surface turned back to smooth again as shown in Figure 1.12 (d). If repeating above growth procedure, the SML QDs can be grown with adjustable height as shown in Figure 1.12 (e).

Such growth correlations were revealed [33] already in the infancy of QD studies, and are still investigated as a possible route to the creation of ordered 3D arrays of QDs with a narrow size distribution. Under appropriate growth conditions, this procedure results in

a crystalline, dislocation-free structure with QD layers stacked along the growth direction and separated by the material of the spacer layer. The electronic wavefunction of the vertically aligned 3D islands stacks is equivalent to a quantum dot. And in this way, the dots stack have small base width as 6-8 nm, and may be strongly electronically coupled in vertical direction and thus have a larger height-to-width ratio leading to a stronger absorption for a normal incidence infrared light.
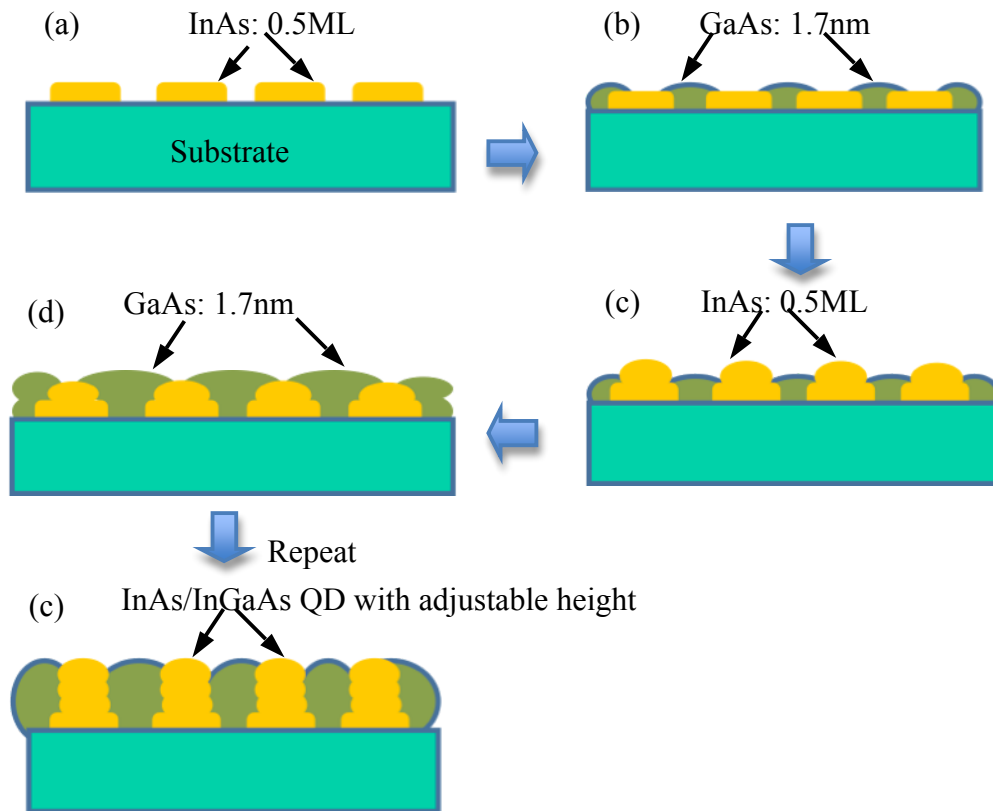
Figure 1.12 The SML-QDs growth process. (a) Uncapped 0.5 ML InAs QD with small base diameter and flat shape (b) After the 1.7nm GaAs capping layer deposition, the 3D islands are buried and the substrate surface turned back to smooth. (c) The second layer of 3D InAs islands will automatically vertically self align to the previous layer of 3D InAs islands due to the surface strain. (d) After the 1.7nm GaAs capping layer deposition, the 3D islands are buried and the substrate surface turned back to smooth. (e) After repeating (c) and (d), InAs/InGaAs QDs with adjustable height are formed.

1.4.4 Quantum Dot Infrared Photodetectors

Self-assembled quantum dot infrared photodetectors (QDIPs) have attracted much interest in recent years. It has been predicted [35]-[37] that QDIPs will significantly outperform QWIPs to emerge as an important technology for the mid- and long-wave regions infrared detection. Compared to QWIPs, the three-dimensional confinement in quantum dots has many advantages, such as (1) ability to absorb normally incident light due to three dimensional confinement, thereby eliminating the need of special light coupling techniques such as gratings, (2) temperature insensitive operation due to the reduced dependence of the density of states on temperature, (3) carrier lifetimes 10-100 times longer than QWIPs, giving rise to a lower dark current. Various groups have been working on methods to improve the structural and optical properties of quantum dots [38]-[44] to increase the carrier lifetime as well as to increase the quantum dot density. Dark current levels have been significantly reduced by using AlGaAs as current blocking layers [45]-[47].

1.4.5 DWELL QDIPs

The quantum dot-in-a-well (DWELL) detector is a hybrid between the conventional quantum well and the emerging quantum dot detectors. The DWELL name comes from the active region's structure, which consists of a layer of quantum dots embedded in (or in
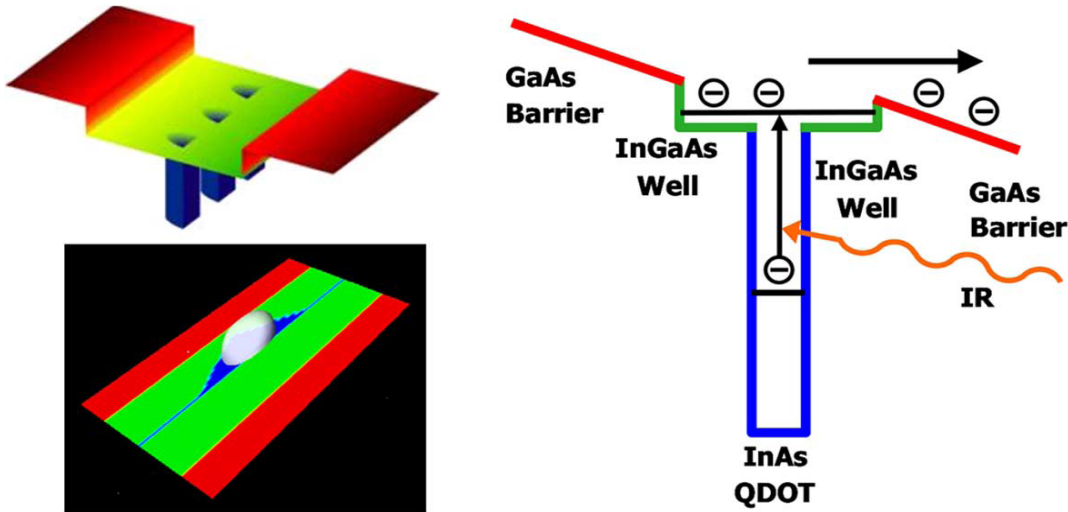
Figure 1.13 Potential profile in a typical dots in a well structure

some cases grown on) a quantum well. This dot/well combination is similarly surrounded by a barrier material.

Figure 1.13 shows the theoretical model that was used to define the InAs dot in a InGaAs well with GaAs barrier heterostructure, and the optical interband and interband transitions in the DWELL QDIP structure. The absorption occurs mainly between the ground state bound in the dots and the state of the well. There are 3 primary types of intersubband transitions to detect light at precise wavelengths due to the band engineering, such as (a) bound-to-bound, (b) bound-to-quasi-bound, and (c) bound-to-continuum transitions. The DWELL structure has combined advantages of quantum well and QDs resulting in a relatively flexible detection wavelength control and a strong quantum confinement of the electrons. Moreover, they demonstrate normal incidence operation due to their three-dimensional quantum confinement [48][49]. And the thermal generation of electrons is significantly reduced due to three dimensional confinement of the electrons (or holes) in all three dimensions. Furthermore, the DWELL structure provides better confinement for the carriers trapped in the QDs by lowering the ground state of the QD relative to the InGaAs/GaAs bandedge. This leads to lower thermionic emission.

In the recent 10 years, several research groups have demonstrated some significant progress at the band engineering of the DWELL structure to optimize the performance of QDIPs. The several primary approaches are listed below:

1. **Vary the Indium composition in the $In_xGa_{1-x}As$ QW**

The Indium composition of the quantum well layer mainly engineers the QW energy levels, tailors the operating wavelength and the nature of the transitions [48]. As shown in Figure 1.14, the continuum energy level of $In_{.20}GaAs$ QW is lower than that of $In_{.15}GaAs$ QW, so the peak wavelength of hv_2 is red-shifted. While the Indium composition of the quantum well has an influence on the strain under the wetting layer, thus effecting the energy levels and shape of the QDs.
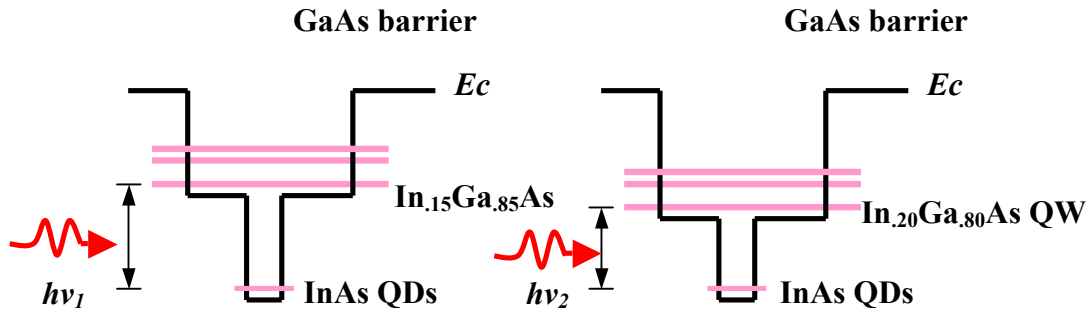
Figure 1.14 The conduction band diagram and intersubband transitions in the DWELL QDIP structure. (a) $In_{.15}Ga_{.85}As$ Quantum well (b) $In_{.20}Ga_{.80}As$ Quantum well.

2. Vary the thickness of the bottom $In_xGa_{1-x}As$ QW

As shown in figure 1.15, the thickness of the bottom $In_{.15}Ga_{.85}As$ QW is varied from 10 Å to 60 Å [50]. The asymmetric distribution of the bottom well layer has a significant influence on the strain under the wetting layer, have effect to the strain status and energy levels in the QDs, tailor the operating wavelength and nature of transitions.
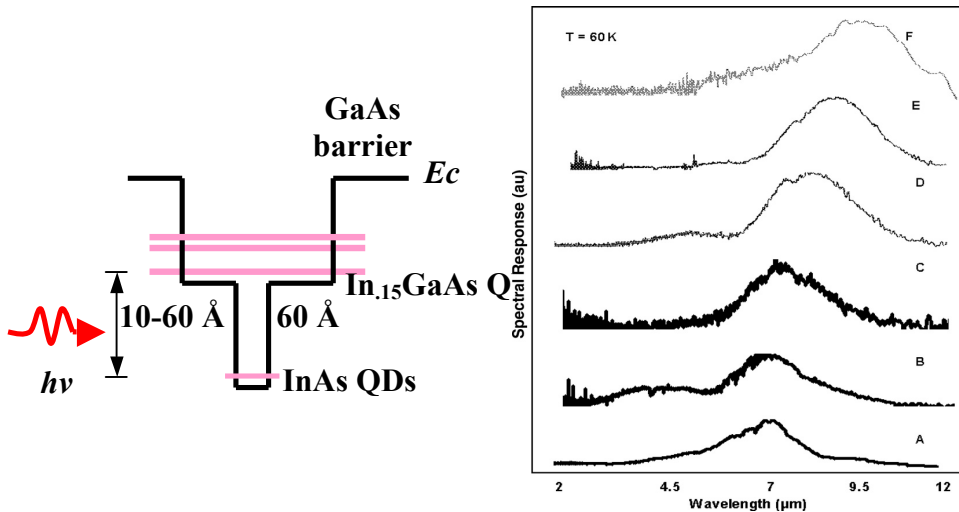
Figure 1.15 (a) The conduction band diagram and intersubband transitions in the DWELL QDIP structure. The bottom InGaAs layer is changes from 10 to 60 Å. (b) Progressive red shift in the peak wavelength of the detector as the width of the bottom InGaAs layer is increased from 10 to 60 Å. The spectra have been vertically displaced for clarity.

3. Vary the symmetry of confining potential

The change in optical transition energy in a quantum well caused by an electric field is called the *quantum-confined Stark effect (QCSE)*. The detailed band diagram of a quantum well structure and the change in transition energy is illustrated in Figure 1.16 (a) without and (b) with electric field. The energy of the lowest state changes upon application of field. The change can be calculated by second-order perturbation theory. Figure 1.16 (c) shows a spectral response of a 10-layer InAs/InGaAs DWELL as a function of the applied bias demonstrating the QCSE. Using a projection algorithm, this spectral diversity can be exploited to develop spectrally smart sensors whose centre wavelength and bandwidth can be tuned depending on the desired application [51].
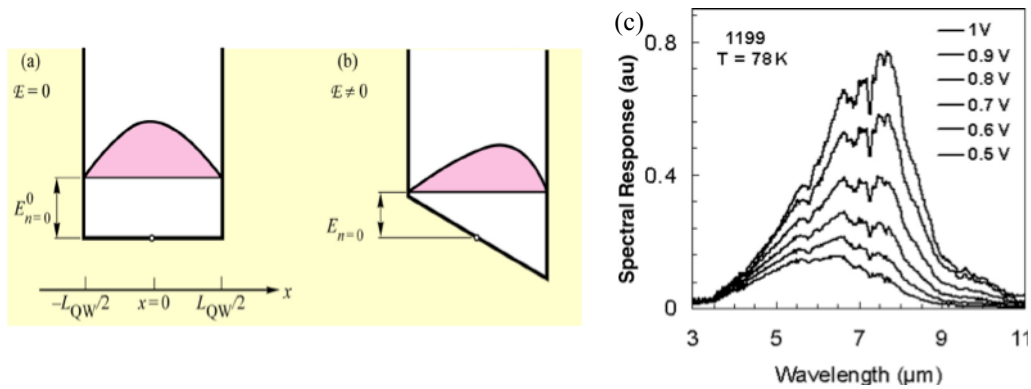
Figure 1.16 The detailed band diagram of a quantum well structure and the change in transition energy (a) without and (b) with electric field, (c) a spectral response of a 10-layer InAs/InGaAs DWELL as a function of the applied bias demonstrating the QCSE.

4. DDWELL

R. V. Shenoi et al. [52] demonstrated the $InAs/In_{0.15}Ga_{0.85}As/GaAs/Al_{0.10}Ga_{0.90}As$ dots-in-a-double-well (DDWELL) detector where the InAs quantum dots are embedded in $In_{0.15}Ga_{0.85}As$ and GaAs wells with the use of $Al_{0.10}Ga_{0.90}As$ barriers. The thickness of $In_{0.15}Ga_{0.85}As$ well is limited to 1 nm above and below the dot as opposed to 5 and 6 nm in traditional DWELLs. As shown in Figure. 1.17, the GaAs well forms the primary well in these devices and has a thickness of 4 nm below the dot and 6.85 nm above the dot. The $In_{0.15}Ga_{0.85}As$ layer below the dot acts as a strain bed for the QD growth while the

layer above the dots acts as a capping layer that helps to preserve the dot shape. The system strain is reduced by using the GaAs second well. $Al_{0.10}Ga_{0.90}As$ was used as the barrier material. This device shows responses with peaks at 8.7 μm for negative bias voltages and peaks at 9.4 μm and 6.8 μm at positive bias voltages. The LWIR peak due to transitions from a state in the quantum dot to a state in the quantum well, is dominant at higher bias voltages and the MWIR peak due to a dot to quasi-bound transition is dominant at lower bias voltages. These lower strain quantum dots-in-a-double-well devices exhibit lower dark current, lower noise equivalent temperature difference, and higher uniformity than the previous generation DWELL devices while still demonstrating spectral tunability.
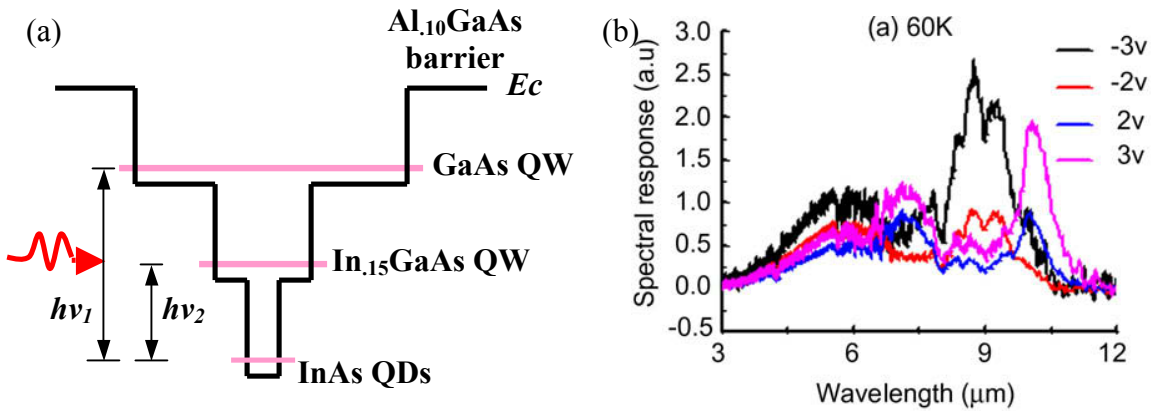
Figure 1.17 (a) The band diagram of a DDWELL structure (b) Bias-dependent spectral responses of DDWELL at 60 K
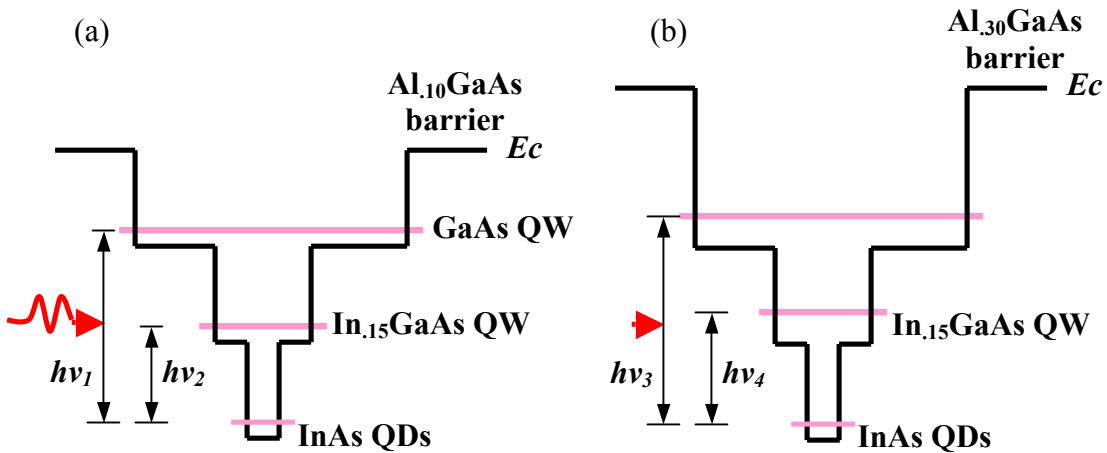
Figure 1.18 The band diagram of a DDWELL structure with (a) $Al_{.10}GaAs$ barrier (b) $Al_{.30}GaAs$. The peak wavelength of hv_3 and hv_4 is blue shifted to hv_1 and hv_2.

5. $Al_xGa_{1-x}As$ barrier

High Aluminum composition in the $Al_xGa_{1-x}As$ block barrier can reduce the dark current, and increase the operating temperature of the detector [53]. As shown in Figure 1.18, varying the Aluminum composition in the AlGaAs barrier can influence the 2D continuum quantum well energy state, tailor the operating wavelength and the nature of the transitions. The peak wavelength of hv_3 and hv_4 is blue shifted to hv_1 and hv_2.

6. Addition of a resonant tunneling barrier

P. Bhattacharya et al. [54] report multi-band tunneling quantum dot infrared photo detector (T-QDIP) structures designed for high temperature operation covering the range from mid- to far-infrared. These structures consist of a QD (InGaAs or InAlAs) placed in a well (GaAs/AlGaAs) with a double-barrier system (AlGaAs/InGaAs/AlGaAs) adjacent to it as shown in Figure 1.19. The photocurrent, which can be selectively collected by resonant tunneling, is generated
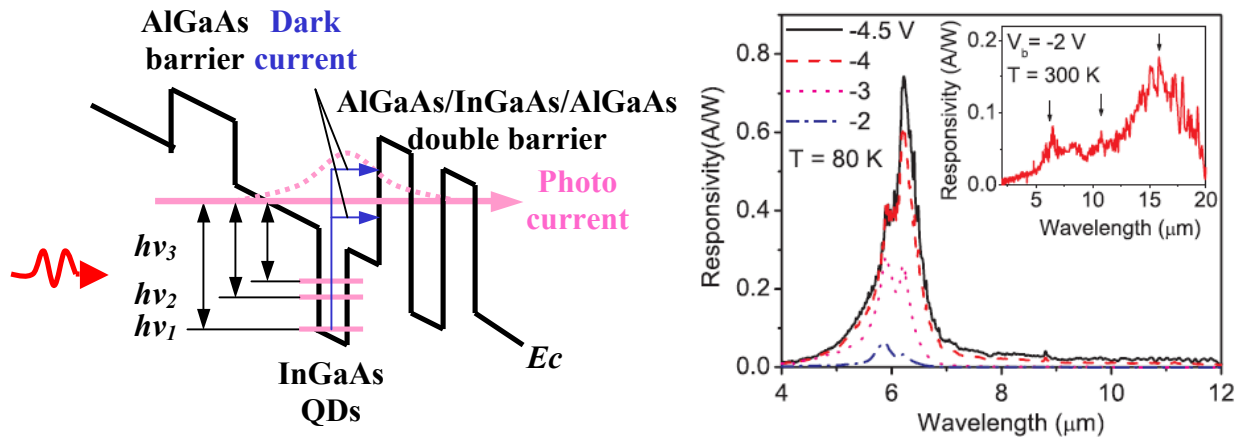
Figure 1.19 (a) Schematic diagram of the conduction band profile of T-QDIP structure under reverse bias. (b) Response of the T-QDIP detector at 80 K under different bias voltages. The response at 300 K is shown in the inset. The arrows represent the positions of the peaks resulted from different transitions in the structure. The peaks at 11 and 17 μm are possible only at high temperatures since the transitions leading to these peaks are enabled by the carrier occupancy in the states $E1$ and $E2$, which occur at high temperatures.

by a transition of carriers from the ground state in the QD to a state in the well coupled with a state in the double-barrier system. The double-barrier system blocks the majority of carriers contributing to the dark current. The energy level positions in the QD with respect to the resonant state are denoted by hv_1, hv_2, and hv_3. Only the carriers excited to the resonant state will contribute to the current. Hence, most of the dark current will be blocked, except the thermal excitations on to the resonant state. The resonance condition is possible only under an applied bias when there is an overlap between the resonant state and the state in the double-barrier system. Several important properties of T-QDIP detectors such as the multi-colour (multi-band) nature of the photoresponse, the selectivity of the operating wavelength by the applied bias, and the polarization sensitivity of the response peaks, have been demonstrated in several other research groups [54]-[56]. The reduction of the dark current without reducing the photocurrent is a considerable challenge in developing far-infrared detectors.

1.5 Objective and Contribution of This Dissertation

After reviewing the six main approaches described above to improve the performance of DWELL QDIPs, we found that most of them focus on the band engineering of the quantum well in the DWELL structure. This dissertation focuses on engineering the Stranski-Krastanov QD and the Sub-Monolayer QD in the QDIP detectors.

The third generation FPA IR imaging systems require enhanced detector capabilities such as the non-cryogenic operation temperature, good uniformity, low cost, larger numbers of pixels, higher frame rates, better thermal resolution, multicolor functionality, and/or other on-chip signal-processing. The QDIP is a competitive novel technology with advantages such as normal incidence detection, low dark currents and high operating temperatures, high detectivity, while enjoying all the benefits of a mature GaAs fabrication technology. But in the practical, conventional Stranski-Krastanov QD with flat shape, low height to base aspect ration, interface diffusion can not fully exploit the 3D "artificial atom" property. The conventional SK-QD are normally with large dot base width as 17nm -35nm, that leads to the weak in-plane (TE mode) quantum confinement and weak normal incidence absorption. The interface diffusion between the quantum dot and quantum well make the DWELL lose abrupt quantum confinement, lose discrete 0D

quantum energy status, and decrease the carrier lifetime. In addition, the interface diffusion provides a leakage path for carriers, lead to increase the dark current and decrease operating temperature. In the QDIP performance, that will affect several important parameters such as: responsivity, detectivity, highest operating temperature, and quantum efficiency.

The objective of this dissertation is the following: To control the dot geometry, preventing interface diffusion and optimizing 3D quantum confinement, grow nanoscaled quantum dot close to 3D "artificial atom" to achieve high performance quantum dot infrared photodetectors (QDIPs) for the 3rd generation FPA IR system. The experimental research consists of two parts: (1) For the engineered QDs QDIP, using selective post growth capping materials of the QDs to engineer the dot geometry and the quantum confinement. (2) For the SML-QD QDIP, using optimized growth condition such as InAs thickness, stacks of InAs layers, selective quantum well materials, growth temperature, III/V BEP flux ratio, and interrupt time before and after InAs deposition, to engineer the dot geometry and the quantum confinement.
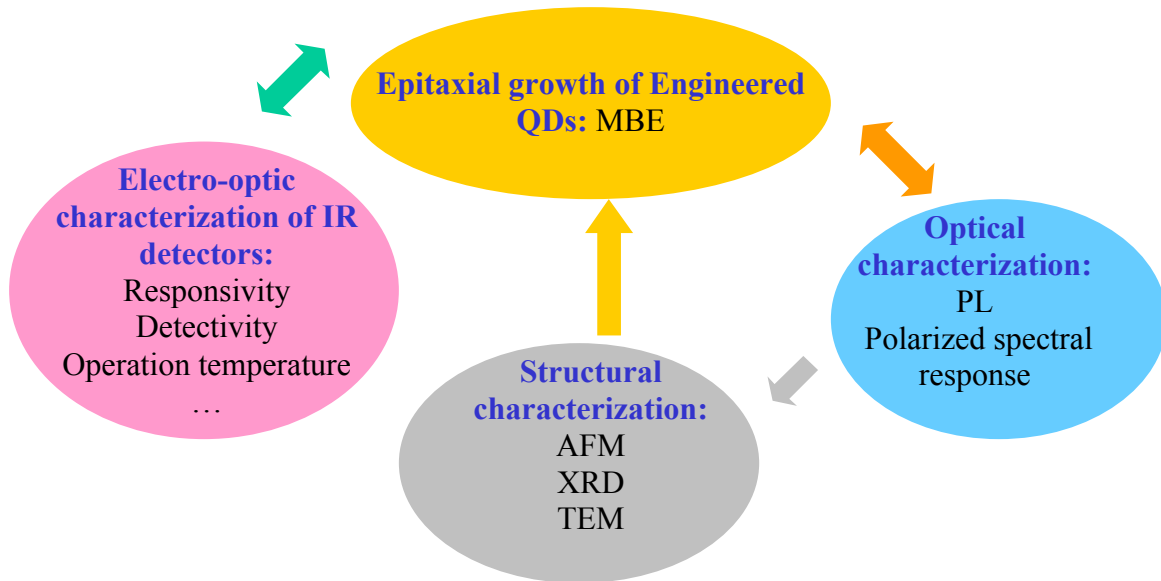
Figure 1.20: Four main approach methods to engineer Stranski-Krastanov QD and Sub-monolayer QD in this dissertation

The approach experimental methods of the dissertation are divided into four main areas shown in Figure 1.20. They are (i) Epitaxial growth of Engineered QDs by

molecular beam epitaxy (MBE), (ii) Optical Characterization (iii) Structural characterization, and (iv) Electro-optic characterization of infrared detectors based on the engineered QDs. A detailed description of this approach is included in chapter 2.

The optical properties of engineered QD DWELL materials were determined by Photoluminescence (PL) and polarized spectral response of the QDIP detectors. The structural property is determined by X-ray diffraction (XRD) measurements. The surface morphology of the QDs was imaged and evaluated by atomic force microscopy (AFM). The detailed dot geometry, stain distribution and interface diffusion is imaged and evaluated by TEM and scanning TEM (STEM). The electrical behavior of processed detectors was investigated by current-voltage (I-V) measurements. Detector performance was characterized by spectral response, responsivity and detectivity measurements.

For the SK-QDIP, InAs QD with $In_{.1}Al_{.15}Ga_{.75}As$ quantum well shows the best PL intensity yield. The s-to-p polarization ratio was increased to 37%, compared to the 10% in conventional quantum dot detectors. The TEM image shows an engineered SK quantum dot with a reduced base of 12 nm and an increased height of 8 nm, compared to the conventional quantum dot with base of 17 nm and height of 4 nm. The infrared photodetector fabricated from this material shows a peak photodetectivity of 1×10^{9} cmHz$^{1/2}$/W at 77K for a peak wavelength of 4.8 μm and 1×10^{7} cmHz$^{1/2}$/W at 250K for a peak wavelength of 3.2 μm. The highest BLIP operating temperature increased to 150 K. The dark current density is as low as 2×10^{-4}A/cm^{2} and the photocurrent gain is 100 at the optimal operating bias.

For the SK-QD QDIP detectors, there are 3 designs: (1) two layers of 0.5 ML InAs evenly embedded in 5.1 nm GaAs quantum well. The active region consists of 10 periods of SML QDs separated by 50 nm $Al_{.16}Ga_{.84}As$ barrier is sandwiched by 1000 nm bottom and 200 nm top N+ GaAs contact layer. The STEM images show that the SML-QD with height to base aspect ratio as 8nm/6nm when growth temperature as 480 °C, and with height to base aspect ratio as 8nm/25nm when growth temperature as 540 °C. The SML-QDs have increased interface diffusion under high growth temperature. The s-to-p ratio of polarized spectral response is 9% when growth temperature as 480 °C and close to 0 when growth temperature as 540 °C. But since GaAs QW require high growth temperature for high crystal quality, the QDIP with the SML-QD grown under 540 °C

36

has the highest responsivity of 0.40 A/W and detectivity 5×10^8 cmHz$^{1/2}$/W under 0.25 V bias and 77K with peak wavelength as 10.3 μm.

(2) Based on the structure of design (1), two layers of 0.5 ML InAs evenly embedded in 5.1 nm In$_{.1}$Ga$_{.9}$As quantum well instead of the previous GaAs QW. Since In$_{.1}$Ga$_{.9}$As material requires low growth temperature for high crystal quality, the SML-QD growth temperature is kept as 500 °C. This QDIP has peak wavelength as 10.2 μm with narrower full width of half maximum (FWHM) than the previous design. The detector peak wavelength does not shift under various bias, showing the strong bound-to-bound intersubband transitions. The highest operating temperature is 90K. These factors demonstrate that the In$_{.1}$Ga$_{.9}$As QW has improved SML-QD 3D quantum confinement and has prevented interface diffusion between QD and QW.

(3) Based on the structure of design (1), four layers of 0.3 ML InAs evenly embedded in 5.1 nm In$_{.15}$Ga$_{.85}$As quantum well, and 2 nm Al$_{.22}$Ga$_{.78}$As and 48 nm Al$_{.07}$Ga$_{.93}$As as the barrier. The SML-QD growth temperature is kept as 500 °C. The STEM image shows the SML-QD with small base width as 4nm and height as 8nm. The s-to-p ratio of polarized spectral response is increased as 33%, closer to the 3D "artificial atom" property than previous designs.

1.6 Conclusion

We introduced the general physics of IR radiation, the concept of black body radiation and the absorption characteristics of IR radiation in the atmosphere. General concepts concerning infrared detection were presented followed by a description of different technologies for infrared imaging. One of the main requirements for the third generation FPAs is the non-cryogenic operation temperature. The QDIP is an alternative novel technology, which overcomes some shortcomings of thermal imagers and conventional photon detectors, has normal incident, long carrier lifetime, low dark current, and high operation temperature. The dot formation of SK and SML QDs are described, engineered QD with small base diameter and high height and less interface intermixing will have enhanced 3D quantum confinement and normal incident absorption. The engineered QDs will not only improve the performance of QDIP

detector, but also have wide applications at QD lasers, nanostructure device, and quantum computing.

CHAPTER 2 EXPERIMENTAL METHODS

2.1 INTRODUCTION

As mentioned in section 1.5, the experimental methods of the dissertation are divided into four main areas. They are (i) Epitaxial growth of engineered QDs by molecular beam epitaxy (MBE), (ii) Optical Characterization (iii) Structural characterization, and (iv) Electro-optic characterization of infrared detectors based on the engineered QDs. A detailed description of the method and materials used are included in this chapter.

The optical properties of engineered QD DWELL materials were determined by photoluminescence (PL) and polarized spectral response of the QDIP detectors. The structural property is determined by X-ray diffraction (XRD) measurements. The surface morphology of the QDs was imaged and evaluated by atomic force microscopy (AFM). The detailed dot geometry, stain distribution and interface diffusion is imaged and evaluated by TEM and scanning TEM (STEM). The electrical behavior of processed detectors was investigated by current-voltage (I-V) measurements. Detector performance was characterized by spectral response, responsivity and detectivity measurements.

2.2 Epitaxial Growth

2.2.1 Molecular Beam Epitaxy

Molecular beam epitaxy (MBE) was invented in the late 1960s as a means of growing high-purity epitaxial layers of compound semiconductors by one atomic layer at a time [1]. MBE can produce high-quality layers with very abrupt interfaces and good control of thickness, doping, and composition. It is a valuable tool in the development of sophisticated electronic and optoelectronic devices.

The growth chamber of a generic MBE system and several of its subsystems are illustrated in Figure 2.1 [1][2]. The wafer sits at the center of the chamber facing to the several elemental cells. Each cell contains one ultra-pure element, and the entire chamber is under ultra high vacuum, with a background pressure around 10^{-10} Torr. The cells are heated until the source material begins to evaporate or sublimate. There is a shutter in front of each cell that is used to control whether that element is allowed to reach the wafer surface. The wafer is heated to 400 - 650 °C during growth, which gives atoms on the surface sufficient mobility to move around and find sites of relatively low energy. For a perfect crystal such as a semiconductor, the crystal structure can be maintained. MBE is a modern technique used in research to grow nanostructures with precisely controlled compositions.
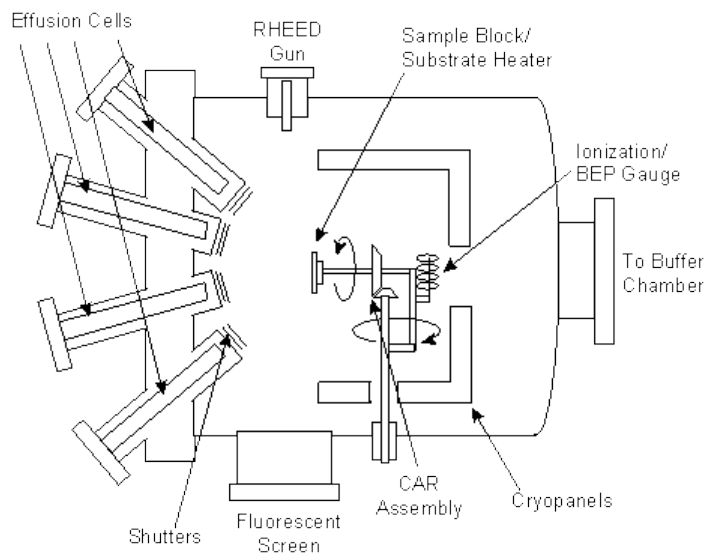
Figure 2.1 Diagram of a typical MBE system growth chamber

As shown in Figure 2.2, the growth chamber is equipped with several tools for in situ monitoring of growth process: Reflection High Energy Electron Diffraction (RHEED) gun, pyrometer for measuring substrate temperature and ion gauge for monitoring flux pressure during the growth process. Also it contains a residual gas analyzer (RGA) to monitor the pressure of residual gases such as H_2O, CO_2, N_2 and CO et al.

One of the most useful tools for *in-situ* monitoring of the growth is reflection high-energy electron diffraction (RHEED). It can be used to calibrate growth rates, observe removal of oxides from the surface, monitor the arrangement of the surface atoms, determine the proper arsenic overpressure, give feedback on surface morphology, and provide information about growth kinetics. The RHEED gun emits ~10 KeV electrons which strike the surface at a shallow angle (~0.5-2 degrees), making it a sensitive probe of the semiconductor surface. Electrons reflect from the surface and strike a phosphor screen forming a pattern consisting of a specular reflection and a diffraction pattern that is indicative of the surface crystallography. A camera monitors the screen and can record instantaneous pictures or measure the intensity of a given pixel as a function of time.
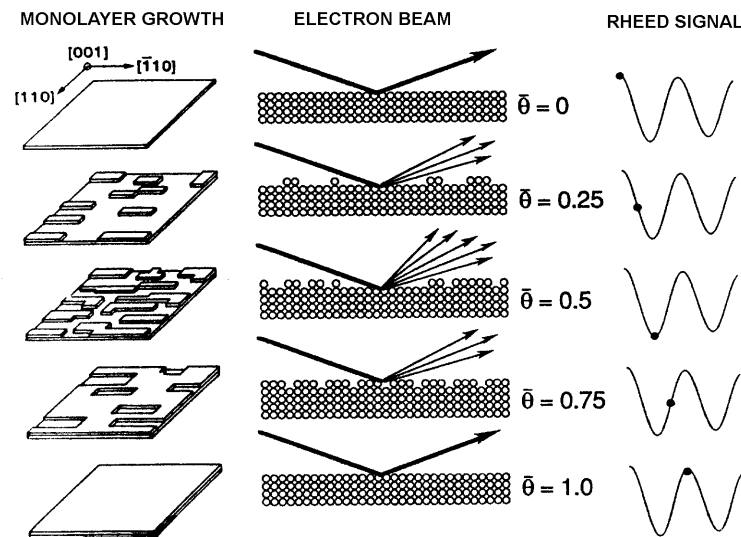
Figure 2.2 Illustration of the mechanism for RHEED specular spot oscillations during growth of a monolayer [3]

RHEED intensity oscillations can be used as an accurate, quick, direct measure of the growth rates in MBE. When growth is initiated on a smooth GaAs surface, the intensity of the RHEED pattern, especially the specular reflection, starts to oscillate. The oscillation frequency corresponds to the monolayer growth rate [4], where a monolayer (ML) is the thickness of one full layer of GaAs or AlAs. The oscillations can be explained by a layer by layer growth mode as demonstrated in Fig. 2.2. When a layer starts it is smooth and the specular spot is bright, but as the layer nucleates, islands form on the surface, and the specular spot dims. As the layer finishes, the islands coalesce into

a flat layer, and the specular spot intensity increases. The oscillation of the specular spot intensity has been attributed to the oscillating roughness of the layers changing the diffuse scattering [5], but the incident angle dependence of the oscillations [6][7] suggest that interference between electrons scattering from the underlying layer and the partially grown layer contribute to these oscillations. Because the angle of the sample can vary due to wobble in the CAR, the position of the electron gun should be fine-adjusted empirically to get the optimum incident angle.
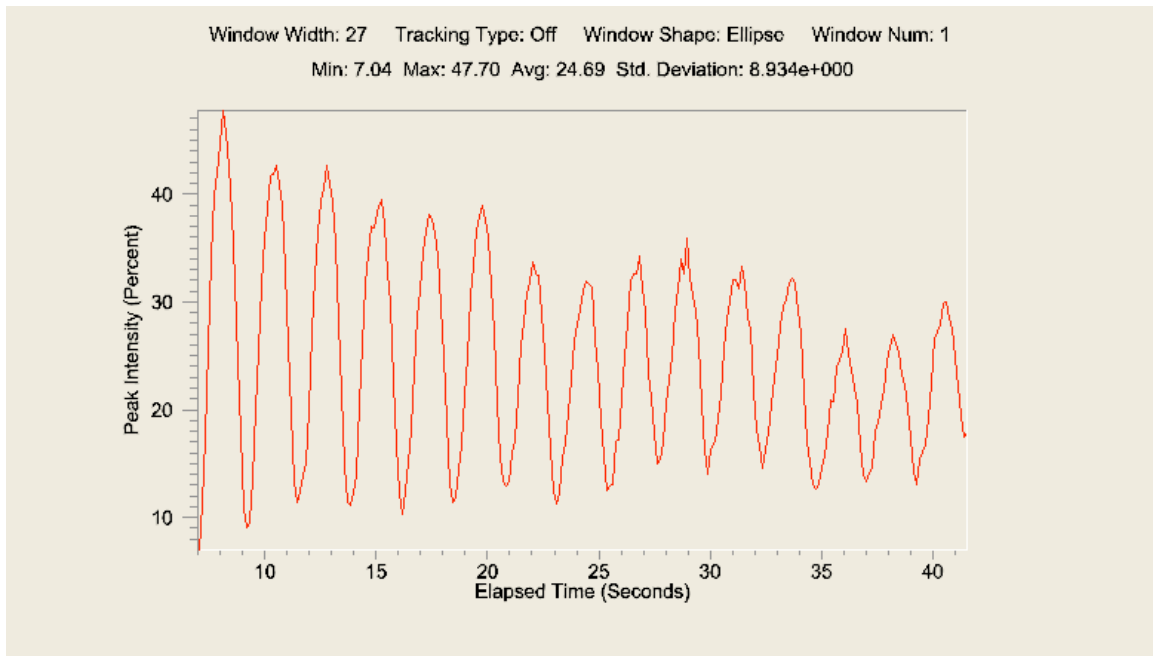
Figure 2.3 RHEED specular spot intensity oscillations at the growth of AlAs layers on a GaAs starting surface.

RHEED oscillations for AlAs growth starting on a GaAs surface are shown in Figure 2.3. At the start of growth, the intensity is the greatest since the layers are nearly atomically smooth. The magnitude of the RHEED oscillations damps because as the growth progresses, islands nucleate before the previous layer is finished. The amount of damping depends on both the growth conditions and the diffraction conditions (e.g. angle of incidence). The median intensity of the RHEED oscillations can also drop with time, since drifting in the electron beam due to charging effects and by changes in the surface as the growth progresses.

2.3 Optical Characterization

2.3.1 Photoluminescence
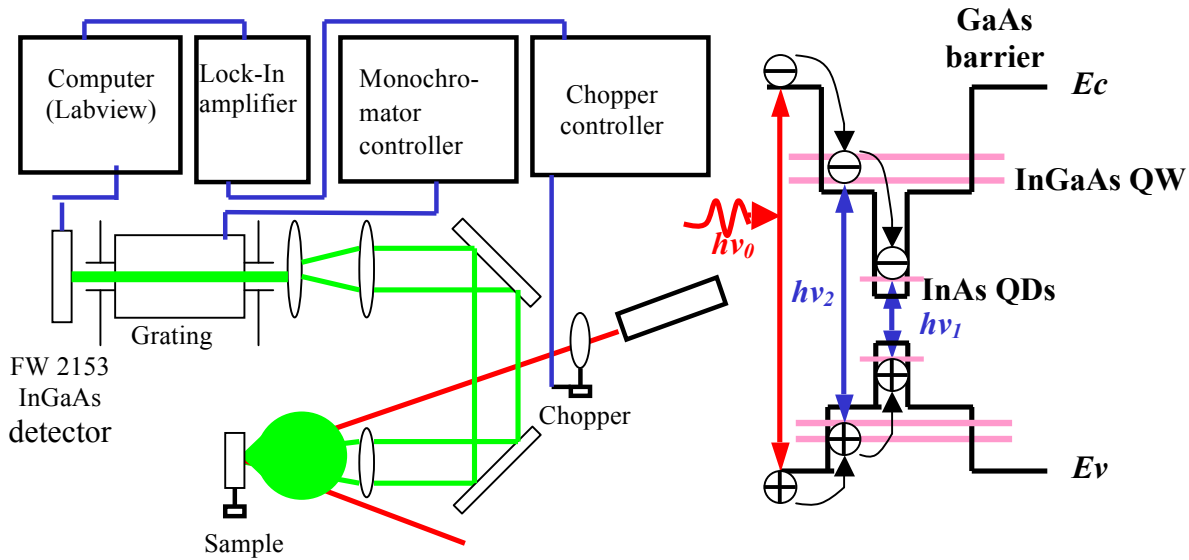
Figure 2.4 (a) The experimental measurement set up of the photoluminescence (PL)
(b) Energy level schematic of DWELL structure and the photoluminescence process

Figure 2.4 (a) is the experimental measurement set up of the photoluminescence (PL), in which He-Ne laser optical pumping is used to excite free carriers, and the spectrum of the resulting emitted light is collected by the FW 2153 InGaAs detector. Photoluminescence is a process involving photon excitation and subsequent radiative recombination. The high bandgap energy incident photons impinge on the sample causing the excitation of electrons from their ground level in the valence band to the upper levels of the conduction band, creating an initial distribution of photon-excited carriers. These photo-generated carriers quickly (0.2-100 ps) lose their energy by the emission of phonons, and reach lower energy states at the energy band extreme. The electrons, at the conduction band minimum, have a finite probability to recombine with holes at the valence band maximum. The recombination of electrons and holes may result in a radiative process. The emitted light called photoluminescence (PL). In the DWELL system, after the photoexcitation of electron-hole pairs in the barrier, carriers relax from the 3D barrier into 2D QW and 0D QD states. The electrons and holes can recombine by either radiatively or non-radiatively.

In the DWELL system, all of the light will be emitted with an energy exactly that of the QD or QW bandgap, neither more nor less. In practice, the transition energy may not be so distinct. This may be due to high doping, alloy fluctuations (which change the bandgap randomly depending on local composition), random variations in quantum dot size and defect. All of these effects lead to a broadening of the luminescence spectrum. The narrowness (linewidth, or FWHM) of the luminescence spectrum is often used as another measure of material quality, although it is usually correlated with PL intensity.

If the material quality is very poor, then there are many carrier traps (defects) that can provide nonradiative recombination of the electron and hole. This generates heat but not light. Therefore high material quality is usually correlated with high photoluminescence intensity. If all of the nonradiative traps are removed, then the radiative recombination will be the dominant form of recombination, emitting the most possible light. [7]

2.4 Structure characterization

2.4.1 Atomic Force Microscopy

Atomic force microscopy (AFM) provides a 3D profile of the surface on a nanoscale, by measuring *forces* between a sharp probe (<10 nm) and surface at very short distance (0.2-10 nm probe-sample separation). The probe is supported on a flexible cantilever. The AFM tip "gently" touches the surface and records the small force between the probe and the surface. An AFM measurement setup is mainly composed of a laser diode, a flexible cantilever, a piezoelectric motor, and a position-sensitive photodetector, as shown in Figure 2.5 (a). The repulsive Van der Waals force between the tip and the surface causes the cantilever to deflect. The motion of the cantilever is magnified by a laser beam reflection and recorded as the vertical displacement of the tip. In this way, the surface topography can be imaged by scanning the tip over the sample surface. AFM is typically operated in 3 basic modes [8]: contact mode, tapping mode and non-contact mode. Contact mode (< 0.5 nm probe-surface separation) is a fast and convenient way of imaging a relatively hard surface, but the drawback for this mode is that there are large constant lateral forces on the sample as the tip is "dragged" over the surface, can damage or deform soft samples. In tapping mode (0.5-2 nm probe-surface separation), the cantilever is oscillated at its resonant frequency (often hundreds of kilohertz), and the tip gently taps the surface with

a significantly reduced contact time. Tapping mode is thus extremely useful for topographical imaging of soft samples, but slower scan speeds is needed.

In non-contact mode (0.1-10 nm probe-surface separation), the probe does not contact the sample surface, but oscillates above the surface during scanning. Using a feedback loop to monitor changes in the amplitude due to attractive VdW forces the surface topography can be measured. It has very low force exerted on the sample (10^{-12} N) and extended probe lifetime, but on the other hand, it produces generally lower resolution, contaminant layer on surface can interfere with oscillation, and usually need ultra high vacuum (UHV) to have best imaging. Figure 2.5 (b) shows SEM image of an AFM tip.

(a)   (b)
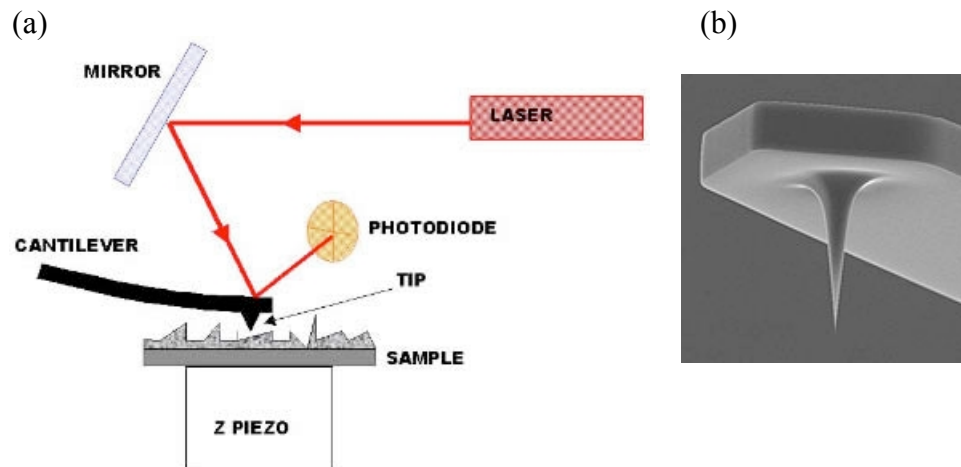
Figure 2.5 (a) An AFM measurement setup is mainly composed of a laser diode, a flexible cantilever, a piezoelectric motor, and a position-sensitive photodetector, (b) a SEM image of an AFM tip [9]

However there are limitations in achieving atomic resolution. The physical probe used in AFM imaging is not ideally sharp. As a consequence, an AFM image does not reflect the true sample topography, but rather represents the interaction of the probe with the sample surface. This is called tip convolution, as shown in figure 2.6. Commercially available probes are becoming more widely available that have very high aspect ratios. These are made with materials such as carbon nanotubes or tungsten spikes. However these probes are still very expensive to use for every day image analysis.
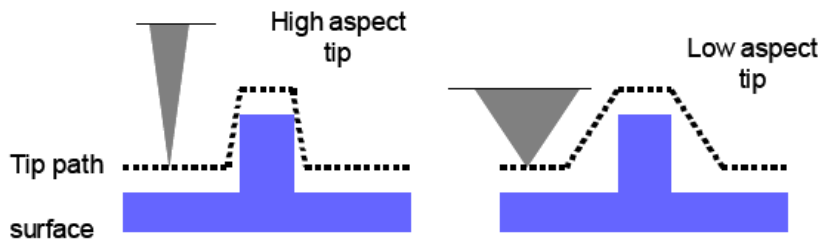
Figure 2.6 Ideally a probe (tip) with a high aspect ratio will give the best resolution. The radius of curvature of the probe leads to tip convolution. This does not often influence the height of a feature but the lateral resolution.

2.4.2 Transmission Electron Microscopy

TEM is a mocroscopy technique whereby a beam of electron is transmitted through an ultra thin specimen, interacting with the specimen as it passes through.

2.4.2.1 Transmission Electron Microscopy (TEM) Mode

JEOL 2010 FEG TEM STEM with 200 KV field emission has point resolution 1.9 Amstrongs, line resolution 1.4 Amstrong, and STEM ADF mode resolution 1.4 Amstrongs, owing to the small De Broglie wavelength of electrons. The instrument can produce a high-brightness 1 nm diameter probe and has an information limit of about 0.14 nm, which permits simultaneous high-resolution imaging and nanometer-level spectroscopic analysis.

Fig 2.7 shows almost all the important lens and aperture position in the TEM system. After the electron beam goes through several electron magnetic lens and apertures and hits the thin specimens, there are direct beam, elastically scattered electrons, and in-elastically scattered electrons. An integral part of an electron microscope is a viewing screen of some form, which translates electron intensity to light intensity, and which we observe or record photographically. The standard bright field TEM mode is also named as strain mode. The dark areas in the image indicate the atom with high lattice stain.
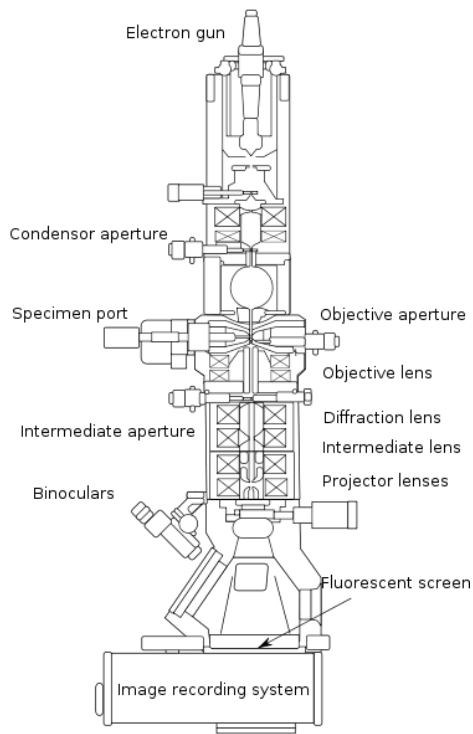
Figure 2.7 Layout of optical components in a basic Transmission Electron Microscopy

2.4.2.2 Scanning Transmission Electron Microscopy (STEM) Mode

In scanning TEM (STEM) mode, a tiny, convergent electron beam is scanned over a defined area of the sample. At each spot, the generated signal is simultaneously recorded by selected detectors, building up an image. Furthermore, such a convergent beam is used to gain a highly localized signal from the specimen in analytical TEM (e.g., EDXS, EELS), and thus the combination of STEM with analytical methods is a main application in practical work. In the STEM mode, more heavier of the chemical atomic mass more brighter of the image area. We can use STEM to get the chemical distribution information of the binary specimens.

2.4.2.3 Electron Energy-Loss Spectrometers (EELS)

When the electron beam traverses a thin specimen, it loses energy by inelastic scattering. Through EELS, inelastically scattered electrons can be separated. The Gatan Image Filter (GIF) contains the magnetic prism, which is designed with energy spectrometry as its primary function. Plasmon losses are a frequent cause of energy loss. Plasmons are collective excitations of the electron gas in the material and are typically

several electron Volts in magnitude. Phonon losses can also occur, which are much smaller, and the energy spread of the monoenergetic beam must be particularly small to detect such losses.

Use EELS we can get the chemical distribution information of ternary or quaternary compound specimens.

2.4.3 X-ray diffraction

X-ray scans are used to determine the structural properties of the epitaxial growth layers. X-rays are electromagnetic radiation with typical photon energies in the range of 100 eV - 100 keV. For diffraction applications, only short wavelength x-rays (hard x-rays) in the range of a few angstroms to 0.1 angstrom (1 keV - 120 keV) are used. Because the wavelength of x-rays is comparable to the size of atoms, they are ideally suited for probing the structural arrangement of atoms and molecules in a wide range of materials. The energetic x-rays can penetrate deep into the materials and provide information about the bulk structure.

Double crystal X-ray diffraction (XRD) is a non-destructive technique for the structural characterization of thin crystalline films. X-rays interact with electrons in matter and are scattered in various directions by the atomic electrons. If distances comparable to the wavelength of the X-rays separate the scattering centres then interference between the X-rays scattered from particular electron centres can occur. For an ordered array of scattering centres this can give rise to interference maxima and minima.

In order to observe x-ray diffraction from a crystalline lattice, the Bragg condition must be satisfied (2.1). When the waves are scattered from lattice planes separated by the interplanar distance d, the scattered waves interfere constructively. The path difference between two waves undergoing constructive interference is given by 2d sin Θ, where Θ is the scattering angle. Therefore, Bragg's law is given as equation 2.1:

$$2d_{h,k,l} \cdot \sin\Theta = n\lambda \qquad (2.1)$$

Where $d_{h,k,l}$ is the distance between the atom planes (*h, k, l* are the Miller indices), Θ is the incident angle, *n* is the order of diffraction and λ is X-ray wavelength.

The Bragg condition depends on the angle of the incident x-ray beam as it enters the crystal lattice and the direction at which the diffracted beam exits the lattice (Figure 2.8). It is met only when the scattered waves from all the atoms in the lattice are in phase, and interfere constructively.
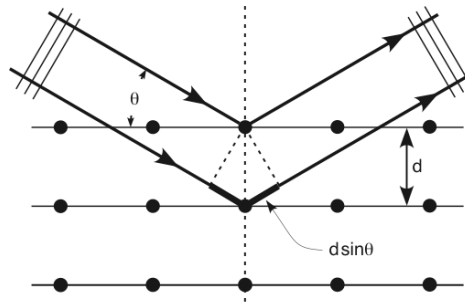
Figure 2.8 Schematic diffraction of X-rays in the crystal

RADS is a computer program for refining the parameters of multiple layer models of laminar materials by comparing experimental X-ray rocking curve data with simulated data. Mercury automates the process of fitting experimental X-ray rocking-curve data to simulated data. The data are compared using a robust error (cost) function and best-fit parameters are automatically calculated. RADS Mercury may be used to fit the following parameters such as layer thickness, composition, and strain.

The profile of the diffraction peak can reflect the structural details of the sample. The average period and sublayer thickness ratio of the multiplayer can be obtained from peak positions and intensities of various orders of diffraction peaks. As shown in Figure 2.9, the black rocking curve is the experimental scanning profile of a GaAs/InGaAs supperlattice structure, and the red rocking curve is the simulation data use RADS software. The detail of the structure and best-fit parameters are listed at Table 2.1. Use RADS simulation we can get the as-grown information of the epitaxial structure.
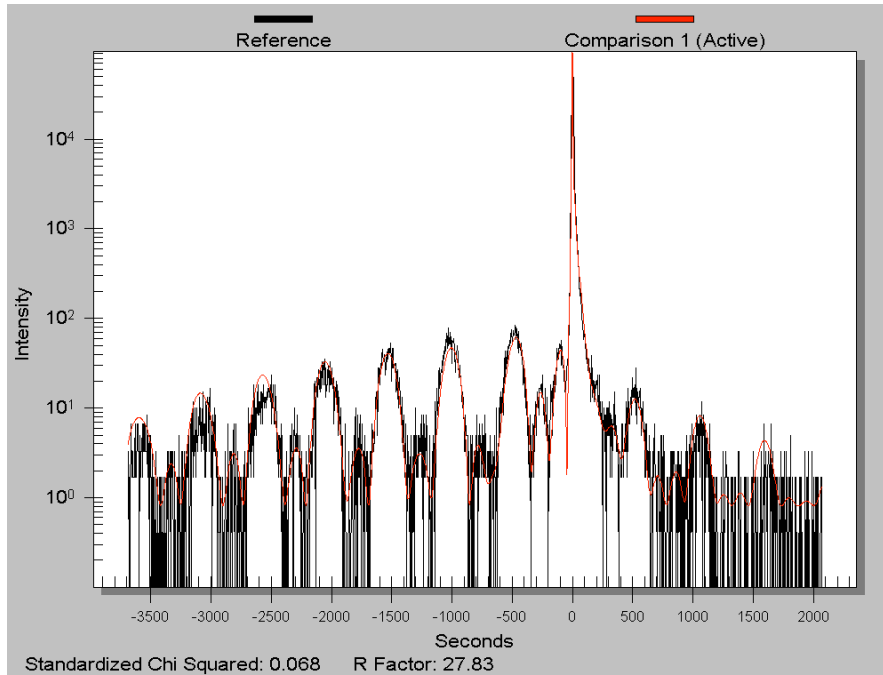
Figure 2.9 The XRD rocking curve of the InGaAs/GaAs supperlattice (black color) and rocking curve analysis by (RADS) Mercury simulation (red color).

Table 2.1 The designed parameters and the best-fit parameters of the RADS Mercury simulation for InGaAs/GaAs supperlattice #2721

Repeat	Material	Design		Simulation	
		Thickness (nm)	x	Thickness (nm)	x
3	GaAs	30		29.617	
3	$In_xGa_{1-x}As$	7	15%	6.74	14.57%
	GaAs substrate				

2.5 Electro-optic Characterization of IR detectors

2.5.1 Background-Limited Infrared Photodetecion (BLIP) Operating Temperature

There is a fundamental limit of detectivity equally applicable for the thermal and photon detectors. The best possible detector performance occurs when the incoming radiation fluctuation determines the noise of the detector. This regime called background-limited infrared photodetection (BLIP).

Carriers can be generated both thermally within the detector and by the incident background flux of IR radiation that is absorbed by the detector materials. The variance in the number of carriers on the detector node is given by equation 2.2 [21]

50

$$\left\langle \Delta N^2 \right\rangle = N_{th} + N_\Phi \qquad\qquad (2.2)$$

where N_{th} is the number of thermally generated carriers, and N_Φ is the number generated by the incident background. The ultimate in detector performance is achieved when the noise generated by the system background flux is larger than any thermally generated noise within the detector. The detector is then said to exhibit background limited performance (BLIP). For an incident background flux, Φ_B photons/cm^2/s, the photon generated density of carriers is $n_\Phi = \eta_a \Phi_B \tau / t$, where η_a is the absorption quantum efficiency, τ is the lifetime of the relevant carrier, and t is the detector thickness. Thus, BLIP is achieved when $\eta_a \Phi_B \tau / t > n_{th}$.

2.5.2 Dark Current and Activation Energy

From a system design perspective, dark current of the detector is one of the key figures of merit. Dark current determines the maximum operating temperature for the detector for a given signal to noise ratio. In QDIPs, the prime source of dark current is thermionic emission of carriers from the quantum dots, while field assisted tunneling, interdot tunneling [10] and thermal generation of carriers in barrier regions are other important sources.

Dark current can be reduced by lowering the operating temperature or by increasing the energy barrier. The latter makes it difficult to extract the higher wavelength carriers out of quantum dots. Hence there is a tradeoff between longer peak wavelength and lower dark current in a typical QDIP design. Since the density of states in quantum dots should be "atomic-like", the dark current is expected to be lower for similar wavelengths, as compared to QWIPs. Doping concentrations inside the quantum dots have to be carefully controlled and optimized in order to have minimum dark current with high photocurrent levels.

Figure 2.10 is experimental measurement set up of the QDIP dark current. The fabricated QDIP device is covered by a cold Aluminum shell and sealed in the closed cycle helium cryostat. A copper cold finger connected with the device is controlled by the temperature controller. The semiconductor parameter analyzer HP 4145B can add bias on the device and collect the I-V signal with low system noise.

Since the dark current is mainly caused by thermal excitation, the energy spectrum is proportional to $e^{-(Ea/kT)}$, where E_a is the activation energy [11][12]. The slope of the log(dark current) vs 1/T curve represents E_a, then the activation energy of QDIP can be calculated.
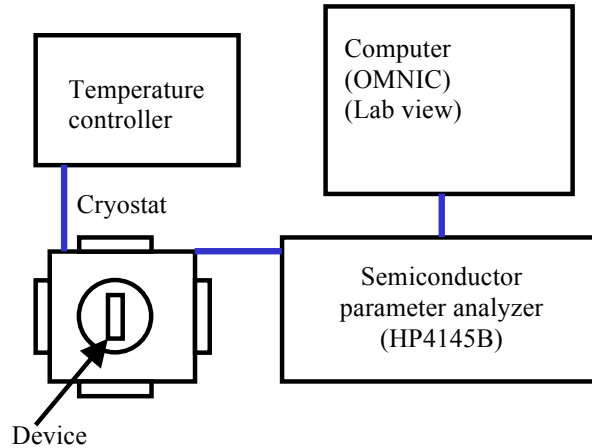
Figure 2.10 experimental measurement set up of the QDIP dark current.

2.5.3 Spectral Response

The experimental set up for the spectral response

$$E_{ex}(eV) = \frac{hc}{\lambda(\mu m)} = \frac{1.241}{\lambda(\mu m)} \qquad (2.3)$$

measurements is schematically shown in the Figure 2.11. A glow bar source within the Fourier Transform infrared (FTIR) spectrometer served as an infrared source. Infrared radiation is collected by a parabolic mirror and directed on the device surface. Device is mounted on a cold finger, which is connected with the Lakeshore temperature controller in 77-300K range. Measured signal is amplified by a Keithley 428 preamplifier and is supplied to FTIR for further processing. When the IR beam incidents upon the device surface, photons are absorbed by carriers at the ground state of QDs and get promoted to the higher conduction band. The peak wavelength of spectral response corresponds to the energy level difference between the ground state of QDs and the continuum energy level as equation 2.3.
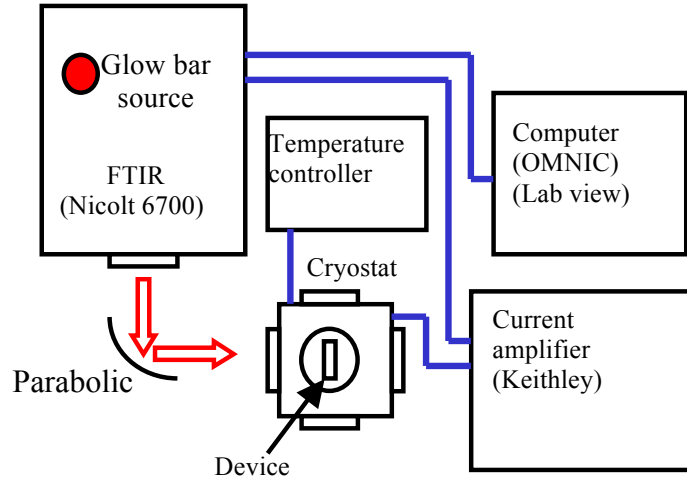
Figure 2.11 Schematic for the spectral response setup.

2.5.4 Polarized Spectral Response

For polarization dependent infrared spectral photoresponse measurements, the experimental setup schematic is shown as Fig. 2.12. The processed devices are polished with 45° side facet geometry, mounted on the 45° facet holder, wire-bonded on the pins of the leadless chip carrier (LCC). The front and back view of the processed devices in a leadless chip carrier (LCC) are shown in Fig. 2.12 (a). As shown in Fig. 2.12 (b), the device is loaded in the cryostat with KBr window and cooled to 77 Kelvin using liquid N_2. After the infrared radiation (IR) from Fourier Transform Infrared Spectroscopy (FTIR Nicolet 6700) is transmitted through the polarizer, it is vertically incident upon the 45° side facet of the substrate and device, and follows the zigzag ray path in it. The 428 Current Amplifier is connected with the cryostat to add bias to the device and give output signal back to FTIR and OMNIC software for processing the spectral photoresponse. As shown in Figure. 2.12 (c) and (d), The s-polarization electric field of the 45° side incident IR is equivalent to normal top surface incident radiation or TE mode, and the electrical field of p'-polarization is TE and TM polarization modes in equal shares [13]-[15]. So the p-polarization or TM mode can be extracted [16] using equation 2.4

$$E_p^2 = 2E_{p'}^2 - E_s^2 \qquad (2.4)$$

The intensity of the spectral photoresponse (equation 2.5) is proportional to the square of the electric field, so

$$I_p = 2I_{p'} - I_s \qquad (2.5)$$

(a)

(b)

Polarizer

P'

S

IR source

(c) Top normal incidence

S (TE)

Y (TE)

P'

45°

S (TE)

45° facet
side incidence

(d)

P'   P(TM)

QD

Y(TE) S(TE)

IR source

Z (P,TM)

X(S,TE)   Y(TE)
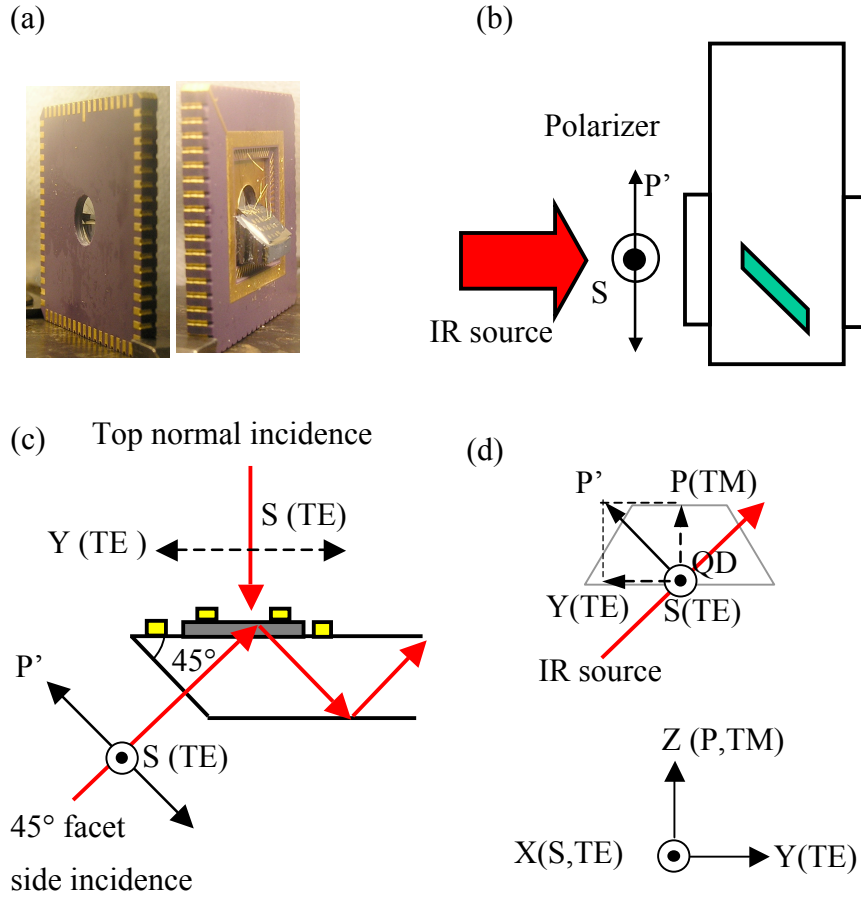
Figure 2.12 The experimental setup schematic of the polarized spectral response measurements, (a) The front and back view of the processed devices in a leadless chip carrier (LCC), (b) IR beam passed through the polarizer, and is vertically incident upon the 45° side facet of the substrate and device. (c) The s-polarization electric field of the 45° side incident IR is equivalent to normal top surface incident radiation or TE mode, and the electrical field of p'-polarization is TE and TM polarization modes in equal shares, (d) The s, p', and p-polarization electric field in a single QD.

Fig. 2.11 (d) shows s, p' and p -polarization electric field in a signal QD. The s and p polarized spectral response indicate the infrared absorption and quantum confinement of the QD at horizontal and vertical direction. The larger base diameter of the QD will cause weak horizontal quantum confinement and weak infrared absorption. The s to p ratio of the polarized spectral response more close to 1, the 3D quantum confinement of QD more close to the ideally "artificial atom". Additionally, the s to p ratio of the polarized spectral response should be correlated with the height to base geometry aspect ratio from the TEM image.

2.5.5 Responsivity

The photoresponsivity (R_i) is defined as the ratio of the output current generated per input optical power incident on the detector measured in Amperes/Watt. The experimental set up for the responsovity measurements is schematically shown in the Figure 2.13. In this system, infrared radiation from a black body source with controllable temperature is directed through a chopper onto the detector mounted inside the cryostat. Temperature of the cryostat is controlled by a Lakeshore temperature controller. The detector converts the incident radiation into an electrical signal, which is then amplified by a Keithley 428 preamplifier and measured using a computer controlled network analyzer. The chopper frequency is controlled through the chopper controller.

The photoresponsivity of the QDIP is given by equation 2.6:

$$R_i = \frac{I_o}{\int_{\lambda_1}^{\lambda_2} \frac{R(\lambda)}{R(\lambda_c)} L_e(\lambda,T) \frac{A_s A_d}{r^2} t F_F \, d\lambda} \qquad (2.6)$$

where $R(\lambda)$ is the normal spectral response intensity and $R(\lambda_c)$ is the peak spectral response intensity, A_s is the area of blackbody pinhole and A_d is the area of the detector, r is the distance between the center of the blackbody source and the detector, and t and F_F are the fill factor. L_e is the blackbody radiance, expressed as equation 2.7

$$L_e(\lambda, T) = \frac{2c^2 h}{\lambda^5 (e^{\frac{hc}{k\lambda T}} - 1)} \quad \left[\frac{watt}{cm^2 - sr \ \mu m} \right] \tag{2.7}$$

where c is the speed of light, h is the Planck's constant, e is the charge of an electron.
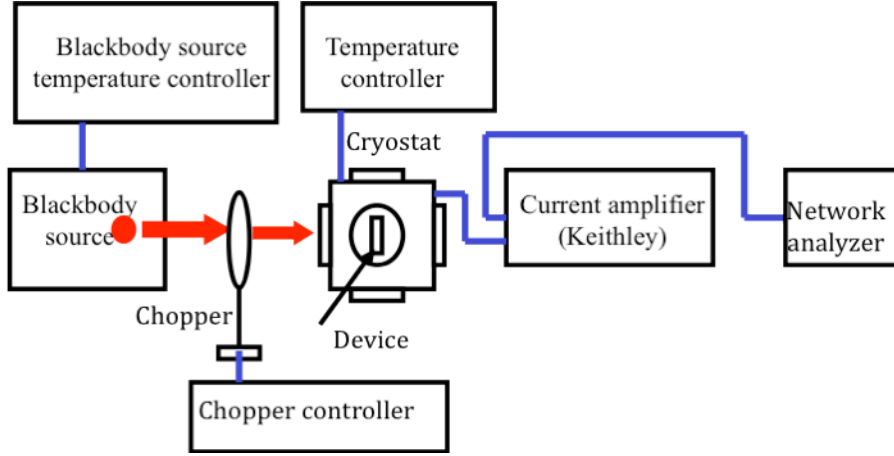
Figure 2.13 The experimental set up for the responsovity measurements

2.5.6 Detectivity

One important parameter used to evaluate the performance of infrared photodetectors is the specific detectivity D*, which is the signal-to-noise ratio normalized to the wavelength. The experimental set up for the detectivity measurements is similar as the responsivity but without the black body source and chopper.

The detectivity can be calculated using [17] equation 2.8,

$$D^* = \frac{R_i \sqrt{A_d \Delta f}}{i_{noise}} \tag{2.8}$$

where R_i is the responsivity, A_d is the mesa area of the QDIP device, and $(\Delta f)^{1/2}/i_{noise}$ is the noise current associated with the square root of noise frequency which is directly read out from the network analyzer.

2.5.7 Photoconductive Gain

To analyze the photocurrent gain, we need to discuss the noise gain G_n first. Using the current amplifier and the network analyzer, the noise current can be measured. To avoid 1/f noise, the noise current at 2000Hz was used for generation-recombination (GR) noise analysis [18]. The noise current contains both GR noise current and thermal noise (Johnson noise) current (I_{th}) using equation 2.9,

$$j^2_{noise} = 4eG_n I_d + I^2_{th} \qquad (2.9)$$

where e is the charge of an electron, and I_d is the dark current of the QDIP which can be measured using the HP 4145A semiconductor parameter analyzer. The thermal noise current can be calculated using equation 2.10,

$$I_{th} = \sqrt{\frac{4kT}{R}} \qquad (2.10)$$

where k is the Boltzmann's constant, T is the absolute temperature, and R is the differential resistance of the QDIP, which can be extracted from the slope of the dark current. From the experimental data, the thermal noise current is much less then the GR noise current and can be ignored. So the noise gain can be expressed as equation 2.11,

$$G_n = \frac{j^2_{noise}}{4eI_d} \qquad (2.11)$$

Following Liu's expression [19] noise gain for quantum well with the QD filling factor (F), the noise gain is related to the electron capture probability (P_c) by a QD as equation 2.12,

$$G_n = \frac{1}{FNP_c} \qquad (2.12)$$

where N is the number of QD layers, and the average value of the QD filling factor (F) is 0.35. We combine Beck's gain expression [20], which has been experimentally verified by Schönbein, the photoconductive gain is expressed as equation 2.13,

$$G_{ph} = \frac{1 - P_c / 2}{FNP_c} \qquad (2.13)$$

57

If the capture probability is much less than 1, as a good approximation, the photocurrent gain and the noise gain are equal in this device.

From the equation 2.12, the higher the photocurrent gain, the lower the capture probability of carriers, which indicates the QDIP has long carrier lifetime.

2.6 Conclusion

In this chapter, a detailed description of characterization techniques used in this work and their applications for structural, optical and optoelectrical characterization of as-grown materials and processed devices was presented. Physical foundations underlying x-ray diffraction, photoluminescence, atomic force microscopy and Auger electron spectroscopy were discussed. A schematic of experimental setups used for spectral response, PL, and responsivity measurements were presented.

In this chapter we discussed growth, processing and characterization of InAs/GaSb SL infrared single-pixel detectors. Detailed description of characterization techniques used in this work and their applications for structural, optical and electrical characterization of as grown materials and processed devices were presented. Physical foundations underlying X-ray diffraction, atomic force microscopy and transmission measurements were discussed. Schematics of experimental set up used for spectral response, transmission, and responsivity measurements were presented.

CHAPTER 3 ENGINEERED STRANSKI-SRASTANOV QUANTUM DOT INFRARED PHOTODETECTOR

3.1 INTRODUCTION

As mentioned in section 1.4.3.2 and 1.4.3.3, due to Stranski-Krastanov (SK) growth technology and the subsequent capping growth, the conventional SK QDs with pancake shape inhibit the full exploitation of the 3D "artificial atom" property. This is mostly due to the fact that the epitaxially grown quantum dots tend to be "pancake" shaped due to the flattening of the dots via intermixing during the growth of the capping layer and the loss of discrete quantum mechanical confinement.

In this chapter, we demonstrate the improvement in the high operating temperature and the s-to-p ratio of the polarized spectral response in an engineered Stranski-Krastanov quantum dot-in-a-well- (DWELL-) based infrared photodetector. This improvement was achieved through engineering the dot geometry and the quantum confinement via post growth capping of the quantum dots (QDs) with select overlying materials under various growth conditions. The effect of the capping procedures was determined by examining the optical properties of the QDs such as photoluminescence and the s-to-p ratio of the polarized spectral response in the QDIP detector, and structural properties of the QDs such as AFM and TEM.

Engineering of the geometry and the potential confinement of InAs quantum dots (QDs) using post growth capping with $In_{.15}Al_{.1}Ga_{.75}As$ is studied. By examining the dot geometry using TEM, quantum dots with a reduced base of 12 nm and an increased height of 8 nm are observed, therefore the dot height to base aspect ratio is reached to 0.67, which is much higher than the conventional SK dot with the aspect ratio of 0.24 (with height 4 nm/ base 17 nm). The TEM measurements were corroborated by measuring the polarized spectral response in an intersubband detector made with these quantum dots. The ratio of the polarized spectral response obtained in s-polarization (TE) to the photocurrent obtained in p-polarization (TM) increased from 10% in a conventional detector to 37% in the shape engineered QD detector.

These engineered QDs in a Well were then introduced into the active region of a DWELL IR photodetector. The infrared photodetector shows the highest operating

temperature is increased to 250K, the peak photodetectivity of 1×10^9 cmHz$^{1/2}$/W at 77K for a peak wavelength of 4.8 μm, and 7.2×10^7 cmHz$^{1/2}$/W at 250K for a peak wavelength of 3.2 μm. The dark current density is as low as 6.3×10^{-7}A/cm^2 (V$_b$=7V) and 2×10^{-4} A/cm^2 (V$_b$=12V) at 77 K, and the photoconductive gain is 100 (V$_b$=12V) at 77 K.

3.2 Molecular Beam Epitaxy growth

3.2.1 In$_{.15}$Al$_{.1}$Ga$_{.75}$As Capping

As we introduced in Chapter 1, when uncapped QDs are buried by additional epi-layers, they get flattened along the vertical direction and elongated along the lateral direction [1] due to the interface intermixing and diffusion process between the QDs and the capping materials. Both of these effects result in low height to base aspect ratio of QDs, loss of discrete energy confinement levels, and inhibit QDs from behaving like "artificial-atoms" by modifying the density of states and suppressing interesting phenomenon like the phonon bottleneck. Additionally, the intermixing of the QD's material with the capping layer creates a compositional gradient above and between the QDs. This diffusion gradient gives carriers a pathway to leak out, reducing the carrier lifetime and consequently leads to higher dark current and lower operating temperature [1].

For the engineered QDs, we need to prevent the QDs from intermixing with the capping layers. The diffusion processes involved in the intermixing between the QDs and the capping material can be controlled through several means: interfacial-strain engineering, mechanical diffusion barrier, and chemical diffusion retardant, and/or deposition kinetics.

To prevent the quantum dots from intermixing with the capping layers, one needs to control the bulk and surface diffusion processes involved in the intermixing between the QDs and the capping material. A major contributor to the energy for intermixing comes from the interfacial strain. If an exchange between the adatoms and the previously deposited material forms a mixed compound, the intermixing will lower the interfacial strain.

Certain materials (e.g. Al) however, can act as mechanical diffusion barriers for the indium in InAs dots. In this project we utilized lattice mismatched AlAs-based compounds to coat the dots at various deposition temperatures to try to prevent diffusion.

An unfortunate side-effect of adding Aluminum into the capping layer is that it tends to increase the interfacial energy at the dot and can increase the very intermixing we are trying to prevent. Therefore, controlling the kinetics of intermixing, was of critical importance in this portion of the study. By controlling the temperature and rate of deposition one should be able to mitigate the enhanced diffusion generated by the increased interfacial energy.

Initial results verify that interfaces with less strain intermix less, due to a decreased availability of energy to drive diffusion. This is evidenced by the samples that have caps with a greater degree of lattice matching (e.g. InAlAs cap instead of AlAs). As mentioned above, Indium is less miscible in aluminum containing compounds than those without Al; therefore, this makes Al-compounds a natural capping material. This effect, however, has to be balanced against the increase in interfacial-strain introduced by the Al-In lattice mismatch.

To try to find a balance between competing processes described above, we employed a number of Al containing compounds in our study: AlAs, InAlAs, and InAlGaAs. Deposition kinetics (e.g. substrate temperature and deposition rate) has previously been shown to be key to quantum engineering studies [2]. The decrease of substrate temperature would seem the simplest way to decrease the diffusion length; and, therefore, intermixing; however, this would also disrupt crystalline quality.

3.2.2 Migration Enhanced Epitaxy (MEE) Capping

In order to allow lower temperature deposition, while maintaining high crystalline quality, we used migration enhanced epitaxy (MEE) technology [3]. This process gives the adatoms more time to settle into their final position before burial by the incident flux, thereby reduce chemical intermixing during the capping as opposed to MBE grown capping layers of the same materials.

Our initial tests have shown, however, that while MEE improves the PL for samples when compared to samples grown without MEE at the same temperature, it does not fully

61

overcome the low temperatures negative effects on crystalline quality. Additional experimentation is warranted, to perfect this technique, but it is unlikely to solve the intermixing problem by itself.

3.2.3 Optimizing of the Capping Materials and Growth Condition

The material for this capping study was grown using VG-80 solid-source molecular beam epitaxy (MBE) system with a cracked As_2 source. The reference sample is based on the previously optimized DWELL detector reported elsewhere [4]. All of capping study materials have a similar structure based on the reference sample shown in Figure 3.1 (a). Transmission electron microscope (TEM) image of the heterostructure is shown in Figure 3.1 (b). A 200 nm GaAs buffer layer was first grown at 590°C on (100) semi-insulating GaAs substrate, followed by a 50 nm undoped GaAs barrier. Next, the substrate temperature was lowered to 470°C, and 4 nm of $In_{.15}Ga_{.85}As$ was deposited, which comprises the first part of the quantum well, and a total of 2.8 ML of InAs was grown to form the wetting layer and QDs. Then for the second-half of the quantum well, 6nm of $In_{.15}Ga_{.85}As$ material was deposited. A 50 nm undoped GaAs barrier was then grown. And this active region was repeated 3 times. Silicon was used to directly dope the dots with one electron per dot in order to provide carriers for absorption.

The optimized DWELL heterostructure and Pyrometer-verified growth temperature
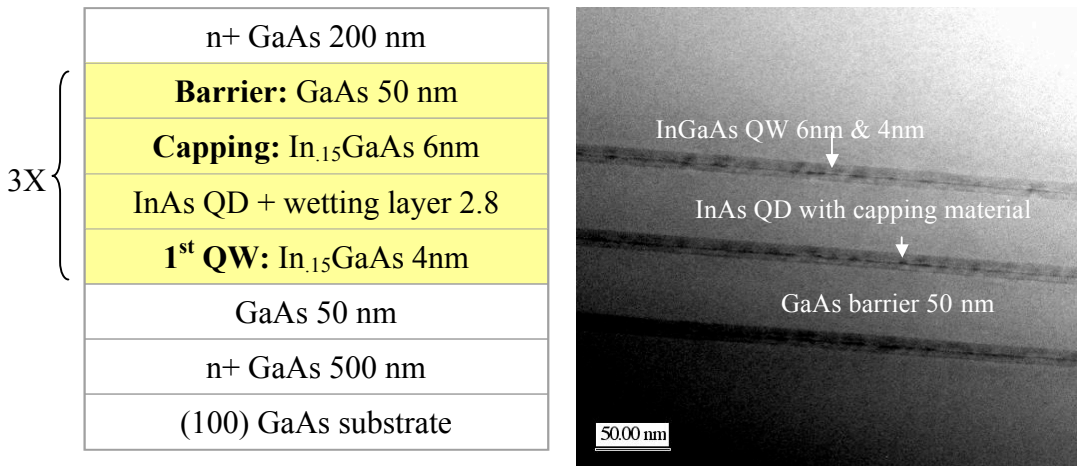
Figure 3.1 (a) Heterostructure schematic of the 3 periods InAs/InGaAs/GaAs DWELL reference sample (b) Cross-section Transmission Electron Microscopy (TEM) image of the reference sample

used in the capping study are shown in Table 1. The materials of the 1st part of QW, capping and barrier are selected, the substrate temperature was changed, and even the digital alloy (DA) QW and migration enhanced epitaxy (MEE) technology was involved.

Table 3.1. The growth condition and materials used in the capping study.

Barrier (nm)	1st part of Quantum Well (nm)	T (°C)	Capping	Run#	T (°C)	Pause (sec)	Thickness (ML)	Intensity of PL
GaAs	In$_{.15}$Ga$_{.85}$As	470	Same as QW	2319	470		-	Reference
GaAs	In$_{.15}$Ga$_{.85}$As	470	AlAs	2320	470		3	Low
				2324	350		3	Bad
				2328	470		2	Low
				2329	470		1	Low
				2323	350	MEE	3	Low
				2330	470	MEE	3	Bad
				2331	470	MEE	1.5	Bad
	DA In$_{.146}$Ga$_{.854}$As	470	Same as QW	2340	470		-	1×
	In$_{.15}$Ga$_{.85}$As	470	InAlGaAs	2338	470		1.5	1×
	DA In$_{.146}$Ga$_{.854}$As	470	Same as QW	2339	470		-	1×
Al$_{.3}$Ga$_{.7}$As	In$_{.15}$Al$_{.1}$Ga$_{.75}$As well /In$_{.15}$Ga$_{.85}$As strain bed	470	Same as QW	2341	470		-	2×
		510	Same as QW	2343	470		-	1/2×
	Double QW: InAlGaAs/InGaAs	470	DA In$_{.146}$Ga$_{.854}$As	2342	470		3	Low
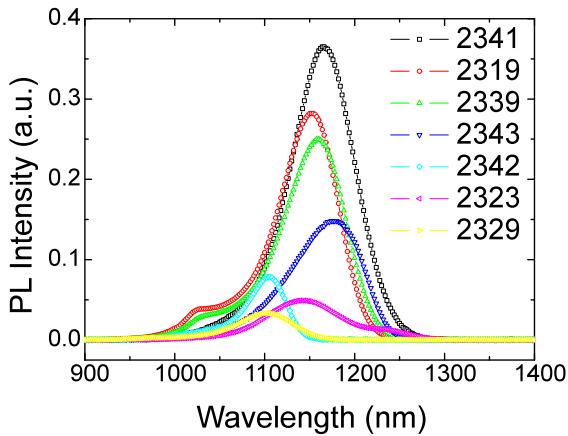
Fig. 3.2. PL intensity of the various capping study samples grown with optimized material and condition
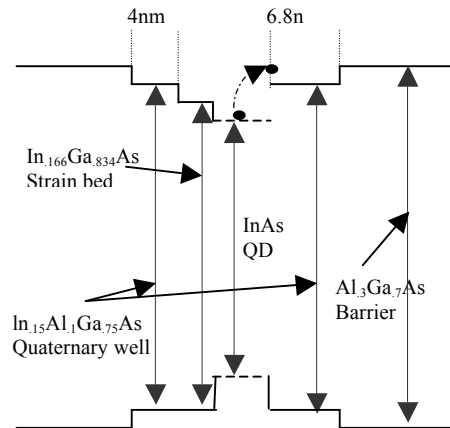
Fig 3.3. Energy band diagram for the best PL performance sample Run 2341.

3.3 Optical Characterization of Engineered QDs

3.3.1 Photoluminescence

The overall effect of the various techniques employed on the quality of the QDs can be determined by photoluminescence (PL) measurement. The PL measurement was undertaken using a He-Ne pump laser and an InGaAs detector, which has a response range from 800-1700nm at the room temperature. The PL intensity performance give us the information of the 3D quantum confinement, density of state, dot density, and has the same trend as the inhomogeneous strain distribution of the interface between dots and capping layer along the growth direction [5]. The higher the PL intensity, the lower the migration of Indium, the lower In/Ga interdiffusion, and the lower deterioration of the abrupt interfaces along the growth direction. The defect properties of the lateral/device are also revealed by PL.

Here, we report the results-to-date from employing four techniques mentioned earlier: interfacial-strain engineering, mechanical diffusion barrier, and chemical diffusion retardant, and/or deposition kinetics. Several top PL intensity performers are shown in Fig 3.2. The sample with the best performance, 2341, with an AlGaAs barrier, InAlGaAs QW, and InGaAs strain bed yielded the greatest increase in PL intensity, while maintaining QD high aspect ratios. The peak wavelength is at 1160 nm and the full width of the half maximum (FWHM) is about 80 nm. The band-structure of 2341 is shown in Fig 3.3. We believe that all desired mechanisms and techniques were employed on the best performance sample, the overall potential confinement was improved.

3.4 Structural Characterization of Engineered QDs

Characterization of the grown structure helps one to identify the material properties which strongly influence/impact the device quality and provides clues to approaches for optimization to achieve the highest device performance.

The grown structure is normally subjected to any of a variety of characterizations including AFM, TEM, and XRD. Defect properties of the material/device are revealed by PL. Crystal quality is revealed by the TEM. Double crystal x-ray diffraction (DCXRD) is utilized to map the lateral uniformity of the alloy composition and thickness across the wafer.

3.4.1 Atomic Force Microscopy

In order to obtain the dot density and uniformity of EQDs, based on best PL structure, we grew 4 samples of the InAs QDs and wetting layer/ $In_{.15}Al_{.1}Ga_{.75}As$ QW with 1nm $In_{.15}Ga_{.85}As$ strain bed / $Al_{.3}Ga_{.7}As$ barrier DWELL structure using VG-80 solid-source MBE system. The detail of the structures is shown in Fig 3.4. The top layer of QDs is uncapped for the atomic force microscopy (AFM) scanning. The difference between 4 designs is the repetitions of the full active region as 0, 1, 10 and 11. Therefore the exposed top layers of QDs are the 1st, 2nd, 11th and 12th layer in the structure.

The AFM scanning images of the 4 samples are shown in Figure 3.5. Each image has

InAs QDs & Wetting 2.8ML

Layer
1st QW $In_{.15}Al_{.1}Ga_{.75}As$ 4nm
Barrier $Al_{.3}Ga_{.7}As$ 50nm
Capping $In_{.15}Al_{.1}Ga_{.75}As$ 6.8 nm
InAs QDS & Wetting 2.8ML
DA InGaAs 1nm
1st QW $In_{.15}Al_{.1}Ga_{.75}As$ 4nm
Barrier $Al_{.3}Ga_{.7}As$ 50nm
GaAs buffer 0.2 μm
GaAs S.I. Substrate

0×
1×
10×
11×
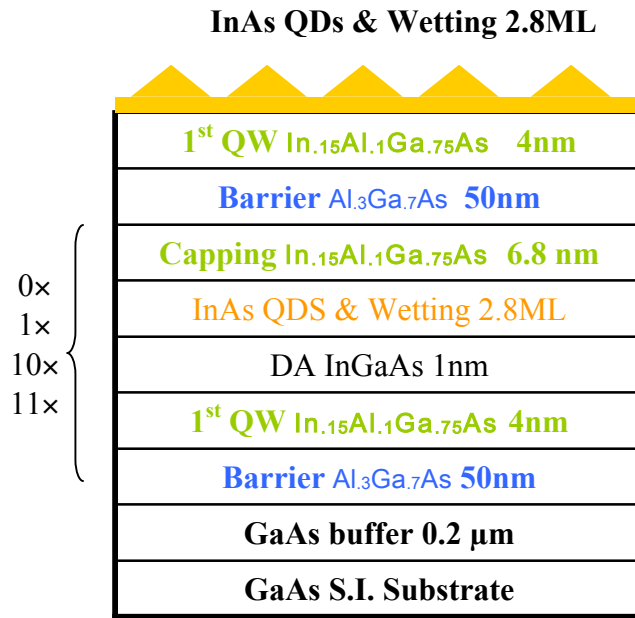
Figure 3.4 Heterostructure schematic of 4 samples of InAs/InAlGaAs/AlGaAs DWELL sample with exposed top QD layer.

the scanning area as 0.5 μm by 0.5 μm. The dot density is: first layer as 1.7×10^{11} cm^{-2}, second layer as 1.7×10^{11} cm^{-2}, eleventh layer as 1.4×10^{11} cm^{-2}, and twelfth layer as 1.5×10^{11} cm^{-2}. The dots at different layers have good uniformity with the average base diameter as 12 nm and height as 8 nm.

1st: 1.73×10^{11} cm^{-2} 2nd: 1.69×10^{11} cm^{-2}

11th: 1.41×10^{11} cm^{-2} 12th: 1.52×10^{11} cm^{-2}
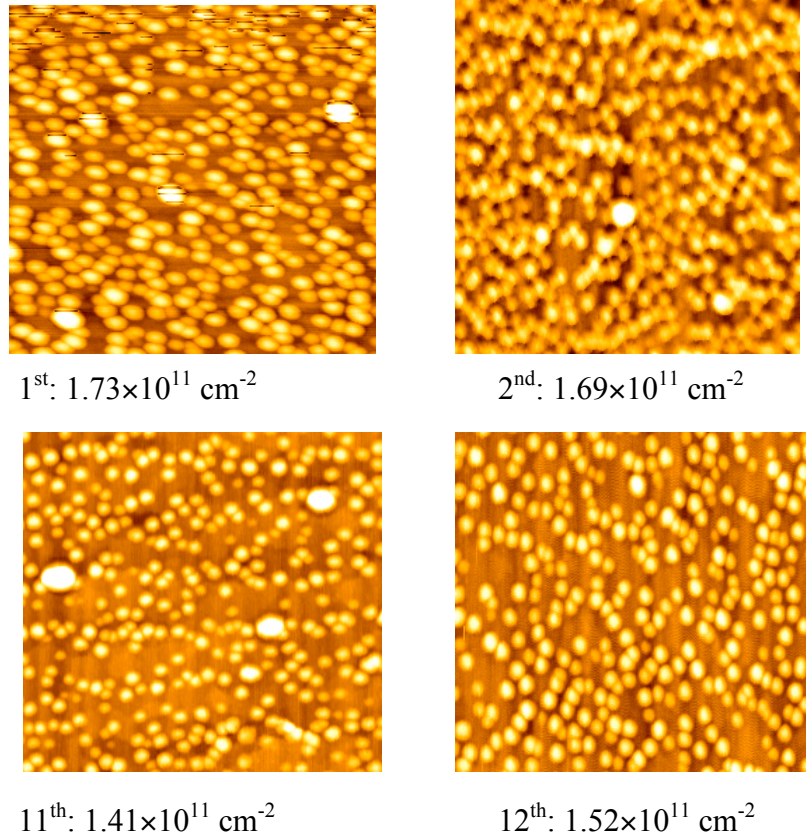
Figure 3.5: The AFM scanning images of the 4 samples with the exposed QDs at the 1st, 2nd, 11th and 12th layer.

3.4.2 Transmission Electron Microscopy

The TEM can observe the dot geometry and the interface diffusion between the dot and the capping material using the standard high resolution model.

In order to compare the dot geometry between the engineered QDs and the conventional QDs, two samples for this study were grown using V80 solid-source MBE system with a cracked As$_2$ source. A conventional DWELL detector (Sample A) was used as a reference sample. This sample has InAs quantum dots embedded in a 3 nm strain bed and 2.5 nm cap layer of In$_{.15}$Ga$_{.85}$As quantum well. This is capped with a 50 nm Al$_{.08}$Ga$_{.92}$As barrier and the active region was repeated 20 times. Sample B is an engineered QD sample repeat of the best PL structure, in which the InAs quantum dots were embedded in 4 nm lower and 6.8 nm upper In$_{.15}$Al$_{.1}$Ga$_{.75}$As

quantum well. A 1nm In$_{.15}$Ga$_{.85}$As strain bed was introduced between the lower QW and InAs QDs to increase the lattice strain. The barrier consisted of 50 nm Al$_3$Ga$_7$As layer and the structure was repeated 12 times. N+ GaAs layers were grown as top and bottom contacts to enable electrical characterization of the devices. The heterostructure schematic of the two samples is shown in Fig. 3.6.
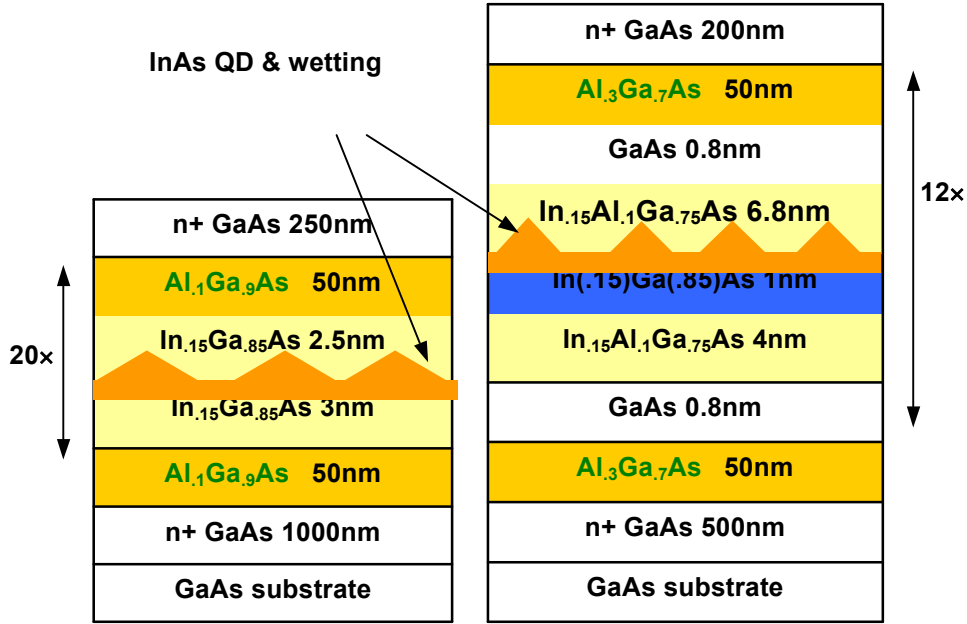
Figure 3.6: The heterostructure schematic of the quantum dot infrared photodetectors. Sample A is the conventional QDs detector and sample B is the engineered QDs detector.

Figure. 3.7 (a) is a high-resolution scanning TEM (STEM) image of the QD in the reference sample A. The bright area shows the indium atom distribution. It reveals that the dot is confined at the middle height of the quantum well and there are obvious indium diffusion between the surface of the dot and the surrounding bottom and top QWs. The QD is "pancake" shaped with a base width of ~17 nm and height of ~4 nm, and the height to base aspect ratio is 0.23. Fig. 3.7 (b) is a bright field high-resolution TEM image of the engineered QD in sample B. The dark area indicates the high strain area. It reveals that the dot is confined to the top half of the well and the QD cross section in the [110] azimuth is trapezoid shaped with a base width of ~12 nm and height of ~8 nm, respectively. The height to base aspect ratio is increased to 0.67. The edge between the

dot and the capping material is clear and no obvious diffusion is observed. Thus the engineered QDs design successfully prevents the diffusion processes involved in the intermixing between the QDs and the capping material, reduces the dot base width, increases the dot height, improves the 3-D dot confinement.
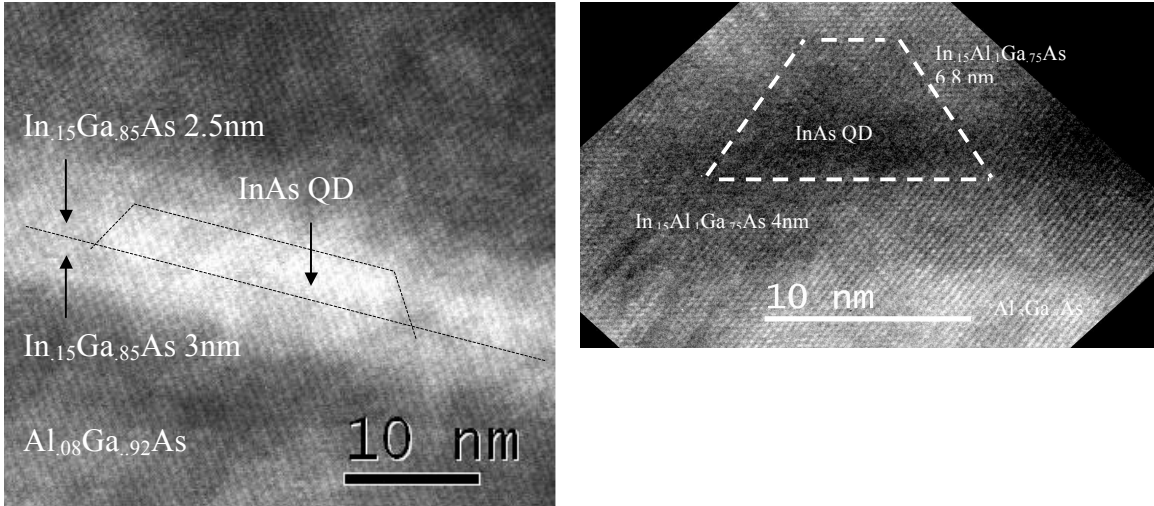
Figure 3.7 (a): The high-resolution scanning TEM (STEM) image of the QD in the reference sample A, (b): The bright field high-resolution TEM image of the engineered QD in the sample B.

Figure 3.8 is a standard model TEM image of the 12 repetitions engineered QD in the sample B. Using the analytical function of the TEM system, the Electron Energy Loss (EELS) Mapping can show the chemical atom contribution and the diffusion edge between different chemical layers. Figure 3.9 shows the original TEM image of the dwell cap structure and the EELS mapping of Indium, Gallium and Aluminum.

All above TEM images show: (1) the epitaxy layer was accurately grown as designed. (2) the height to base ratio of the single QDs is ~ 8nm/12nm. (3) the strain at the interface between QDs & QW is reduced. (4) the Indium is well contained in the wetting layer & QDs, and there is obviously no diffusion between the interface of QDs and Quantum well.
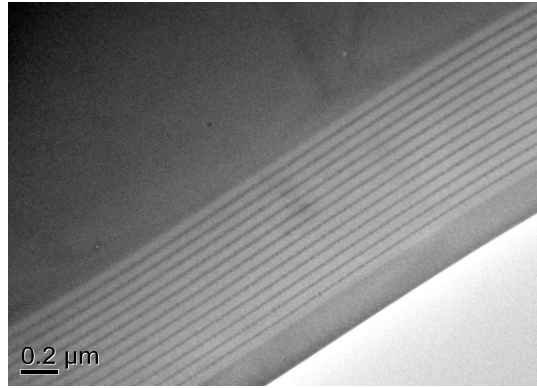
Fig. 3.8: Cross-section Transmission Electron Microscopy (TEM) image of the IR photodetector with 12 repetitions of the InAs/InAlGaAs/AlGaAs DWELL active region

(a)Original imagine

(b) In mapping

(c) Ga mapping

(c) Al mapping
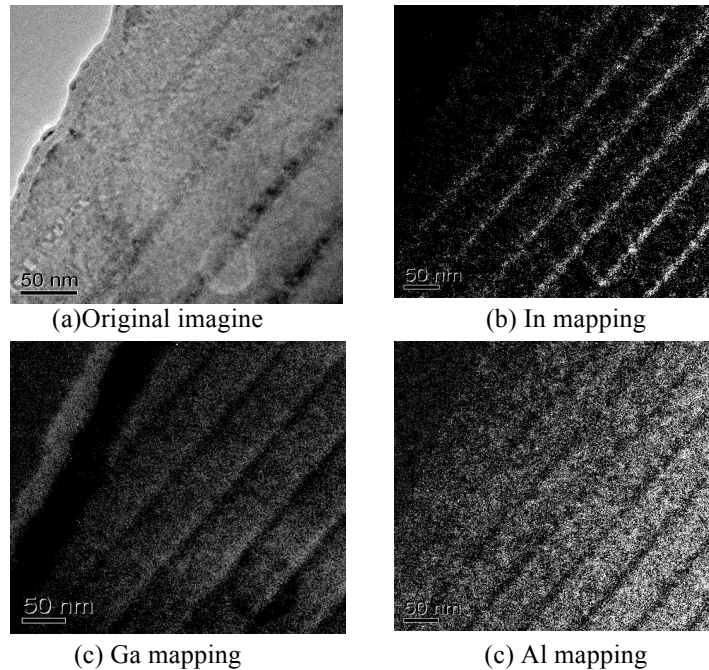
Fig. 3.9: The Electron Energy Loss (EELS) Mapping images: (a) Original imagine of the DWELL structure (b) Indium mapping imagine (c) Gallium mapping imagine (d) Aluminum mapping imagine

3.4.3 X-ray Diffraction

Figure 3.10 shows the XRD rocking curve of the engineered QDs sample B (black color) and Rocking curve Analysis by Dynamic Simulation (RADS) Mercury simulation (red color). RADS is a computer program for refining the parameters of multiple layer models of laminar materials by comparing experimental X-ray rocking curve data with

simulated data. Mercury automates the process of fitting experimental X-ray rocking-curve data to simulated data. The data are compared using a robust error (cost) function and best-fit parameters are automatically calculated. RADS Mercury may be used to fit the following parameters such as layer thickness, composition, and strain.

The designed parameters and the best-fit parameters of the RADS Mercury simulation are shown at Table 3.2.
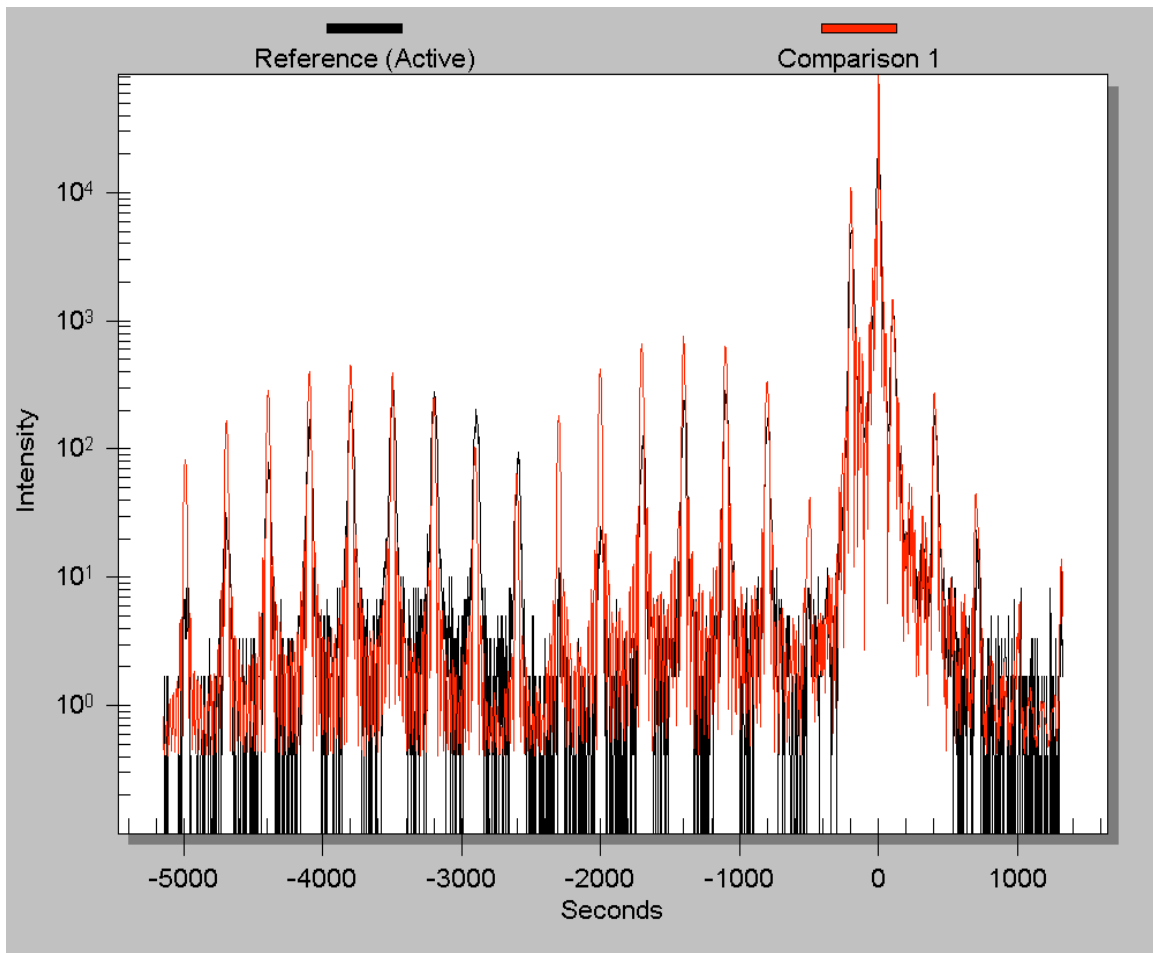
Figure 3.10 The XRD rocking curve of the engineered QDs sample B (black color) and Rocking curve Analysis by Dynamic Simulation (RADS) Mercury simulation (red color).

Table 3.2: The designed parameter and the best-fit parameter of the RADS Mercury simulation

Repeat	Materials	Design			RADS best-fit parameter		
		Thickness (nm)	x	y	Thickness (nm)	x	y
1	GaAs	200			200		
12	$Al_xGa_{1-x}As$	50	30%		50.27	32.24%	
12	GaAs	1			0.52		
12	$In_xAl_yGa_{1-x-y}As$	6.8	15%	10%	7.07	15.67%	10.66%
12	InAs	0.85			0.69		
12	$In_xGa_{1-x}As$	1	15%		0.71	14.85%	
12	$In_xAl_yGa_{1-x-y}As$	4	15%	10%	3.55	14.21%	8.42%
12	GaAs	1			0.52		
1	$Al_xGa_{1-x}As$	50	30%		50.21	33.24%	
1	GaAs substrate	2000					

3.5 Electro-optic Characterization of Infrared Detectors Based on Engineered QDs

3.5.1 Dark Current

From a system design perspective, dark current of the detector is one of the key figures of merit. Dark current determines the maximum operating temperature for the detector for a given signal to noise ratio. In QDIPs, the prime source of dark current is thermionic emission of carriers from the quantum dots, while field assisted tunneling, interdot tunneling and thermal generation of carriers in barrier regions are other important sources.

Dark current can be reduced by lowering the operating temperature or by increasing the energy barrier. The latter makes it difficult to extract the higher wavelength carriers out of quantum dots. Hence there is a tradeoff between longer peak wavelength and lower dark current in a typical QDIP design. Since the density of states in quantum dots should be "atomic-like", the dark current is expected to be lower for similar wavelengths, as compared to QWIPs. Doping concentrations inside the quantum dots have to be carefully controlled and optimized in order to have minimum dark current with high photocurrent levels.

(a)
TCAD MEDICI GRAPHICS
2319 Band-Diagram v(top)=0v v(bot)=4v

InGaAs QW 4nm & 5nm

n-GaAs 0.2u

n-GaAs 0.2u

InAs wetting 2nm
InAs QD 1e18 1nm

Potential (Volts)
Distance (Microns)

(b)
TCAD MEDICI GRAPHICS
2341 Band-Diagram v(top)=0v v(bot)=4v

AlGaAs barrier 48nm
GaAs smoother 1nm
InAlGaAs QW 4nm & 4nm
InAs QD 1e18 1nm
InAs wetting 2nm
InGsAs wetting 2nm

n-GaAs 0.2u

n-GaAs 0.2u

Potential (Volts)
Distance (Microns)

(c)
TCAD MEDICI GRAPHICS
2319 & 2341 dark current v(top)=0v v(bot)=-4Vto4v

☐ 2319 QD 1e18 with traps
☉ 2341 QD 1e18 with traps

log(I(bot) (Amps/um))
V(bot)(Volts)

Figure 3.11. (a) and (b) are the band diagram of Run# 2319 and Run# 2341. (c) The one dimensional
dark current of Run#2319 and Run# 2341.

72

The performance of sample #2341 (best PL sample) and #2319 (reference sample) from the table I is compared using a commercial software MEDICI that simulates the band diagram and the dark current data. Fig 3.10. (a) and (b) are the band diagram of #2319 and #2341. Fig 10. (c) is their one dimensional dark current. It is shown that the In$_{.15}$Al$_{.1}$Ga$_{.75}$As capping materials structure (#2341) has the much lower dark current. Both of the improved quantum confinement and higher barrier contribute to it.

In order to exploit the advantage of the engineered QDs, we grew and fabricated two IR photodetector with 12 repetitions of the InAs/In$_{.1}$Al$_{.15}$Ga$_{.75}$As/Al$_{.3}$Ga$_{.7}$As DWELL active region sandwiched between 500nm n^+GaAs bottom contact and 200nm n^+GaAs top contact using VG-80 solid-source MBE system. The details of the two structures are shown in Figure 3.12. The difference between the two designs is the Al$_x$Ga$_{1-x}$As barrier energy level. Sample #2509 has the barrier as Al$_{.3}$Ga$_{.7}$As, and sample #2508 has a Al$_{.1}$Ga$_{.9}$As barrier.

Standard processing techniques were then applied for the device fabrication. 450μm diameter circular mesa with GeAu top and bottom contact rings were formed to allow normal incidence measurement from the top window.

	n+ GaAs 200nm
	Al(.3)Ga(.7)As/Al(.1)Ga(.9)As 50nm
	GaAs 0.8nm
	In(.15)Al(.1)Ga(.75)As 6.8nm
12X	InAs QD & wetting 2.5 ML
	In(.15)Ga(.85)As 1nm
	In(.15)Al(.1)Ga(.75)As 4nm
	GaAs 0.8nm
	Al(.3)Ga(.7)As(#2509)/ Al(.1)Ga(.9)As(#2508) 50nm
	n+ GaAs 500nm
	GaAs substrate

Figure 3.12 The growth heterostructure of the 12 periods InAs/InAlGaAs/AlGaAs DWELL detector.

The experimental dark current of the QDIPs #2508 and #2509 are shown as Figure 3.13 (a) and (b). Both of them are lower than 1×10^{-9}A at the working bias range and are 2 orders lower than GaAs/AlGaAs QWIP detectors [6][7]. The flat zone shows the system noise level as $\sim1\times10^{-11}$A. Dark current can be reduced by lowering the operating temperature or by increasing the energy barrier. Since the #2509 has a higher energy barrier Al$_{.3}$Ga$_{.7}$As, it has a lower dark current then # 2508.

Low dark current means low thermonic emission of carriers and more unoccupied conduction band density of state, thereby more photons have the opportunity to be promoted to the higher conduction band.
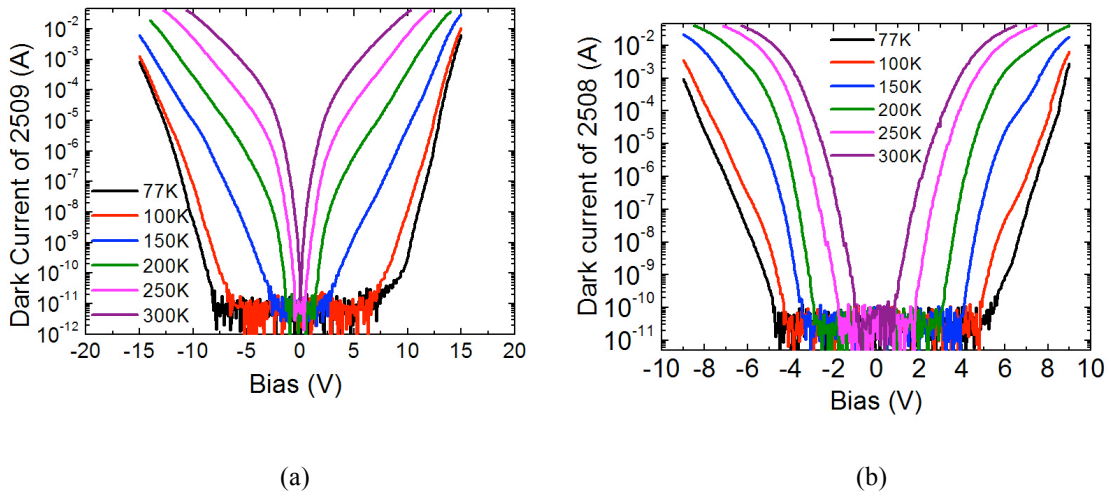
(a)   (b)
Figure 3.13 (a) the dark current of Run#2508, (b) the dark current of Run#2509.

3.5.2 Spectral Response

Without an extended well closer to the QD's energy level the long-wave response peak is suppressed at 4.8μm and 5.1μm in Figure 3.14 and Figure 3.15, but the mid-wave response peak at 3.8μm can still be clearly observed. The energy difference between the ground state level and the first excited level are 258meV and 243meV.

Additionally, this response can clearly be seen at temperatures up to 250K for #2509 and to 200K for #2508. Since those two designs have different barrier energy, their continuum energy level should be different. We recognize that one of this improvement in temperature could be attributed to the increase in barrier height. In addition, we

74

conclude from our electrical experiments that the dark current level was decreased due to improved quantum confinement within the QDs. And also, our reference QDIP sample InAs/In$_{.15}$Ga$_{.85}$As/Al$_{.1}$Ga$_{.9}$As structure has the highest operation temperature at 90K. So this data shows that this improvement in temperature and carrier lifetime is due to intermixing diffusion prevention and the leakage prevention.

Figure. 3.16 shows the # 2509 peak wavelength as a function of bias from 77K to 250K. The observed staircase effect is significant because it illustrates that as bias increases carriers confined at lower quantum levels are able to tunnel out and, therefore, peak wavelength of response increases with bias, implying significant tunability. This
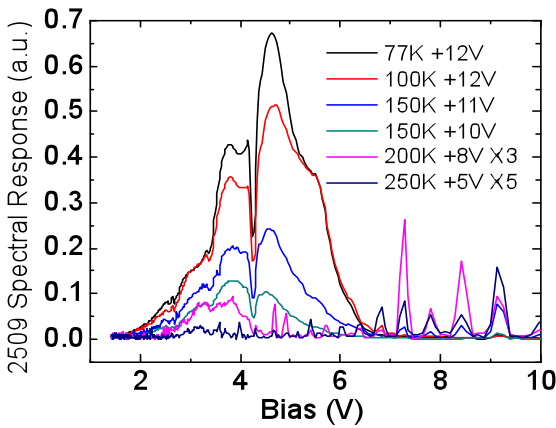
Fig. 3.14. #2509 spectral Response of a 300μm diameter window size device
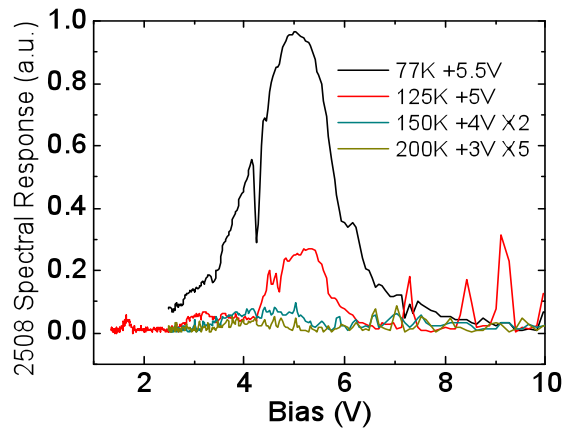
Fig. 3.15. #2508 spectral Response of a 300μm diameter window size device from 77K to 200K
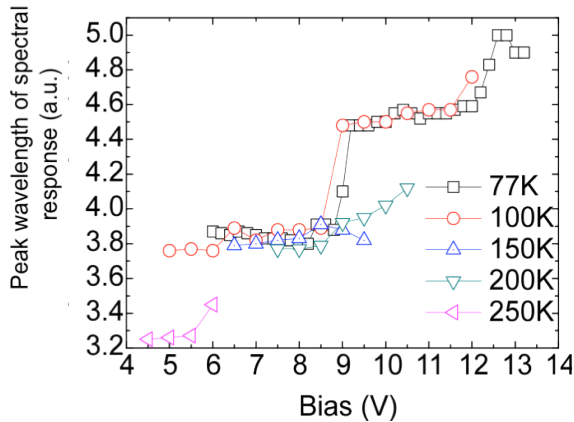
Fig. 3.16. #2509 Peak wavelength as a function of bias from 77K to 250K
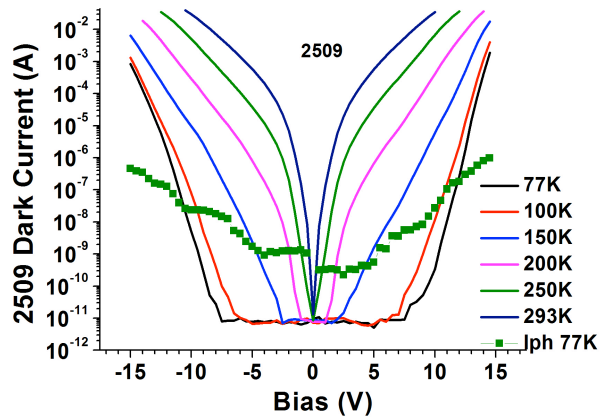
Fig. 3.17. #2509 Dark current from 77K to 293K and photon generation current at 77K under variation of bias

75

device has a wide bias-dependent peak spectral response in the range from 3.7μm to 4.8μm, that is suitable for multispectral imagery [7].

Figure 3.17 shows the #2509 dark current from 77K to 293K and the photon generation current at 77K under variation of bias. The BLIP condition is when the photon generation current larger than dark current. Analyzing with Figure 3.16, the highest BLIP operating temperature of #2509 is 150K.

3.5.3 Polarized Spectral Response

In order to demonstrate the advantage of the engineered QDs, three samples were compared with the s-to-p polarized spectral response. All of three samples for this study were grown using V80 solid-source molecular beam epitaxy (MBE) system with a cracked As_2 source.

A conventional DWELL detector (same as Sample A in section 3.4.2) was used as a control sample. Sample A has 2.0 ML InAs quantum dots embedded in 3 nm $In_{.15}Ga_{.85}As$ lower quantum well bed and 2.5 nm cap layer of $In_{.15}Ga_{.85}As$ quantum well. The DWELL structure is followed with a 50 nm $Al_{.08}Ga_{.92}As$ barrier and the active region was repeated 20 times. In the shape engineered QDs sample (Sample B), 2.8 ML InAs quantum dots were grown on a 4 nm $In_{.15}Al_{.1}Ga_{.75}As$ lower quantum well with 1nm $In_{.15}Ga_{.85}As$ strain bed. The QDs were capped with a 6.8 nm $In_{.15}Al_{.1}Ga_{.75}As$ upper quantum well to minimize intermixing. The barrier layer consists of 50 nm $Al_{.3}Ga_{.7}As$ and the active region was repeated 12 times. In the QWIP sample (sample C), the center 0.9 nm of the 6.4 nm GaAs QW is n+ doped as 1.75×10^{18} cm^{-3} sheet density. The barrier layer consists of 40 nm $Al_{.28}Ga_{.72}As$ and this active layer was repeated 50 times. All samples had a 500 nm n^+GaAs bottom contact layer and 200 nm n^+GaAs top contact layer. Standard processing techniques were then applied for the device fabrication. 450 μm diameter circular mesa with Ge-Au top and bottom contact rings were formed to allow normal incidence measurement from the top window.

All processed samples of A, B and C were polished with 45° side facet geometry, mounted on the 45° facet holder, wire-bonded on the pins of the leadless chip carrier (LCC) and loaded in the cryostat with KBr window and cooled at 77 Kelvin using liquid

N$_2$. The polarized spectral response is measured used the experimental setup described at session 2.4.4.

Fig. 3.18 (a) shows s and p polarization spectral response of reference sample A at 77 Kelvin (V$_b$=−4.5V). The s/p polarization spectral response ratio of the sample A is less then 10%. The inset shows the large dot base width causes the weak in-plan (TM) quantum confinement and in-plane infrared absorption. For the top normal incidence (TM) without gratings, more than 90% of signal is not utilized.

The results measured at 77 Kelvin (V$_b$=+13V) in Figure 3.18 (b) shows that the s/p polarization spectral response ratio of engineered QDs sample B increases to 37%, respectively. This is the highest *s/p* polarization ratio observed in a spectral response measurement for a QDIP device. A strong spectral response not only describes the high material quality of QDs, such as low defect and low trap center, but also the improved discrete quantum confinement, and less intermixing and leakage path of the interface between QDs and capping materials [8]-[11]. For conventional Stranski-Krastanov QDs, the *s* polarized quantum confinement is always less then the *p* polarized since the base width is always larger than the height [10]. But the improved *s/p* ratio as 37% indicates the decreasing of the dot base width and increasing of the dot height as shown in the inset, the in-plane (TE) quantum confinement and in-plane infrared absorption are dramatically improved compared to the vertical direction (TM).

Figure 3.18 (c) shows s and p polarization spectral response of QWIP sample C at 77 Kelvin (V$_b$=−4.5V). Since QW has no in-plane confinement, the s-polarization spectral response shows just noise. From the data listed at table I, the results of the s/p polarization spectral response ratio and the dot geometry height to base aspect ratio are corroborated each other, and the behavior of engineered QDs is closer to the 3-D "engineered atoms". The energy level of In$_{.15}$Al$_{.1}$Ga$_{.75}$As QW in sample B is higher than In$_{.15}$Ga$_{.85}$As QW in sample A, and engineered QDs have higher dot height, both of them cause the blue shift of engineered QD QDIP peak wavelength.
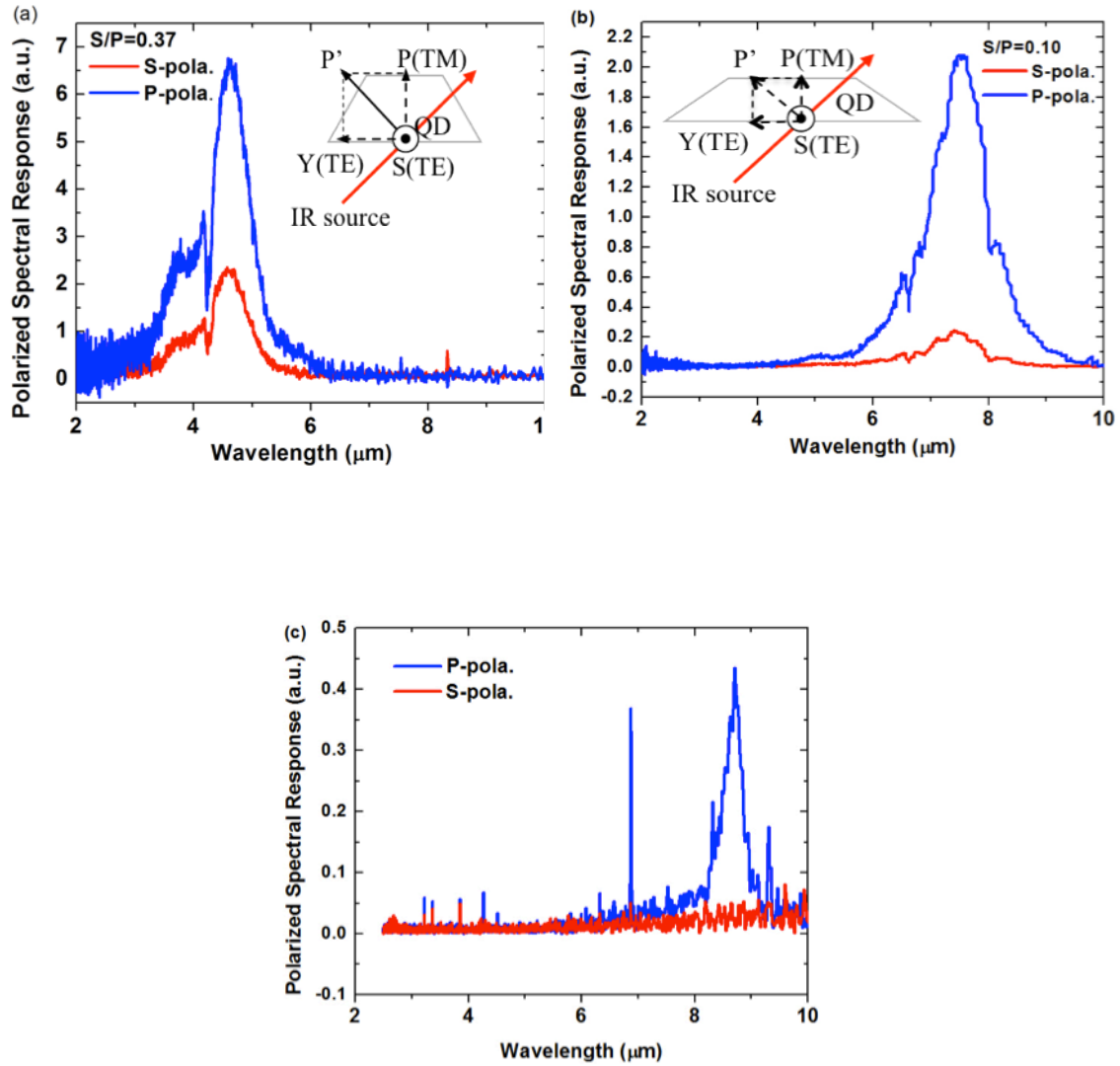
Figure 3.18: S and P polarization spectral response of (a) engineered QDs sample B at 77 K (V_b=13V), s/p=37%, (b) conventional QDs reference sample A at 77 K (V_b=−4.5V), s/p=10%, (c) QWIP sample C at 77 K (V_b=0.37V), s/p=0.

Table 3.3 Results of the s-to-p ratio of polarized spectral response and aspect ratio from TEM images

Sample #	A	B	C
Aspect ratio from TEM	0.23	0.67	-
S/P ratio of polarized	0.10	0.37	0

3.5.4 Responsivity

Figure. 3.19 (a) and (b) shows the peak photoresponsivity R_i as function of bias for different temperatures of #2509 and #2508. At 77K, a R_i of 0.12 A/W was observed at 12V for #2509. A strong temperature-dependent photoresponsivity R_i was also observed. This is due to the temperature dependence of photocurrent gain G_{ph}. Since the #2509 has a higher energy barrier $Al_{.3}Ga_{.7}As$, its working bias range is higher than # 2508.
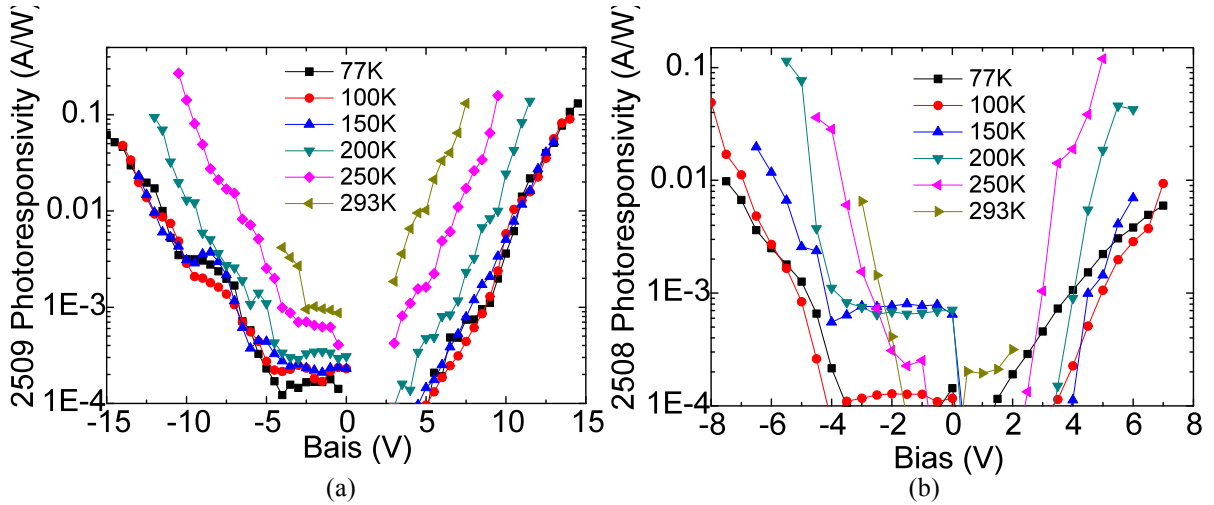
Figure. 3.19. (a)Temperature-dependent photoresponsivity of #2509 at different bias. (b)Temperature-dependent photoresponsivity of #2508 at different bias.

3.5.5 Photoconductive Gain

Fig. 3.20 (a) and (b) shows the photoconductive gain of #2509 and #2508 as function of bias for different temperatures. From equation (5) the capture probability of QDIP is small as 1×10^{-4} to 1×10^{-3}, and the gain can reach to 1000. Both of them show the longer carrier lifetime of this QDIP, and it verifies the capping techniques improves it. Since the capture probability is much less than 1 in these devices, as a good approximation, the photocurrent gain and the noise gain are equal in this device.

Fig. 3.21 shows the normalized photoresponsivity R_i/Gph for different temperature. A near constant R_i/Gph is observed at the high bias range at different temperatures. This indicates that the strong temperature-dependent potoresponsivity effect is mainly due to the electron thermal reemission-induced temperature-dependent photoconductive gain.
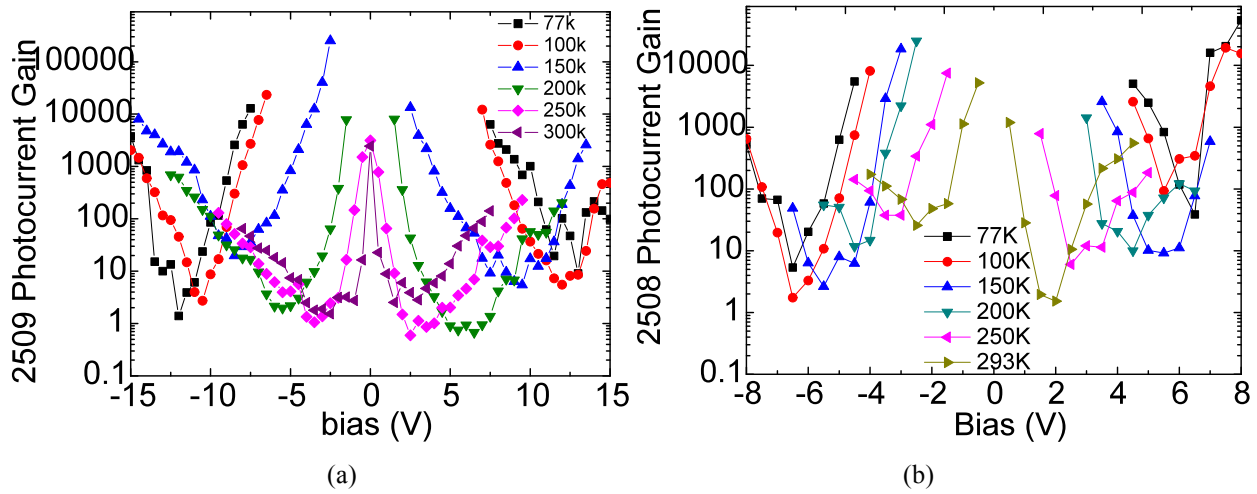
Fig. 3.20. (a)Temperature-dependent photocurrent gain of #2509 at different bias. (b)Temperature-dependent photocurrent gain of #2508 at different bias.
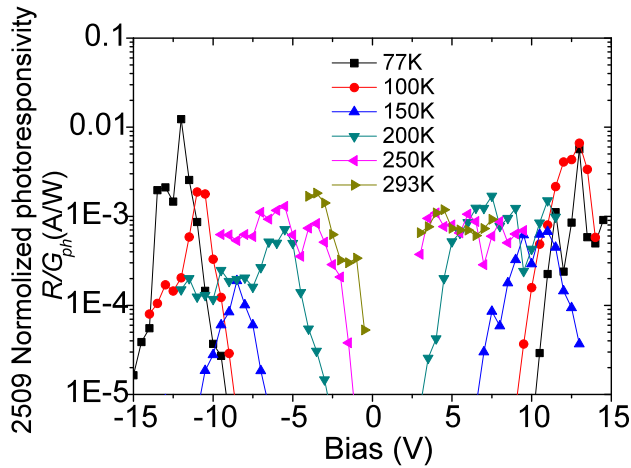
Fig. 3.21. #2509 Normalized photoresponsivites R/G_n at 77, 100, 150, 200, 250 and 293K.

3.5.6 Detectivity

Fig. 3.22 (a) and (b) show the detectivity for different temperatures. The highest detectivity value is 9.8×10^8 cmHz$^{1/2}$/W at 12V and 77K for #2509. The detectivity value decreases with increasing temperatures due to the noise current increasing with the temperature.
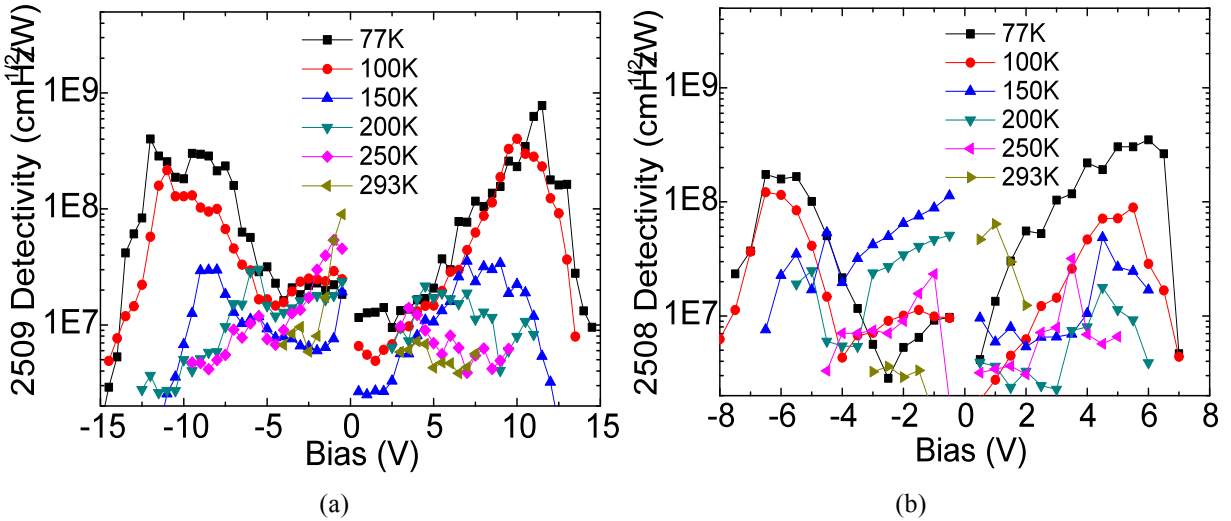
Figure 3.22. (a) photodetectivites of #2509 at 77, 100, 150, 200, 250 and 293K.
(b) photodetectivites of #2508 at 77, 100, 150, 200, 250 and 293K.

3.6 Conclusion

In recent 10 years, several research groups [12]-[16] have reported the QDIPs with the operating temperature between 80K-200K. The medium level of the operating temperature range may be caused by the flattened shape QDs with interface diffusion between dot and capping material and weak 0D quantum confinement.

In this chapter, we have demonstrated a mid-infrared engineered QDs DWELL detector with high operating temperature as 250 Kelvin. This improvement is achieved by exploring various capping material combinations and growth condition, the shape engineered QD detector was increased dot height to base ratio of 0.67 compared to a conventional QD detector with a ratio of 0.23. The change in the aspect ratio was monitored using TEM. A significant increasing in the *s/p* polarization ratio was measured using the polarization dependent spectral photoresponse. We believe that the use of an $In_{.15}Al_{.1}Ga_{.75}As$ cap prevents the flattening of QDs by reducing the diffusion gradient. This is expected to increase the carrier relaxation time by providing 3D quantum mechanical confinement.

The infrared photodetector shows the highest operating temperature is increased to 250K, the peak photodetectivity of 1×10^9 cmHz$^{1/2}$/W at 77K for a peak wavelength of 4.8

μm, and 7.2×10^7 cmHz$^{1/2}$/W at 250K for a peak wavelength of 3.2 μm, which demonstrated their tunability over a wide bias range. The dark current density is as low as 6.3×10^{-7}A/cm^2 (V$_b$=7V) and 2×10^{-4}A/cm^2 (V$_b$=12V) at 77 K, and the photocurrent gain is 100 (V$_b$=12V) at 77 K. The improvement in an engineered QD's quantum confinement decreases dark current in a detector, increases the carrier lifetime, thereby increasing the overall temperature of operation. This progress due to quantum engineering techniques brings us a step closer to realizing 300K high performance detectors.

CHAPTER 4 SUB-MONOLAYER QUANTUM DOTS FOR INFRARED PHOTODETECTOR

4.1 Introduction

We report the optimized growth of the InAs/InGaAs Sub-Monolayer (SML) Quantum Dot Infrared Photodetector (QDIP) with the small dot base diameter as 6 nm by MBE. In the previous chapter, we reported on the optimized dot geometry and quantum confinement of SK-QDIP using $In_{.1}Al_{.15}Ga_{.75}As$ capping material. The results indicate that the engineered SK QDs with small base diameter (12 nm) and large height (8 nm) have better 3-D quantum confinement, behavior more closely resemble the "artificial atom", and have improved high operating temperature reach to 250 Kelvin. But due to the SK QD epitaxy growth technology, the dot base diameter is always larger than the dot height, therefore the in-plane quantum confinement is always weaker than the vertical quantum confinement. Thus in normal incidence QDIP imagers without gratings, a large part of the signal is not utilized.

Recently, several groups have reported growth of InAs/InGaAs SML QDs on GaAs without wetting layer [1]-[3]. Compared to "dome-shaped" SK QDs, the "cylinder-shaped" SML QDs has advantages including small base diameter, better 3-D quantum confinement, high dot density, adjustable height of the dot geometry, tailorable aspect ratio, and the absence of the wetting layer.

In the first design, the InAs/InGaAs SML QDs were formed using 2 layers of 0.5 ML InAs evenly embedded in 5.1 nm GaAs quantum well. The growth temperature has the effect to the Indium interface diffusion, dot geometry, 3D quantum confinement, strain model in whole system. From the PL spectra results, the ground state of SML-QD is energetically close to the GaAs:Si energy, the dot grown at 640 °C has the strongest PL intensity. By examining the dot geometry using TEM, the SML-QD grown at 480 °C has the small base diameter as 6 nm, while that grown at 540 °C has the large base diameter as 30 nm. The XRD RADS simulation shows the structural property of this sample is more like a QWIP. The results of the s/p polarized spectral response ratio and the dot geometry height to base aspect ratio are corroborated each other. The SML-QD detector grown at 480 °C has the smallest base diameter of 6 nm, and has the highest s/p ratio as

9% in this study. The SML-QD detector grown at 540 °C has the large base diameter as 30 nm, and has the low s/p ratio less than 1%. At 77K, #2916 (grown at 540 °C) was observed with the highest responsivity of 0.40 A/W, and the highest detectivity of 5×10^8 cmHz$^{1/2}$/W 0.40 at 0.25 V for a peak wavelength of 10.3 μm. This results are due to the GaAs Quantum Well (QW) requires the high growth temperature for the high crystal quality, low defect density, and improved optical absorption, even the dot has large base diameter, heavy interface diffusion between dot and the surrounding QW material.

Next, we consider the SML-QD with small base diameter, low interface diffusion under medium growth temperature for high crystal quality.

4.2 InAs/GaAs SML-QD

4.2.1 Molecular Beam Epitaxy growth

In this chapter, we designed and grew InAs/InGaAs SML QDs infrared photodetector on (100) S. I. GaAs substrate using a VG-80 solid-source MBE system with a cracked As$_2$ source. The diagram of the growth structure is shown in Figure 4.1. In the figure 4.1(a), the InAs/InGaAs SML QDs were formed using 2 layers of 0.5 ML InAs evenly embedded in 5.1 nm GaAs quantum well. The QW are doped to 5×10^{17}cm^{-3}, *n*-type. While in the figure 4.1(b), the InAs/InGaAs SML QDs were formed using 10 layers of 0.5 ML InAs evenly embedded in 5.1 nm GaAs quantum well. The active region consists of 10 periods of SML QDs separated by 50 nm Al$_{.16}$Ga$_{.84}$As barrier is sandwiched by 1000 nm bottom and 200 nm top N+ GaAs contact layer.

4.2.1.1 Optimization of the Growth Temperature

The growth conditions were optimized in several factors such as the Beam Equivalent Pressure (BEP) III/V flux rate ratio, growth temperature, growth rate, and interruption both before and after InAs deposition. At the first step, the growth condition of the SML QDs with the V/III flux rate ratio as 30, growth temperature as 540°C, growth rate as InAs- 0.159 ML/s and GaAs- 0.787 ML/s, and 10 sec interruption both before and after InAs deposition have been selected. The optimized DWELL heterostructure and growth condition used in the SML QDs study are shown in Table 4.1.
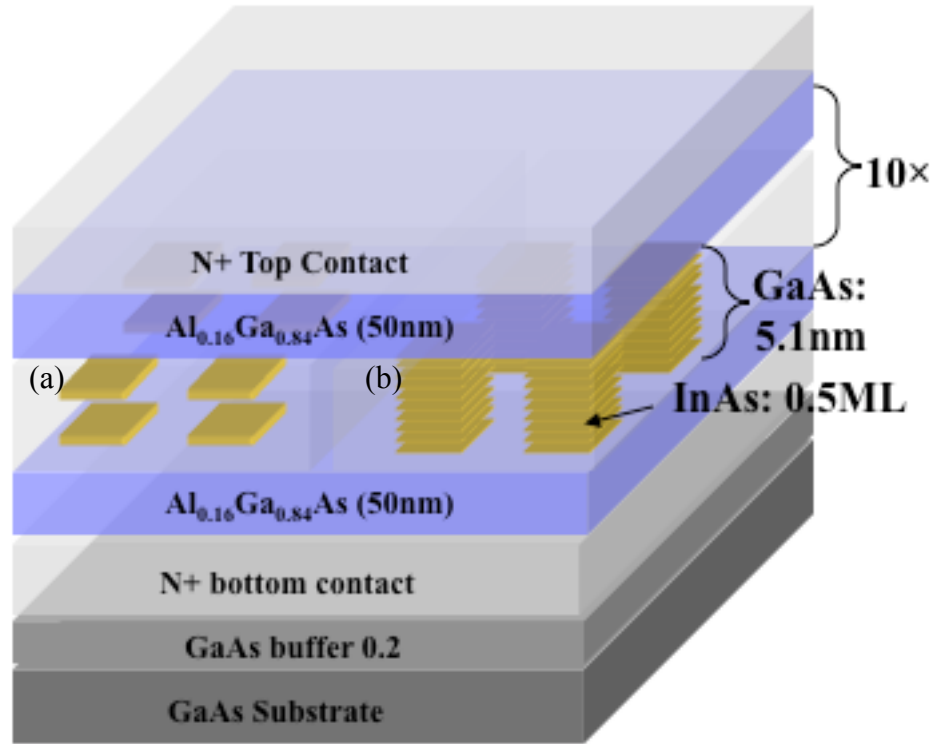
Figure 4.1 The hetorostructure schematic of the SML QDs QDIP (a) the InAs/InGaAs SML QDs were formed using 2 layers of 0.5 ML InAs evenly embedded in 5.1 nm GaAs. (b) the InAs/InGaAs SML QDs were formed using 10 layers of 0.5 ML InAs evenly embedded in 5.1 nm GaAs.

Table 4.1. The growth condition and materials used in the SML QDs study.

SML Quantum Dot	Run#	T (°C)
2 layers of InAs in 5.1 nm GaAs	2912	460
	2903	480
	2911	480
	2910	500
	2909	520
	2916	540
10 layers of InAs in 5.1 nm GaAs	2903	480

4.2.2 Optical Characterization of SML-QDs

4.2.2.1 Photoluminescence

The overall effect of the various growth condition employed on the quality of the SML QDs can be determined by PL measurement. The PL measurement was undertaken using a He-Ne pump laser and an InGaAs detector, which has a response range from 800-1700nm at the room temperature.

Since the GaAs quantum well in the SML QD study is doped as 5×10^{17}cm^{-3}, n-type, and the InAs is deposited as intrinsic materials, we grow two reference samples to observe the Si doping effect to the PL peak wavelength. #2854 has the same heterostructure with the SML study samples, but the GaAs quantum well is doped as 2×10^{17}cm^{-3}, n-type, without InAs deposition. Thus, the # 2854 is a GaAs:Si/Al$_{.16}$GaAs supperlattice structure. Another reference sample has no Si doping at all, it as a simple GaAs/Al$_{0.8}$GaAs supperlattice structure.

The result of the PL measurement shows: almost every sample with the SML QDs containing 2 layers of 0.5 ML InAs show the PL spectra, but no sample with SML QDs containing 10 layers of 0.5 ML InAs has any PL spectra. Thus, the consequent study is focused on the former design.

Figure 4.2 (a), (b) and (c) show the normalized PL from 10 Kelvin to 300 Kelvin for sample 2903, 2916 and 2854. For SML-QDIP sample 2916, even at 300K, the PL spectra show strong emission with two dominant peaks: a GaAs band edge peak at ~ 1.42 eV and SML-QD peak at ~1.46 eV. By comparing the PL from the SML-QDIP sample and the n+-doped GaAs sample, the three peaks at 10K (in Figure 4.2 (d)) are attributed to (a) a Si$_{Ga}$+Si$_{As}$ peak at ~1.489eV, (b) Si$_{Ga}$, e-h peak ranging from 1.513 to 1.531 eV, and (c) a SML-QD peak at ~1.553 eV. In this device, the peak energy of SML-QD is higher than GaAs band edge due to strain and quantum confinement in SML-QDs. Additional experiments that fully take into account the peak energy of SML-QDs are needed to confirm this effect with XRD and TEM.

Figure 4.3 shows the normalized PL at 10 Kelvin for SML-QDIP study samples with different growth temperature and two supperlattice reference samples. For the growth temperature between 460 °C to 520 °C, the SML-QD peak wavelength is almost same as the Si:Ga e, h peak wavelength, but the former is 0D confinement and the latter

is 2D confinement. When the growth temperature increased to 540°C, the PL spectra shows the strong SML-QD peak, which is higher than the Si doped GaAs band edge. The GaAs/AlGaAs supperlattice sample shows the GaAs band edge at ~1.48 eV and the AlGaAs QW without SML-QD at 1.6 eV.
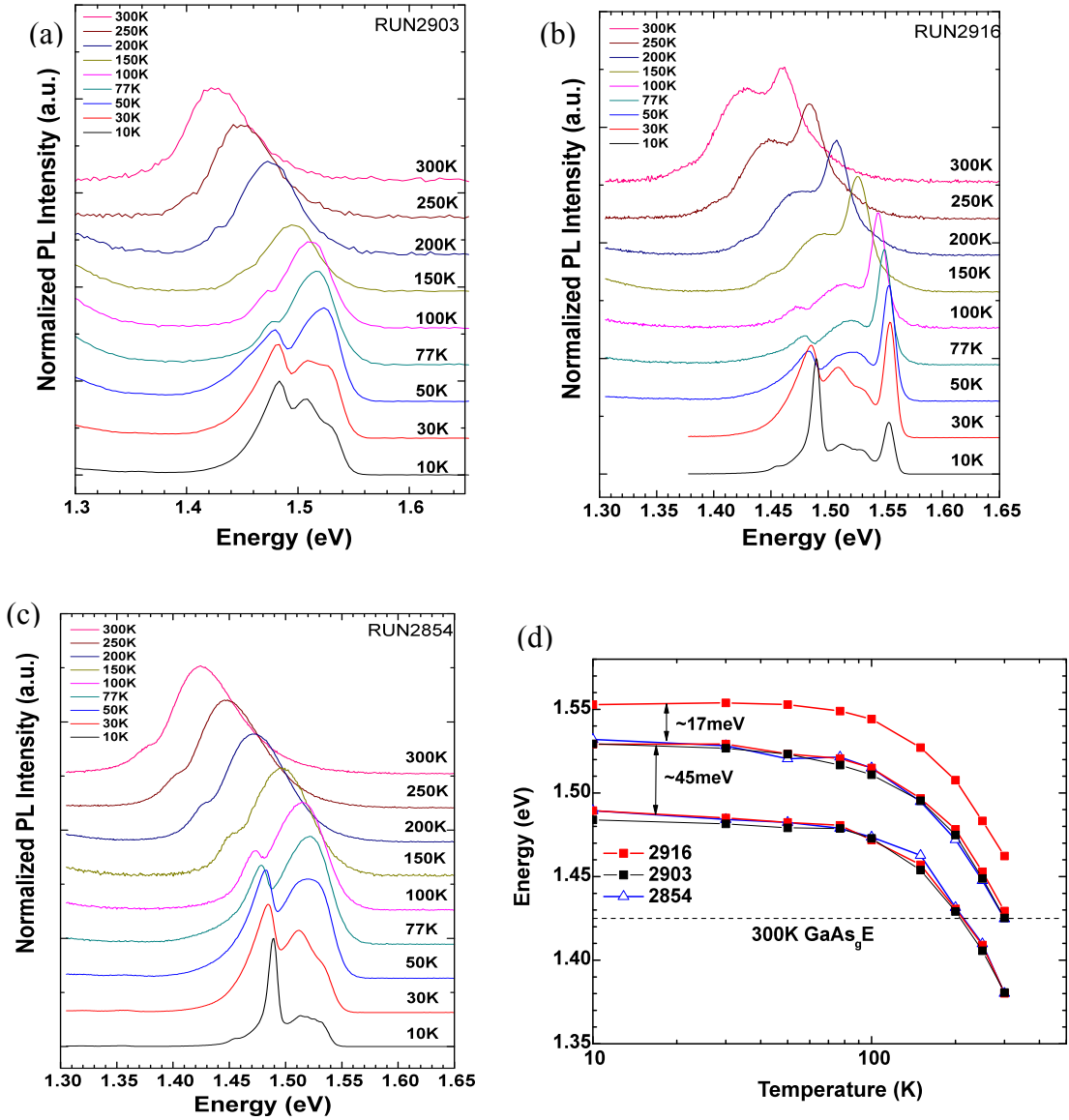
Figure 4.2 The normalized PL from 10 Kelvin to 300 Kelvin for sample (a) 2903, (b) 2916 and (c) 2854. (d) The peak wavelength of three peaks at different temperature.
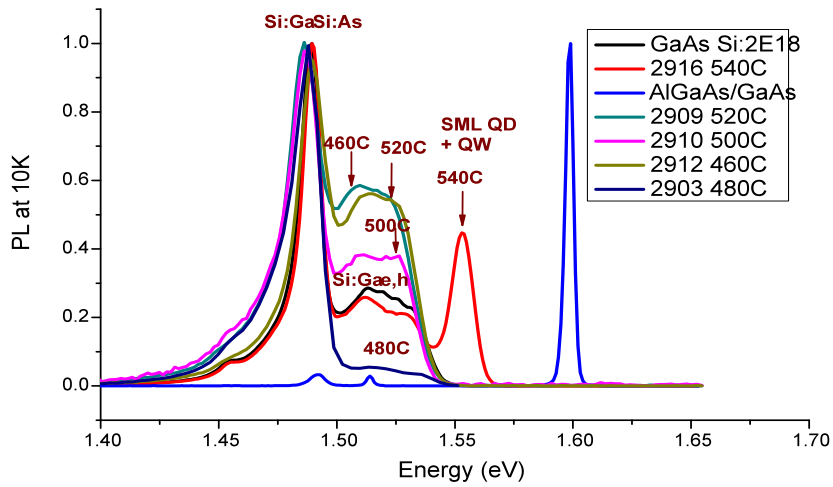
Figure 4.3 The normalized PL at 10 Kelvin for SML-QDIP study samples with different growth temperature and two supperlattice reference samples.

Figure 4.4 shows the conduction band diagram for SML-QDIP study samples with different growth temperature and two superlattice reference samples. In the SML-QD detector, the interband excitation is between the SML-QD ground state energy level

to the QW continuum energy level $Al_{.16}GaAs$ ~1.622 eV. Since the SML-QD ground state energy level with different growth temperature are really close to each other, the detectors have the closed detection peak wavelength around 10.5 μm.

4.2.3 Structural Characterization of SML-QDs

4.2.3.1 TEM

The diagram of the growth structure and the low resolution standard model TEM image are shown as Fig. 4.5 (a) and (b). The InAs/InGaAs SML QDs were formed using 2 layers of 0.5 ML InAs evenly embedded in 5.1 nm GaAs. The active region consisted of 10 periods of SML QDs separated by 50 nm $Al_{.16}Ga_{.84}As$ barrier and is sandwiched by 500 nm bottom and 200 nm top N+ GaAs contact layers. The TEM image shows the epitaxial growth is accurate as the design.
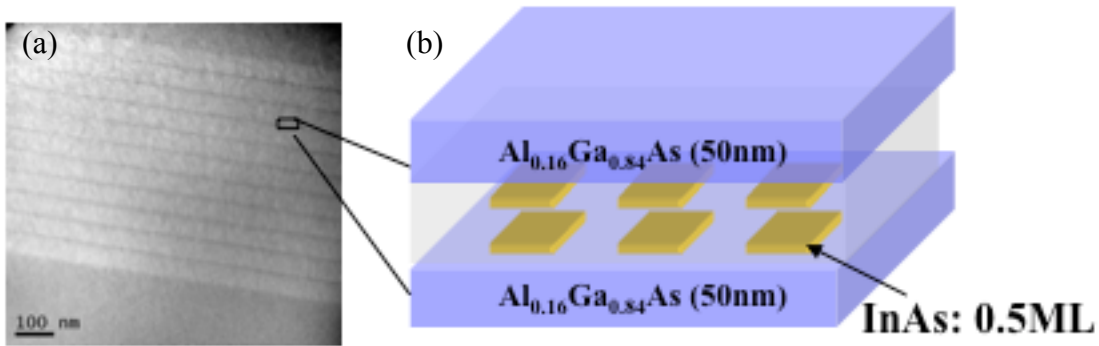
Figure 4.5: (a) The TEM image of the growth structure (b) The heterostructure schematic of SML-QD in GaAs QW with AlGaAs barrier

4.2.3.2 Scanning TEM

High resolution Scanning TEM (STEM) image can get the chemical distribution information of the specimens. More heavier of the chemical atomic mass, more brighter of the image area. Since the SML-QD has small dot base diameter and none-uniform strain model, STEM image is a priority approach to observe the dot geometry and interface diffusion. Figure 4.6 (a) and (c) are the black white and color STEM images of the sample #2903 (grown at 480 °C), and figure (b) and (d) are the black white and color STEM images of the sample #2916 (grown at 540 °C).
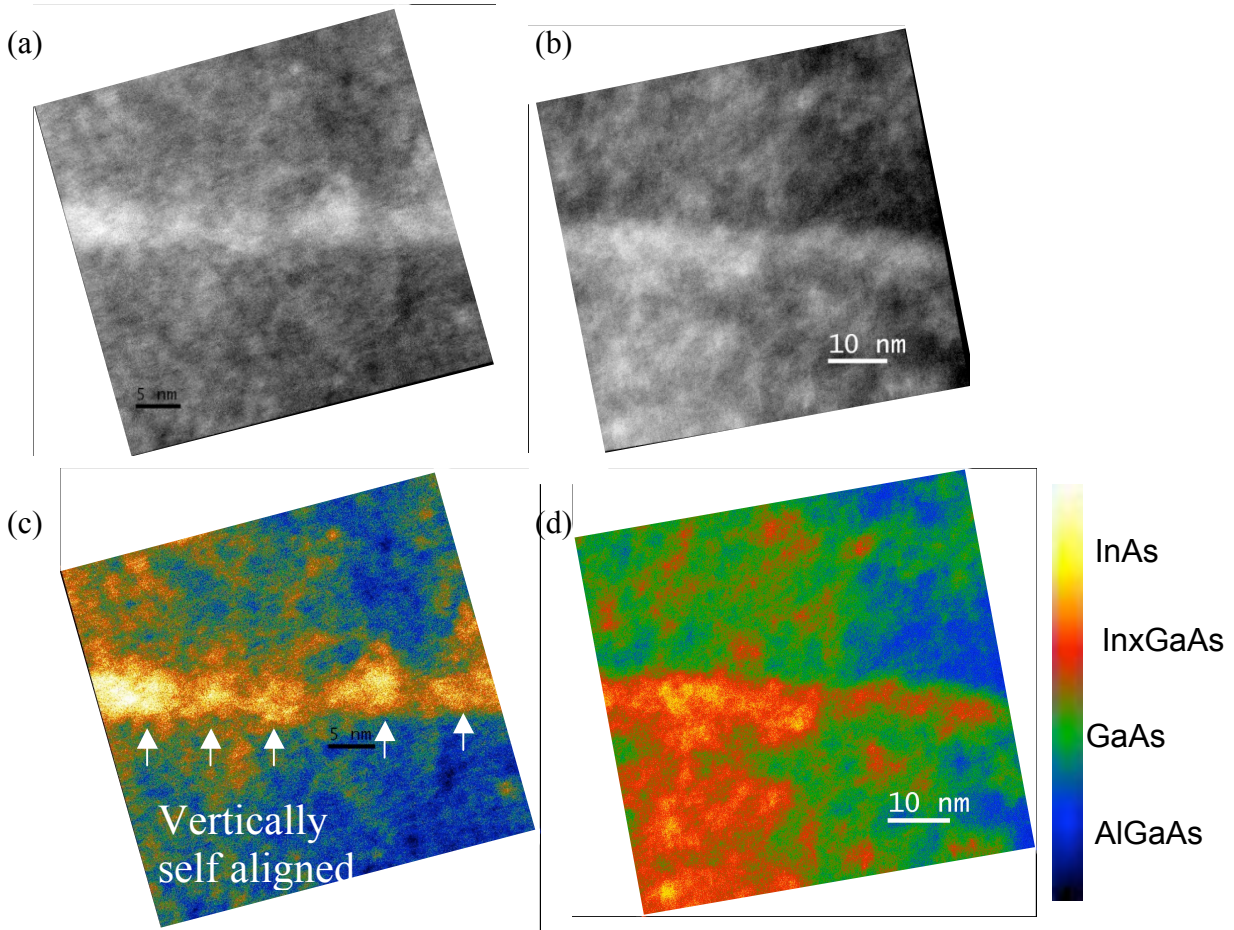
Figure 4.6 (a) and (c) are the black white and color STEM images of the sample #2903 (grown at 480 °C), (b) and (d) are the black white and color STEM images of the sample #2916 (grown at 540 °C).

Color high resolution STEM image of the SML QDs grown at 480 °C (#2903) in Fig. 4.6 (c) reveals that the two layers of InAs/InGaAs SML QDs is confined evenly in the 5.1 nm GaAs and they are vertically self-aligned to each other. The dots have InAs core surrounded by $In_xGa_{1-x}As$ alloy with 7-8 nm base diameter and total 5-6 nm height. There is no wetting layer observed.

Color high resolution STEM image of the SML QDs grown at 540 °C (#2916) in Fig. 4.6 (b) reveals that the Indium is significantly diffused. The dots have small InAs core surrounded by large amount of In_xGaAs alloy with low Indium composition. The

InAs/InGaAs SML- QD has large base diameter as 25-30 nm and height as 5-6 nm. There is no wetting layer observed. So the in-plane quantum confinement of the SML QD grown at 540 °C is weaker than that grown at 480 °C.

For the SML-QD structure designed as figure 4.1(b), the InAs/InGaAs SML QDs were formed as 10 layers of 0.5 ML InAs evenly embedded in 5.1 nm GaAs quantum well. No PL spectra was observed, we still made a STEM image to analyze the dot geometry and interface diffusion. The SML-QD diagram of this growth structure and the color STEM image are shown as Fig. 4.7 (a) and (b). It reveals that the 10 layers of InAs/InGaAs SML QDs are confined evenly in the 5.1 nm GaAs and they are vertically self-aligned to each other with a tilted angle along the [111] direction. The dots have pure InAs core surrounded by thin $In_xGa_{1-x}As$ alloy with high Indium composition. The dot has 3 nm base diameter and total 7 nm height. There is no wetting layer observed. Even the dot has small base diameter and less Indium interface diffusion, however, the large amount of Indium cause the high strain and high defect density in this whole system, and lead to the bad optical property of the intersubband transition.
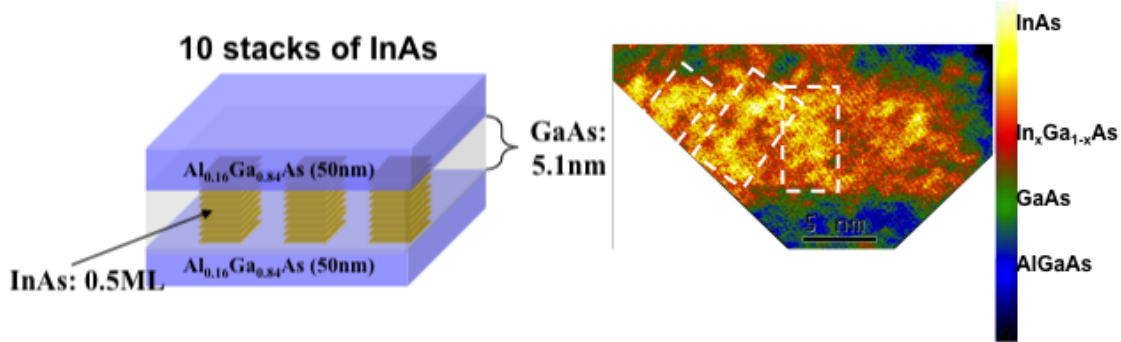
Figure 4.7 (a) The heterostructure schematic of SML-QD formed using 10 layers of 0.5 ML InAs evenly embedded in 5.1 nm GaAs quantum well, (b) the color STEM image

4.2.3.3 XRD

Figure 4.8 shows the XRD rocking curve of the SML-QD sample 2916 which is grown at 540 °C (black color) and Rocking curve Analysis by Dynamic Simulation (RADS) Mercury simulation (red color). RADS Mercury may be used to fit the following

parameters such as layer thickness, composition, and strain. The designed parameters and the best-fit parameters of the RADS Mercury simulation are shown at Table 4.2.
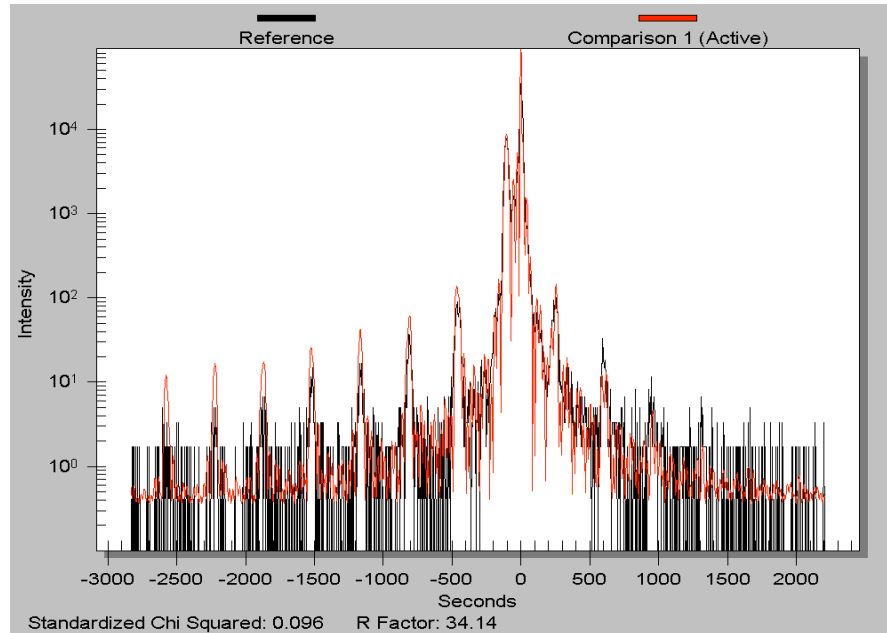
Figure 4.8 The XRD rocking curve of the SML-QD sample #2916 which is grown at 540 °C (black color) and Rocking curve Analysis by Dynamic Simulation (RADS) Mercury simulation (red color).

Table 4.2 The designed parameters and the best-fit parameters of the RADS Mercury simulation for SML-QD sample #2916 (grown at 540 °C)

Repeat	Material	Design		Simulation		
		Thickness (nm)	x	Thickness (nm)	x	
	GaAs	200		200		
10	Al(x)Ga(1-x)As	50	16%	49.4	14.29%	
10	GaAs	2.6		0.27		Indium significantly diffused
10	In(x)Ga(1-x)As	0.3	100%	3.05	5%	
10	GaAs	2.6		0.8		
	Al(x)Ga(1-x)As	50	16%	49.4	14.29%	
	GaAs	1000		1000		
	GaAs substrate					

From the best-fit parameters in Table 4.2, the Indium is significantly diffused when the growth temperature reaches to 540 °C. Since the dot has large base diameter, the structural property is similar to an $In_{.05}GaAs/Al_{.1429}GaAs$ quantum well infrared photodetetor.

4.2.4 Electro-optic Characterization of SML-QD Infrared Detectors

4.2.4.1 Spectral Response

The SML-QD QDIP detectors with various growth temperature have the maximum spectral response peak wavelength from 10.3 to 10.9 μm working at the optimum bias as shown in Fig. 4.9. The inset of Figure 4.9 shows the maximum peak wavelength is slightly increased with the increasing of the growth temperature. The energy difference between the ground state level and the first excited level are ~ 128 meV. But over all, the SML-QD ground state energy level is energetically closed to the GaAs:Si energy level, the dot geometry and Indium diffusion just has slightly effect to the peak wavelength.
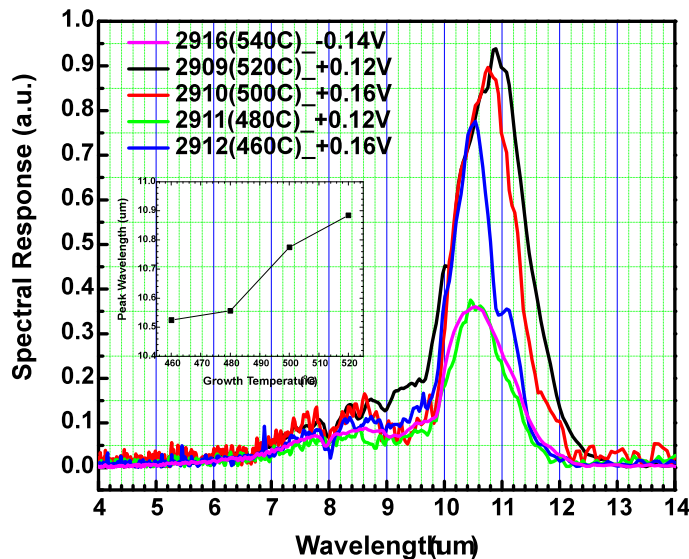
Figure 4.9 The maximum spectral response peak wavelength of SML-QD QDIP detectors with various growth temperature working at the maximum bias.

4.2.4.2 Polarized Spectral Response

For polarization dependent infrared spectral photoresponse measurements, the experimental setup schematic is shown as Figure. 2.11. The processed devices were polished with 45° side facet geometry, mounted on the 45° facet holder, wire-bonded on the pins of the leadless chip carrier (LCC), loaded in the cryostat with KBr window, and cooled to 77 Kelvin using liquid N_2. After the infrared radiation from Fourier Transform Infrared Spectroscopy (FTIR Nicolet 6700) is transmitted through the polarizer, it is vertically incident upon the 45° side facet of the substrate and device, and follows the zigzag ray path in it. The 428 Current Amplifier is connected with the cryostat to add bias on the device and give output signal beck to FTIR and OMNIC software to measure the spectral photoresponse.
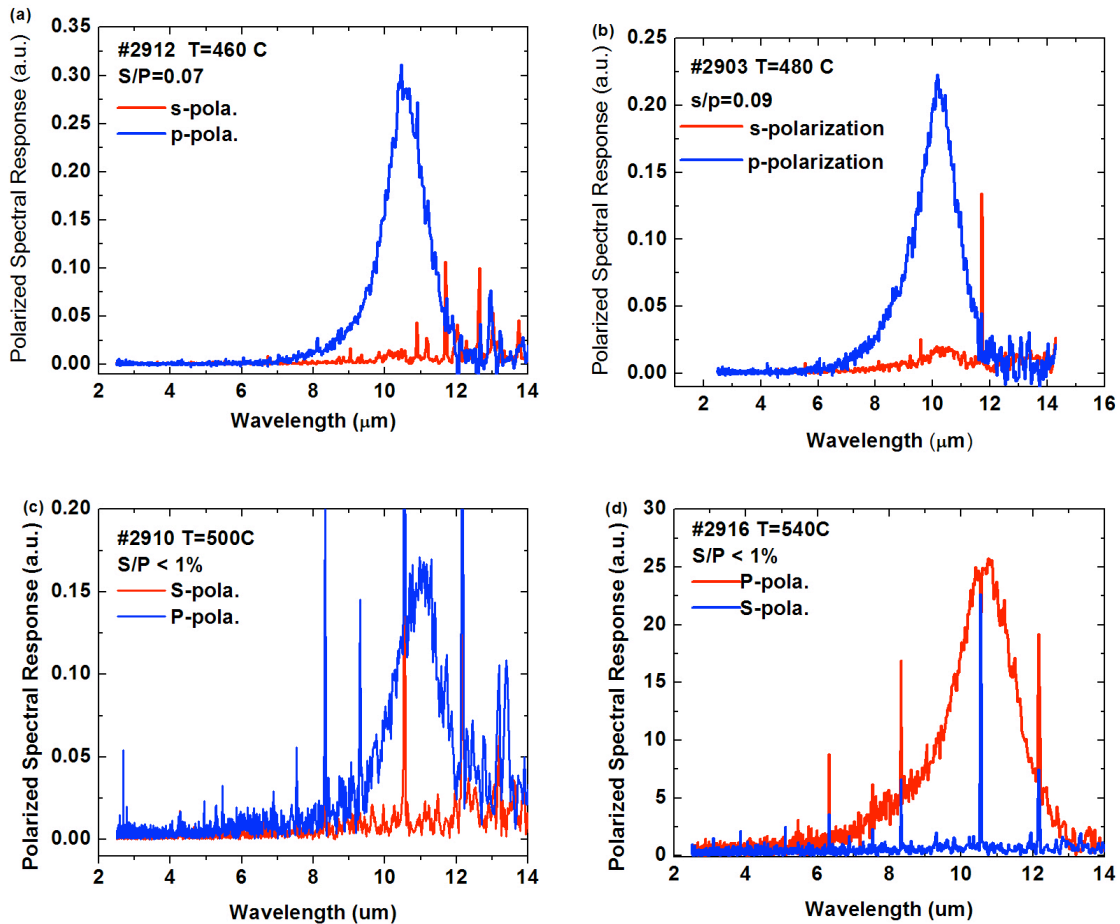
Figure 4.10 (a) (b) (c) and (d) show that the s and p polarized spectral response of SML-QDs sample grown at 460, 480, 500 and 540 °C.

94

The results measured at 77 Kelvin in Fig. 4.10 (a) (b) (c) and (d) show that the s and p polarized spectral response of SML-QDs sample grown at 460, 480, 500 and 540 °C. The s-to-p ratio is listed at table 4.3.

Decreasing of the dot base width, the in-plane (TE) quantum confinement and in-plane infrared absorption are dramatically improved compared to the vertical direction (TM). And the dot density is also increased. A strong spectral response not only describes the high material quality of QDs, such as low defect and low trap center, but also the improved discrete quantum confinement, and less intermixing and leakage path of the interface between QDs and surrounding QW materials.

From the data listed at table 4.3, the results of the s/p polarizated spectral response ratio and the dot geometry height to base aspect ratio are corroborated each other. The SML-QD detector grown at 480 °C has the small base diameter as 6 nm, and has the highest s/p ratio as 9% in this study. When the s/p ratio is closer to 1, the behavior of SML QDs do closely resemble to the 3-D "engineered atoms". For conventional Stranski-Krastanov QDs, the *s* polarized quantum confinement is always less then the *p* polarized since the base width is always larger than the height [16]. However, it is possible to obtain a SML-QD with the s/p ratio larger than 1 under future optimization.

Table 4.3 The growth condition and measurement results in the SML QDs study.

SML Quantum Dot	Run#	T (°C)	TEM height/base	s-to-p ratio	R_i (A/W)	D $(cmHz^{1/2}/W)$
2 layers of InAs in 5.1 nm GaAs	2912	460		5%	0.10	2×10^8
	2903	480	6nm/8nm	9%		
	2911	480			0.07	1×10^8
	2910	500		<1%	0.11	1.05×10^8
	2909	520			0.12	3×10^8
	2916	540	6nm/30nm	<1%	0.40	5×10^8
10 layers of InAs in 5.1 nm GaAs	2903	480	8nm/3nm	No signal		

4.2.4.3 Responsivity and Detectivity

Figure. 4.11 shows the peak photoresponsivity R_i at 77 K as function of bias for SML-QD detector with different growth temperatures. The maximum R_i for each sample are listed at table 4.3. At 77K, the highest R_i of 0.40 A/W was observed at 0.25 V for #2916 (grown at 540 °C). The high growth temperature involves the high crystal quality, low defect density, and improved optical absorption, even the dot has large base diameter, significant interface diffusion between dot and the surrounding QW material. So our nexy approach is to product the SML-QD with small base diameter, low interface diffusion under high growth temperature.
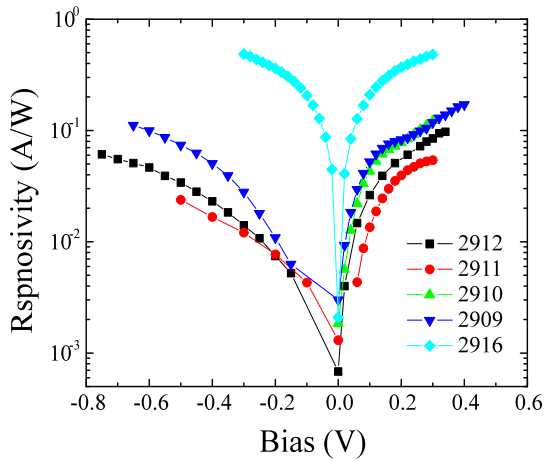
Figure 4.11: The SML QDs infrared photodetector shows the highest photoresponsivity of 0.4 A/W at 77K - 1.8V
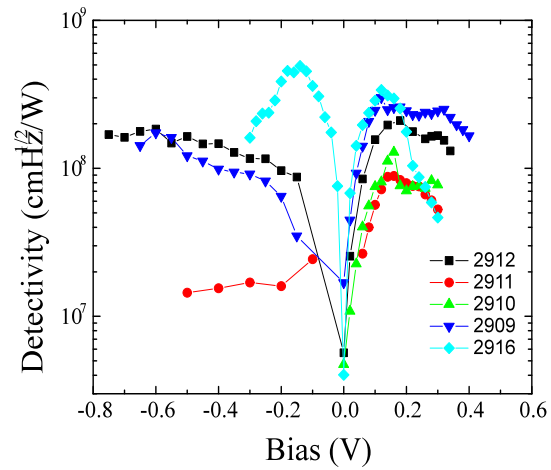
Figure 4.12: The SML QDs infrared photodetector shows the highest photodetectivity of 0.5×10^9 cmHz1/2/W at 77K -1.8V

Figure. 4.12 shows the peak Detectivity D at 77 K as function of bias for SML-QD detector with different growth temperatures. The maximum D for each sample are listed at table 4.3 too. At 77K, the highest D of 5×10^8 cmHz$^{1/2}$/W 0.40 was observed at 0.25 V for #2916 (grown at 540 °C). Thus, the SML-QD detector with the high growth temperature as 540 °C has both of the highest responsivity and detectivity in this study.

4.2.5 Conclusion

In this chapter, we demonstrate the optimized growth of the InAs/InGaAs Sub-Monalayer (SML) Quantum Dot Infrared Photodetector. Compared "dome-shaped" SK QDs, the "cylinder-shaped" SML QDs has advantages including small base diameter, better 3-D quantum confinement, high dot density, adjustable height of the dot geometry, tailorable aspect ratio, and the absence of the wetting layer.

The optical, structure and electronic-optic characterization results indicate the SML QDs with the V/III flux rate ratio as 30, growth temperature as 540°C, growth rate as InAs- 0.159 ML/s and GaAs- 0.787 ML/s, and 10 sec interruption both before and after InAs deposition have the highest performance.

The SML QD infrared photodetector shows photoresponsivity of 0.4 A/W and photodetectivity of 0.5×10^9 cmHz$^{1/2}$/W at 77K -1.8V for a peak wavelength of 10.5 μm. The dot has the small dot base diameter as 6 nm and total height as 8 nm. The ratio of the *s/p* polarized spectral response of the SML QDs QDIP at 77K is ~9%, which is comparable to the ratio of conventional SK QDs QDIP.

4.3 InAs/In$_{.1}$Ga$_{.9}$As SML-QD

4.3.1 Introduction

In previous section 4.2, we report the optimized growth of the InAs/InGaAs Sub-Monolayer (SML) Quantum Dot Infrared Photodetector (QDIP) with the small dot base diameter as 6 nm and the ratio of the *s/p* polarized spectral response is ~9% at 77K, which is as low as comparable to the ratio of conventional SK QDs QDIP. The SML-QD grow technology gave us a new approach to engineer the dot geometry and quantum confinement. But of cause, the advantage of SML-QD did not fully exploit yet. In this section, we demonstrate a new design to keep optimizing the engineered SML-QD QDIP for better quantum confinement and higher s/p polarized spectral response ratio.

In order to prevent the interface diffusion between InAs and QW, InGaAs as QW were chosen for the new design: the InAs/InGaAs SML QDs were formed using 2 layers of 0.5 ML InAs evenly embedded in 5.1 nm In$_{.1}$Ga$_{.9}$As quantum well.

4.3.2 Molecular Beam Epitaxy growth

In this section, we have designed and grown InAs/InGaAs SML QDs with InGaAs quantum well (QW) QDIPs on (100) S. I. GaAs substrate using VG-80 solid-source MBE system with a cracked As$_2$ source. The heterostructure schematic of the growth structures is shown in Figure 4.13. The InAs/In$_{.1}$Ga$_{.9}$As SML QDs were formed using 2 layers of 0.5 ML InAs evenly embedded in 5.1 nm In$_{.1}$Ga$_{.9}$As quantum well. The QW are kept as un-doped. The active region consists of 10 periods DWELL SML-QDs separated by 50 nm Al$_{.16}$Ga$_{.84}$As barrier. The number of this sample is #3002.

One reference sample (# 3001) was grown based on #3002 without SML-QD. #3001 consists of 5.1 nm un-doped In$_{.1}$Ga$_{.9}$As quantum well repeated 10 periods, which is separated by 50 nm Al$_{.16}$Ga$_{.84}$As barrier. # 3001 is a QWIP structure.

Reference sample (# 3008) was grown based on #3002 with SML-QD doped as 2×10^{17} cm^{-3}. Another reference sample (# 3007) was grown based on #3002 with un-doped SML-QD.

Since In$_x$Ga$_{1-x}$As QW requires low temperature for high crystal quality, the active region growth temperature is kept as 500 °C. The optimized SML-QD structure and growth condition used in this study are shown in Table 4.4.
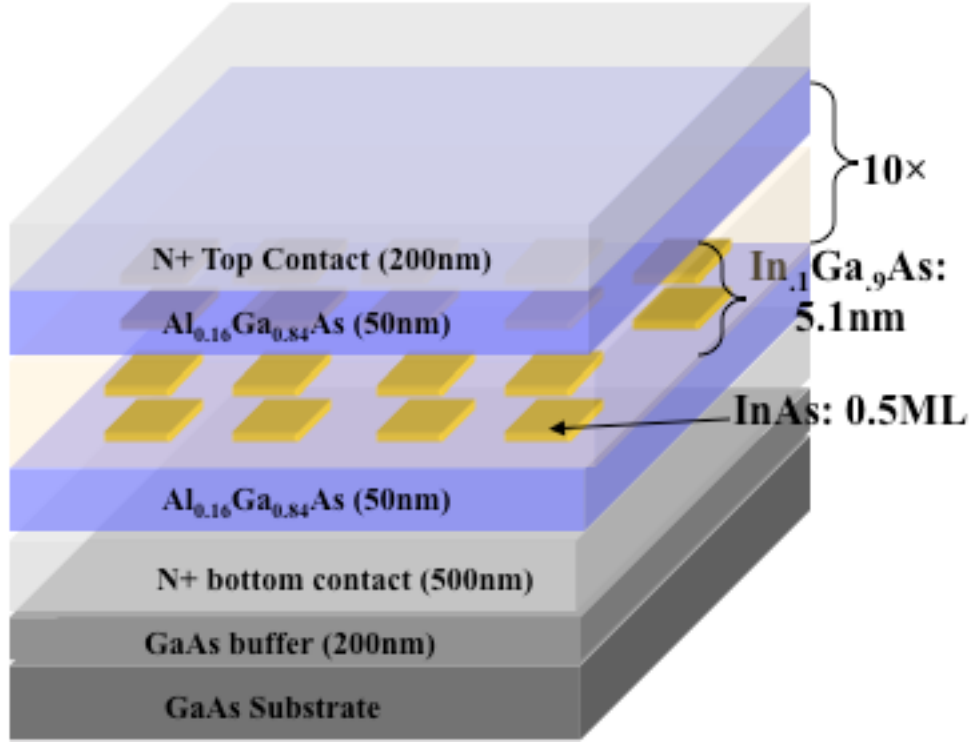
Figure 4.13: The heterostructure schematic of the new designed SML QDs QDIP: the InAs/In$_{.1}$Ga$_{.9}$As SML QDs were formed using 2 layers of 0.5 ML InAs evenly embedded in 5.1 nm In$_{.1}$Ga$_{.9}$As.

Table 4.4. The growth structure in the SML QDs study.

SML Quantum Dot	Run#		SML-QD
2 layers of 0.5 ML InAs in 5.1 nm In$_{.1}$Ga$_{.9}$As	3002	PL structure	un-doped
	3001		without QDs
	3007	Detector structure	un-doped
	3008		Doped 5×10^{17} cm^{-3}

4.3.3 Optical Characterization of SML-QDs

4.3.3.1 Photoluminescence

The overall effect of the various growth condition employed on the quality of the SML QDs can be determined by PL measurement. The PL measurement was undertaken
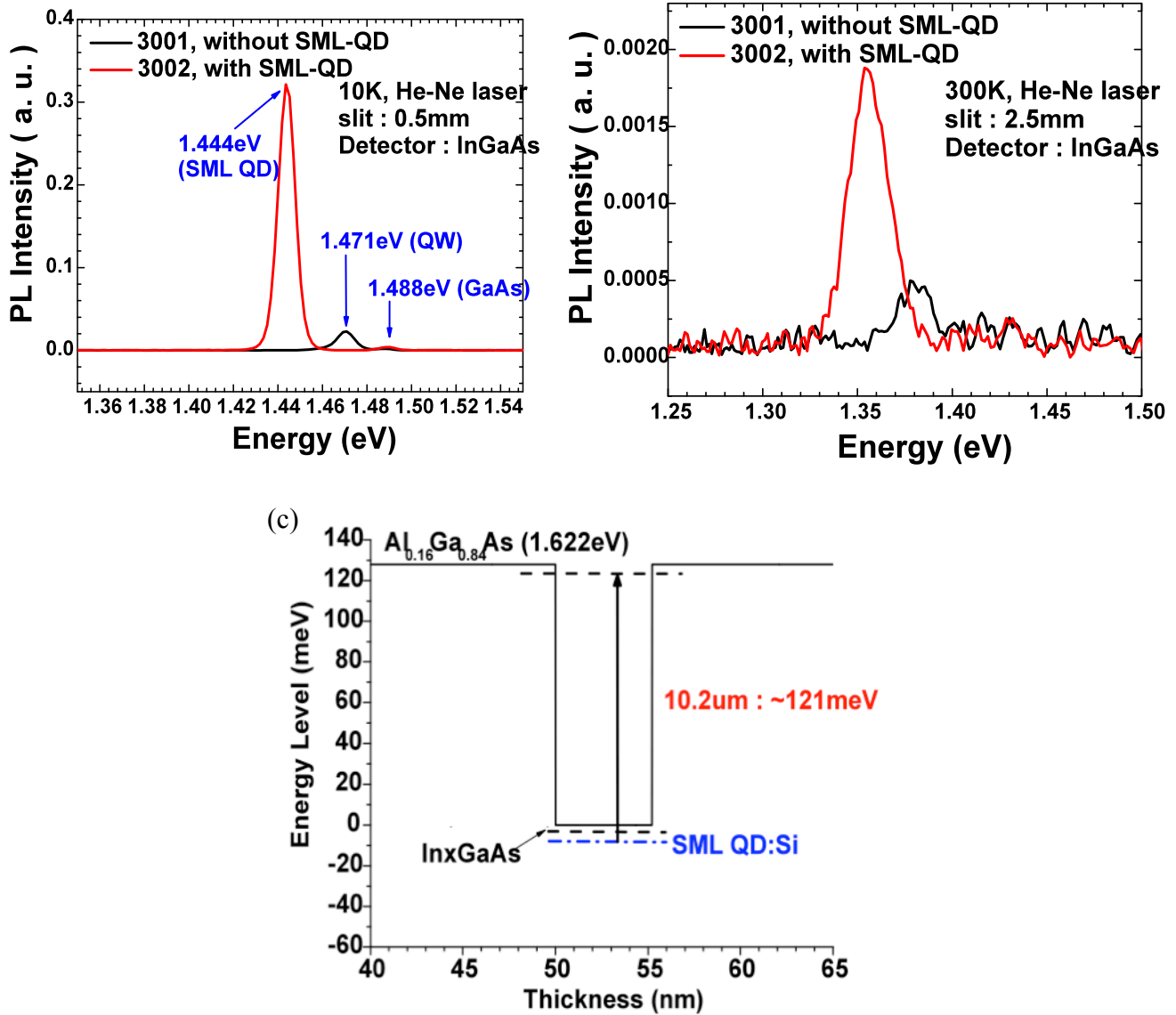
Figure 4.14: (a) and (b) show the PL at 10 Kelvin and 300 Kelvin for sample 3001 and 3002. (c) shows the conduction band diagram for SML-QDIP study samples with 5.1 nm In$_1$Ga$_9$As quantum well.

using a He-Ne pump laser and an InGaAs detector, which has a response range from 800-1700nm at the room temperature.

Figure 4.14 (a) and (b) show the PL at 10 Kelvin and 300 Kelvin for sample 3001 and 3002. For SML-QDIP sample 3002, the PL spectra shows strong QD emission peak intensity at ~ 1.36 eV at 300K, and at ~ 1.443 eV at 10K. In this device, the peak energy of SML-QD is lower than $In_{.1}Ga_{.9}As$ band edge due to the good quantum confinement in SML-QDs DWELL structure.

Figure 4.14 (c) shows the conduction band diagram for SML-QDIP study samples with 5.1 nm $In_{.1}Ga_{.9}As$ quantum well. In the SML-QD detector, the intraband excitation is between the SML-QD ground state energy level to the energy level close to $Al_{.16}GaAs$ ~1.622 eV QW continuum. After the spectral response measurement under various bias, whether the intersubband transition is bound-to-bound, or bound-to-quasi-bound, or bound-to-continuum can by verified.

4.3.4 Electro-optic Characterization of SML-QD Detectors

4.3.4.1 Spectral Response

The spectral response of 3007, 3008 and 2910 are shown in Figure 4.15 All of these samples' SML-QDs are growth at 500 °C. Both of sample 3007 and 3008 with $In_{.1}Ga_{.9}As$ QW show the narrower full width of half maximum (FWHM) than sample 2910, which is with GaAs QW. That indicates that $In_{.1}Ga_{.9}As$ QW can prevent Indium diffusion between InAs dot and wrapping QW, engineer the quantum confinement, improve the normal incidence absorption.

Figure 4.15 also shows the maximum peak wavelength of SML-QD QDIP with $In_{.1}Ga_{.9}As$ QW is slightly blue shift compared with the detector with GaAs QW. The energy difference between the ground state level and the first excited level are ~ 121 meV. The SML-QD ground state energy level is very closed to the ground state of $In_{.1}Ga_{.9}As$ QW energy level, the dot geometry and Indium diffusion just has slightly effect to the peak wavelength.
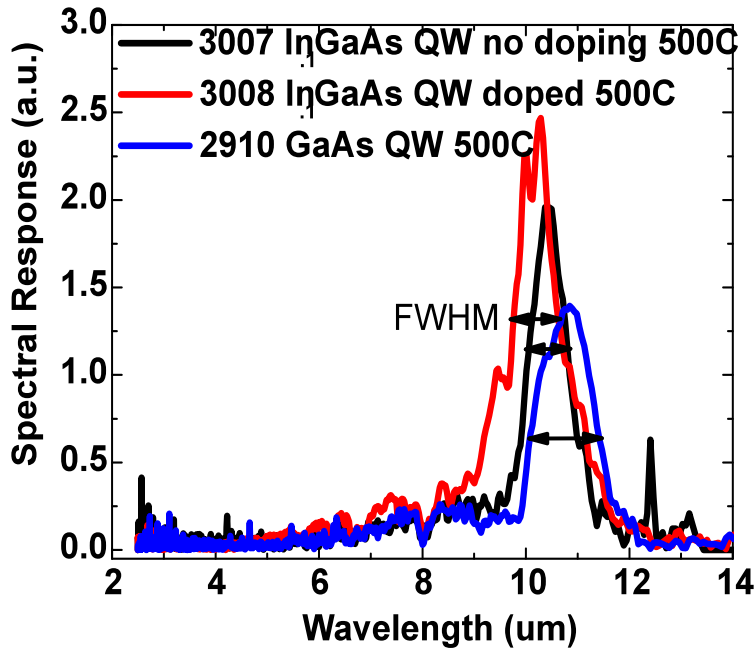
Figure 4.15: The spectral response of 3007, 3008 and 2910

Figure 4.16 (a) and (b) show the spectral response of sample 3008 (doped SML-QD with In$_{.1}$Ga$_{.9}$As QW) at 77K and 90K under various bias. The highest operating temperature of # 3008 is 90K and the peak wavelength is at LWIR region as 10.2 μm.

When bias varied, the peak wavelength does not shift at all, that indicates the intersubband transition between the SML-QD ground state and the first excited energy level is bound-to-bound intersubband transition. From the energy level simulation, the first excited energy level is very close to the Al$_{.16}$Ga$_{.84}$As continuum band edge, but the first excited energy level is still confined as a 0D discrete energy state. It demonstrates that the SML-QD growth technology significantly improves the quantum confinement, shows a great new approach to enhance the capability of QDIP detectors.
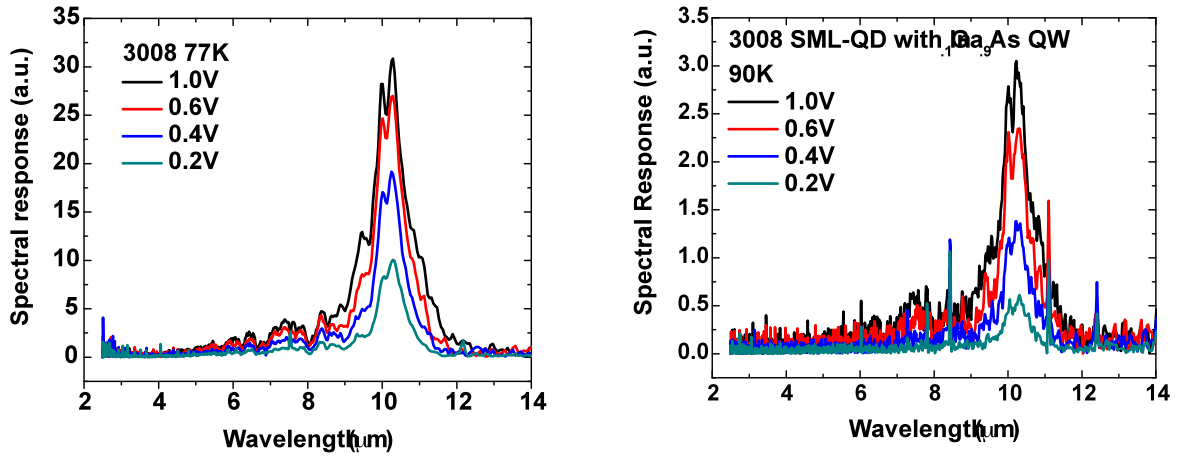
Figure 4.16: (a) and (b) show the spectral response of sample 3008 (doped SML-QD with In$_{.1}$Ga$_{.9}$As QW) at 77K and 90K under various bias.

4.3.4.2 Responsivity and Detectivity

Fig. 4.17 (a) shows the peak photoresponsivity R_i at 77 K and 90K as function of bias for SML-QD detector 3008. The highest R_i of 0.10 A/W was observed at -1.60 V at 77K, and the highest R_i of 0.10 A/W was observed at -0.5V at 90K.

Fig. 4.17 (b) shows the peak Detectivity D at 77 K and 90K as function of bias for SML-QD detector 3008. At 77K, the highest D of 6×10^7 cmHz$^{1/2}$/W was observed at 0.6 V. At 90K, the highest D of 2×10^7 cmHz$^{1/2}$/W was observed at 0.6 V.
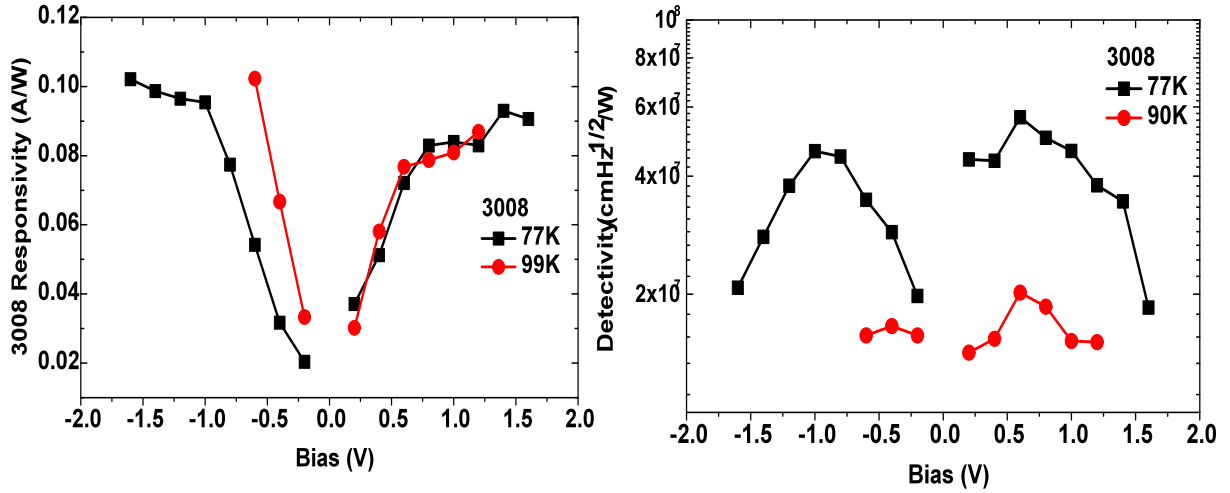
Figure 4.17 (a) shows the peak photoresponsivity R_i at 77 K and 90K as function of bias for SML-QD detector 3008. (b) shows the peak Detectivity D at 77 K and 90K as function of bias for SML-QD detector 3008

4.3.4.3 Photoconductive Gain

Figure 4.18. shows the photoconductive gain of #3008 as function of bias for 77K and 90K. From equation (2.12) the capture probability of QDIP is small as 1×10^{-4} to 1×10^{-3}, and the gain can reach to ~100. Both of them show the longer carrier lifetime of this QDIP, and it verifies the SML-QD technique improves it. Since the capture ability is much less than 1 in these devices, as a good approximation, the photoconductive gain and the noise gain are equal in this device. The photoconductive gain of ~20 was observed as 1.6V 77K, and of ~40 was observed as 1.4V 90K.
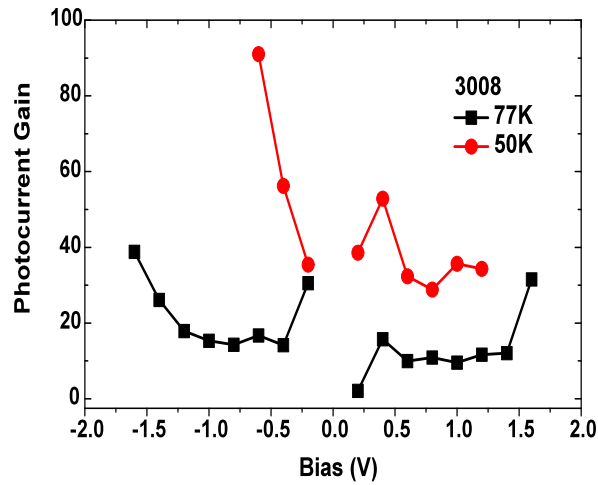
Figure 4.18 Photoconductive gain of #3008 as function of bias for 77K and 90K

4.3.5 Conclusion

In section 4.2, we have demonstrated the SML-QD with $In_{.1}Ga_{.9}As$ QW improved quantum confinement due to the $In_{.1}Ga_{.9}As$ QW significantly preventing the Indium diffusion. This QDIP shows strong bound-to-bound intersubband transition at 10.2 μm from 77K to 90K. The highest responsivity of 0.10 A/W was observed at -1.60 V at 77K, and the highest R_i of 0.10 A/W was observed at -0.5V at 90K. At 77K, the highest D of 6×10^7 cmHz$^{1/2}$/W was observed at 0.6 V. At 90K, the highest D of 2×10^7 cmHz$^{1/2}$/W was observed at 0.6 V. The photoconductive gain of ~20 was observed as 1.6V 77K, and of ~40 was observed as 1.4V 90K.

Even the 0D quantum confinement is significantly improved, the detector's performance does not reach an advantage level yet. It may cause by the un-optimized QD doping level, which may add high dark current in the IR device. Add the enhanced confinement barrier may become another approach to decrease the dark current. Of cause, all other band engineering technology discussed in chapter 1 can be involved to improve the detectoer's performance too.

In next section we demonstrate another new design: SML-QD with 4 stack of InAs layer, $In_{.15}Ga_{.85}As$ QW, and $Al_{.22}Ga_{.75}As$ & $Al_{.07}Ga_{.93}As$ double barrier.

105

4.4 InAs/In$_{.15}$Ga$_{.85}$As SML-QD

4.4.1 Introduction

In section 4.3, we have reported the optimized growth of the InAs/InGaAs Sub-Monolayer (SML) Quantum Dot with In$_{.1}$Ga$_{.9}$As QW improved quantum confinement due to the In$_{.1}$Ga$_{.9}$As QW can significantly prevent the Indium diffusion. In section 4.4, the study is focused both on engineer the SML-QD with dot geometry and quantum confinement and on engineer the quantum well band energy.

4.4.2 Molecular Beam Epitaxy growth
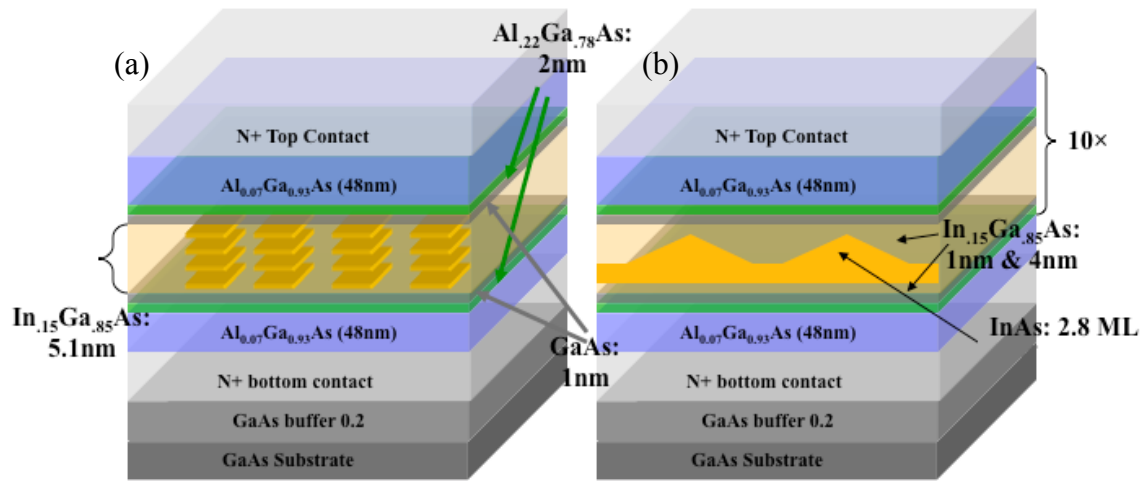
Figure 4.19: diagram of the new designed SML QDs QDIP growth structure (a) the InAs/InGaAs SML QDs were formed as 4 layers of 0.3 ML InAs evenly embedded in 5.1 nm In$_{.15}$Ga$_{.85}$As with GaAs/AlGaAs/ enhanced confinement structure (b) the InAs/InGaAs SK-QDs DWELL structure

In this section, we designed and grown InAs/In$_{.15}$Ga$_{.85}$As SML QDs with InGaAs/GaAs/AlGaAs quantum well (QW) QDIPs on (100) S. I. GaAs substrate using VG-80 solid-source MBE system with a cracked As$_2$ source. The diagram of two new growth structures are shown in Figure 4.19.

While in the Figure 4.19(a), the InAs/InGaAs SML QDs were formed using 4 layers of 0.3 ML InAs evenly embedded in 5.1 nm In$_{.15}$Ga$_{.85}$As quantum well with 1nm GaAs, 2nm Al$_{.22}$Ga$_{.78}$As QW and 48nm Al$_{.07}$Ga$_{.93}$As barrier. The active region consists of 10

periods of DWELL SML QDs separated by GaAs/Al$_{.22}$Ga$_{.78}$As/Al$_{.07}$Ga$_{.93}$As enhanced confinement structure. The active region is sandwiched by 500 nm bottom and 200 nm top N+ GaAs contact layer. The number of this sample is #3032.

In figure 4.19(b), the reference sample (#2969) were formed as 2.0 ML InAs SK-QD and wetting layer with 1 nm and 4.3 nm bottom and top In$_{.15}$Ga$_{.85}$As QW. All other parameters are same as # 3032 except it consists of 7 periods instead of 10 periods.

4.4.3 Optical Characterization

4.4.3.1 Photoluminescence

The overall effect of the various growth condition employed on the quality of the SML QDs can be determined by PL measurement. The PL measurement was undertaken using a He-Ne pump laser and an InGaAs detector, which has a response range from 800-1700nm at the room temperature.
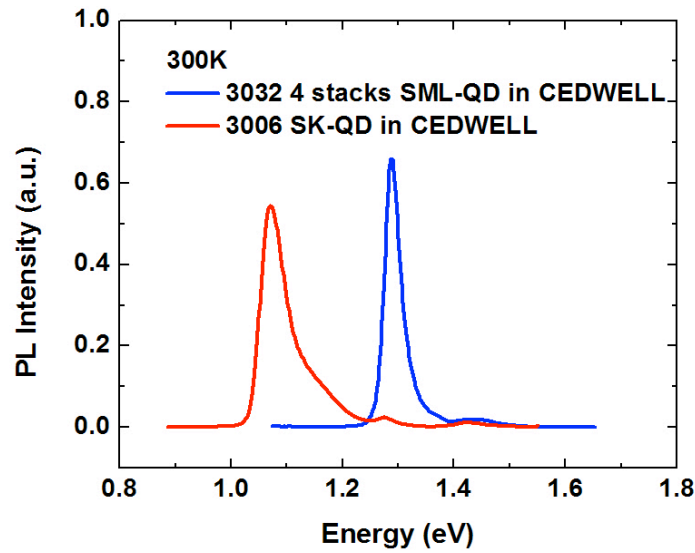
Figure 4.20: the PL for sample 3032 and 3006 at 300 Kelvin.

Figure 4.20 shows the PL for sample 3032 and 3006 at 300K. The ground stated of SML-QD is close to In$_{.15}$Ga$_{.75}$As QW, while the ground state of SK-QD is apart with the In$_{.15}$Ga$_{.75}$As QW. The FWHM of SML-QD is narrower than it of SK-QD, that

demonstrates the SML-QD with better quantum confinement and better dot size uniformity.

4.4.4 Structural Characterization of SML-QDs

4.4.4.1 TEM and STEM

The standard scanning TEM image and high resolution scanning TEM image of 3032 are shown as Fig. 4.21 (a), (b) and (c). The InAs/InGaAs SML QDs were formed as 4 layers of 0.3 ML InAs evenly embedded in 5.1 nm $In_{.15}Ga_{.85}As$. The active region consisted of 10 periods of SML QDs / $In_{.15}Ga_{.85}As$ QW separated by 1nm GaAs/2nm $Al_{.22}Ga_{.78}As$ /48 nm $Al_{.07}Ga_{.93}As$ enhanced confinement DWELL structure. The TEM image shows the epitaxial growth is accurate as the design.
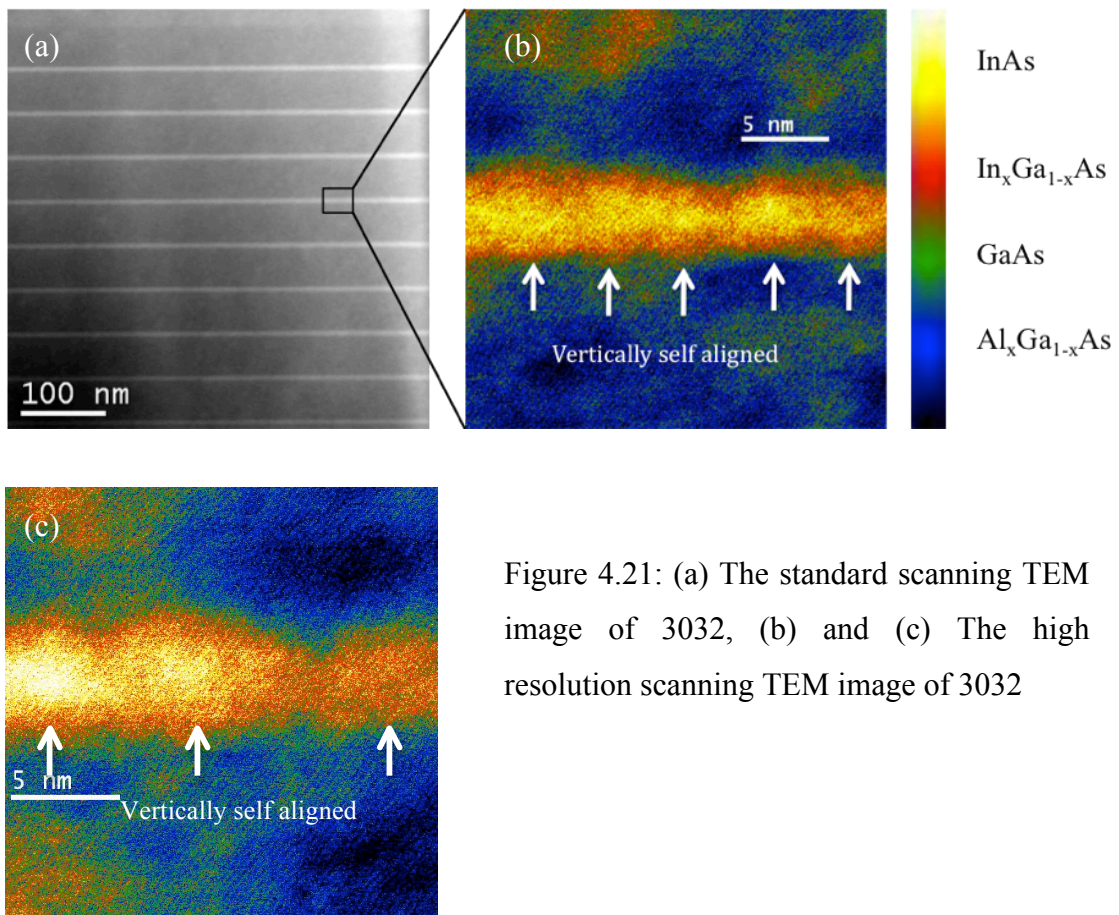
Figure 4.21: (a) The standard scanning TEM image of 3032, (b) and (c) The high resolution scanning TEM image of 3032

Figure 4.21 (b) and (c) show 4 stacks of 0.3ML InAs are vertically self aligned, the SML-QD formed with uniform base 3~4 nm and height ~5nm. Each individual dot shows almost ball shape geometry. But neighboring dots connect with each other, that may

cause in-plane quantum coupling, have effect to the in-plane discrete quantum confinement, cause weak normal incidence absorption. If keep optimizing the InAs thickness, spacer between InAs, growth condition, it is possible to grow ball shape SML-QD with small dot base, high dot density, and good uniformity.

4.4.5 Electro-optic Characterization of SML-QD Detectors
4.4.5.1 Polarized Spectral Response

For polarization dependent infrared spectral photoresponse measurements, the experimental setup schematic is shown as Figure. 4.22. The processed devices were polished with 45° side facet geometry, mounted on the 45° facet holder, wire-bonded on the pins of the leadless chip carrier (LCC), loaded in the cryostat with KBr window, and cooled at 77 Kelvin using liquid N_2. After the infrared radiation from Fourier Transform Infrared Spectroscopy (FTIR Nicolet 6700) passed through the polarizer, it is vertically incident upon the 45° side facet of the substrate and device, and follows the zigzag ray path in it. The 428 Current Amplifier is connected with the cryostat to add bias on the
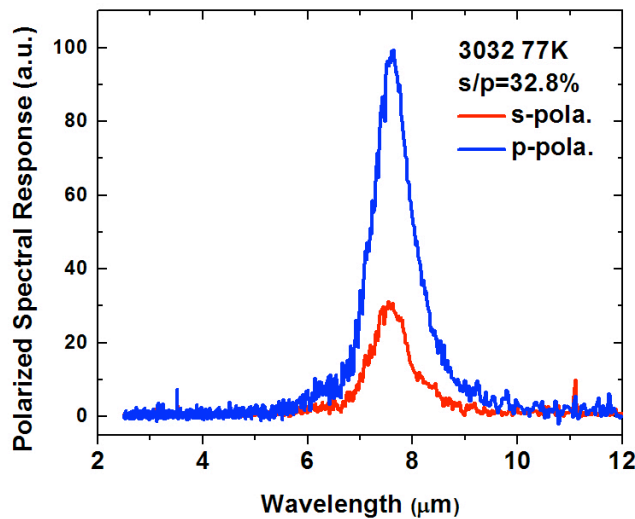
Figure 4.22: the s and p polarized spectral response of SML-QDs sample 3032

device and give output signal beck to FTIR and OMNIC software to measure the spectral photoresponse.

Figure 4.22 shows that the s-to-p ratio of polarized spectral response of 4 stacks of SML-QDs with In$_{.15}$Ga$_{.85}$As QW is increased as 33% compared with 2 stacks of SML-QD with GaAs QW as 9%. It indicates the InGaAs QW significantly prevents the Indium interface diffusion and decreases the dot base width. Even SML-QDs are connected with each other as shown of TEM image, the increased s-to-p ratio of polarized spectral response indicates that the performance of detector is QDIP rather than QWIP.

The in-plane (TE) quantum confinement and in-plane infrared absorption are dramatically improved compared to the vertical direction (TM). And the dot density is also increased. A strong spectral response not only describes the high material quality of QDs, such as low defect and low trap center, but also the improved discrete quantum confinement, and less intermixing and leakage path of the interface between QDs and surrounding QW materials.

4.4.5.2 Responsivity and Detectivity
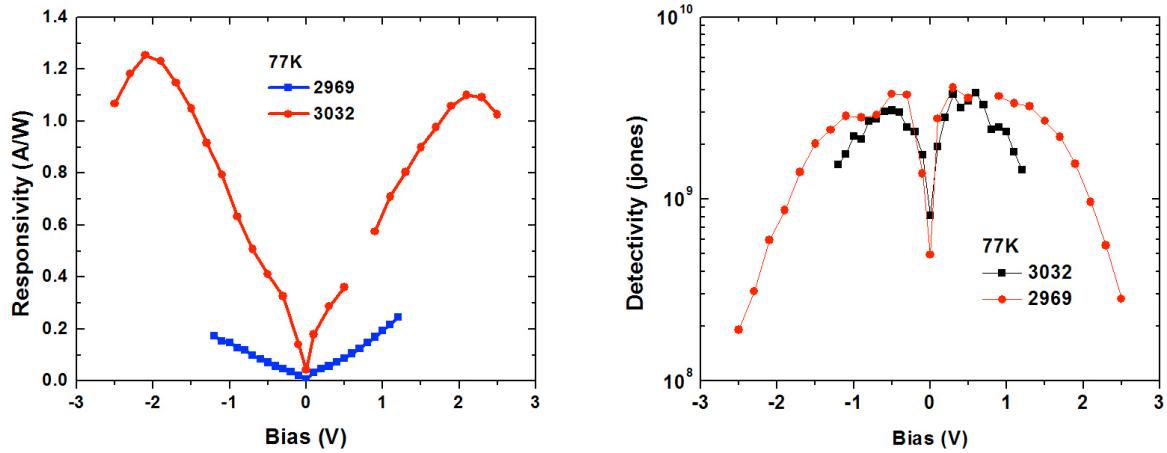
Figure 4.23 (a) shows the peak photoresponsivity R_i of #3032 and #2969 at 77 K as function of bias. (b) shows the peak Detectivity D of #3032 and #2969 at 77 K as function of bias.

110

Fig. 4.23 (a) shows the peak photoresponsivity R_i at 77 K as function of bias for SML-QD detector 3032 and SK-QD detector 2969. The highest R_i of 1.28 A/W was observed at 2.2 V at 77K for SML-QD detector, and it is 6 factor higher than the the highest R_i of SK-QD detector.

Fig. 4.23 (b) shows the peak Detectivity D at 77 K as function of bias for SML-QD detector 3032 and SK-QD detector 2969. At 77K, the highest D of 4×10^9 cmHz$^{1/2}$/W was observed at 0.4 V. Both of these two samples with EC-DWELL structure show the 2 to 3 order high detectivity compared with SML-QD without EC-DWELL design in section 4.2 and 4.3.

4.4.5.3 Photoconductive Gain

Figure 4.24. shows the photoconductive gain of #3032 as function of bias for 77K. From equation (2.12) the capture ability of QDIP is small as 1×10^{-4} to 1×10^{-3}, and the gain can reach to ~10. Both of them show the longer carrier lifetime of this QDIP, and it verifies the SML-QD techniques improves it. Since the capture ability is much less than 1 in these devices, as a good approximation, the photoconductive gain and the noise gain are equal in this device. The photoconductive gain of ~10 was observed as -2V 77K. The high gain indicates that this device is a QDIP rather than QWIP.
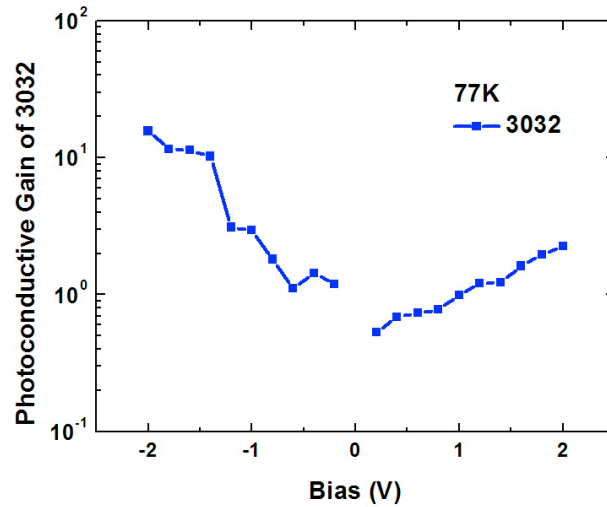
Figure 4.24 photoconductive gain of #3032 as function of bias for 77K and 90K

4.4.6 Conclusion

In section 4.4, we demonstrate the 4 stacks InAs/In$_{.15}$Ga$_{.85}$As SML-QD /enhanced confinement DWELL detector with increased s-to-p ratio of polarized spectral response as 33%. By engineering the dot geometry and quantum confinement, exploring InGaAs QW material combinations and growth condition, the SML-QD detector shows we have demonstrated a shape engineered QD detector with increased dot height to base ratio of ~1 compared to a conventional SK-QD detector with a ratio of 0.23. The change in the aspect ratio was monitored using TEM. We believe that the use of an In$_{.15}$Ga$_{.85}$As QW prevents the flattening of QDs by reducing the diffusion gradient. This is expected to increase the carrier relaxation time by providing 3D quantum mechanical confinement.

This QDIP shows the highest responsivity of 1.2 A/W at -2.2 V at 77K, and it is 6 time higher than the highest R_i of SK-QD detector under same CE-DWELL design and growth condition. This QDIP shows the highest D of 4×10^9 cmHz$^{1/2}$/W at 0.4 V 77K, and it is 2~3 order higher that SML-QD detector without CE-DWELL design. The photoconductive gain of ~10 was observed as -2V 77K.

CHAPTER 5 CONCLUSION AND FUTURE WORK

5.1 Conclusion

This work is focused on development of high performance mid-IR and long-IR SK-QD and SML-QD QDIP detectors. QDIP detector technology has inherent advantages over present-day detection technologies. Namely, the QDIP detectors are characterized by normal incident absorption, high operating temperature, low dark current, long carrier lifetime, mature GaAs epitaxial growth technology, and intermediate value and intermediate cost in the infrared detection market. In addition, adjustable bandgap of the QW provide tunable peak wavelength selection, and multicolor capacity of FPAs based on QDIPs. Moreover, by engineering the dot geometry and preventing the interface diffusion between the dot and QW, it is possible to improve the 3D quantum confinement, increase normal incident absorption, decrease interface leakage path and dark current, increase carrier lifetime, and reach the high operating temperature.

In Chapter 1 of this dissertation, we introduced the general concept of infrared detection. Detection principles, detector types (thermal and photon) were discussed. Pros and cons of competitive infrared technologies (based on MCTs, bulk InSb, type II InAs/InSb superlattice and QWIPs) were described and alternative technology for QDIP detection was introduced. Finally, the SK-QD shape flattening and the interface diffusion during the subsequent epitaxial growth were described as the key issue in this dissertation.

In Chapter 2 we described variety of characterization techniques utilized in this work. To thoroughly understand operation principle of device and be able to design detectors with required characteristics as much as possible information about material and detector properties have to be available, beginning with parameters of as-grown material and ending with characteristics of detector performance. We characterized structural, optical and morphological properties of as-grown material by Photoluminescence, AFM, TEM/STEM, XRD and polarized spectral response techniques, respectively. The electrical behavior of processed detectors was investigated by current-voltage measurements. Detector performance also was characterized by spectral response ,responsivity and detectivity measurements.

In Chapter 3, we demonstrate the improvement in the operating temperature and the s-to-p ratio of the polarized spectral response in an engineered Stranski-Krastanov DWELL based infrared photodetector. This improvement was achieved through engineering the dot geometry and the quantum confinement via post growth capping of the QD with select overlying materials under various growth conditions. The effect of the capping procedures was determined by examining the optical properties of the QDs such as photoluminescence and the s-to-p ratio of the polarized spectral response in the QDIP detector, and structural properties of the QDs such as AFM and TEM.

The results show the InAs QD with the $In_{.15}Al_{.1}Ga_{.75}As$ quaternary well has the best over all performance. By examining the dot geometry using TEM, the TEM image shows a quantum dot with a reduced base of 12 nm and an increased height of 8 nm, therefore the dot height to base aspect ratio is reached to 0.67, which is much higher than the conventional SK dot with the aspect ratio of 0.25 (with height 4 nm/ base 20 nm).

The ratio of s-polarization (TE) to p-polarization (TM) 45° facet side incidence spectral photoresponse increases to 37% from 10% in a DWELL based infrared photodetector.

These engineered QDs in a Well were then introduced into the active region of a DWELL IR photodetector. The infrared photodetector shows the highest operating temperature is increased to 250K, the peak photodetectivity of 1×10^9 cmHz$^{1/2}$/W at 77K for a peak wavelength of 4.8 μm, and 7.2×10^7 cmHz$^{1/2}$/W at 250K for a peak wavelength of 3.2 μm. The dark current density is as low as 6.3×10^{-7}A/cm^2 (V_b=7V) and 2×10^{-4} A/cm^2 (V_b=12V) at 77 K, and the photocurrent gain is 100 (V_b=12V) at 77 K.

In chapter 4 we demonstrate the optimization of the growth condition of the Sub-Monolayer QD QDIP detectors. Compared with "dome-shaped" SK QDs, the "cylinder-shaped" SML QDs has advantages including small base diameter, better 3-D quantum confinement, high dot density, adjustable height of the dot geometry, tailorable aspect ratio, and the absence of the wetting layer.

The optimization is based on three heterostructure designs demonstrated in section 4.2, 4.3 and 4.4.

In section 4.2, the InAs/InGaAs SML QDs were formed using 2 layers of 0.5 ML InAs evenly embedded in 5.1 nm GaAs quantum well. The growth condition of the SML

QDs with the V/III flux rate ratio as 30, growth rate as InAs- 0.159 ML/s and GaAs-0.787 ML/s, 10 sec interruption both before and after InAs deposition have been selected. The growth temperature is adjusted from 460 °C to 540 °C. The growth temperature has the effect to the Indium interface diffusion, dot geometry, 3D quantum confinement, strain model in whole system. From the PL spectra results, the ground state of SML-QD is energetically close to the GaAs:Si energy, the dot grown at 640 °C has the strongest PL intensity.

By examining the dot geometry using TEM, the SML-QD grown at 480 °C has the small base diameter as 6 nm, which grown at 540 °C has the large base diameter as 30 nm. The XRD RADS simulation shows the structural property of this detector is similar to a QWIP.

The results of the s/p polarization spectral response ratio and the dot geometry height to base aspect ratio are corroborated each other. The SML-QD detector grown at 480 °C has the small base diameter as 6 nm, and has the highest s/p ratio as 9% in this study. The SML-QD detector grown at 540 °C has the large base diameter as 30 nm, and has the low s/p ratio less than 1%.

At 77K, #2916 (grown at 540 °C) was observed with the highest R_i of 0.40 A/W, and the highest D of 5×10^8 cmHz$^{1/2}$/W 0.40 at 0.25 V for a peak wavelength of 10.5 μm. The high growth temperature involves the high crystal quality, low defect density, and improved optical absorption, even the dot has large base diameter, heavy interface diffusion between dot and the surrounding QW material. So our future work is to product the SML-QD with small base diameter, low interface diffusion under high growth temperature.

In section 4.3, we have demonstrated the SML-QD with In$_{.1}$Ga$_{.9}$As QW improved quantum confinement due to the In$_{.1}$Ga$_{.9}$As QW significantly preventing the Indium diffusion. The InAs/InGaAs SML QDs were formed using 2 layers of 0.5 ML InAs evenly embedded in 5.1 nm In$_{.1}$Ga$_{.9}$As quantum well. This QDIP shows strong bound-to-bound intersubband transition at 10.2 μm from 77K to 90K. The highest responsivity of 0.10 A/W was observed at -1.60 V at 77K, and the highest R_i of 0.10 A/W was observed at -0.5V at 90K. At 77K, the highest D of 6×10^7 cmHz$^{1/2}$/W was observed at 0.6 V. At

90K, the highest D of 2×10^7 cmHz$^{1/2}$/W was observed at 0.6 V. The photoconductive gain of ~20 was observed as 1.6V 77K, and of ~40 was observed as 1.4V 90K.

In section 4.4, we demonstrate the 4 stacks InAs/In$_{.15}$Ga$_{.85}$As SML-QD /enhanced confinement DWELL detector with increased s-to-p ratio of polarized spectral response as 33%. The InAs/InGaAs SML QDs were formed using 4 layers of 0.3 ML InAs evenly embedded in 5.1 nm In$_{.15}$Ga$_{.85}$As quantum well. By engineering the dot geometry and quantum confinement, exploring InGaAs QW material combinations and growth condition, the SML-QD detector shows small base width as 4nm and height as 5nm, and the increased s/p ratio of polarized spectral response as 33%. We believe that the use of an In$_{.15}$Ga$_{.85}$As QW prevents the flattening of QDs by reducing the diffusion gradient. This is expected to increase the carrier relaxation time by providing 3D quantum mechanical confinement.

This QDIP shows the highest responsivity of 1.2 A/W at -2.2 V at 77K, and it is 6 factor higher than the highest R_i of SK-QD detector under same EC-DWELL design and growth condition. This QDIP shows the highest D of 4×10^9 cmHz$^{1/2}$/W at 0.4 V 77K, and it is 2~3 order higher that SML-QD detector without EC-DWELL design demonstrated in section 4.1 and 4.2. The photoconductive gain of ~10 was observed as -2V 77K.

5.2 Future work

Sub-monolayer QD QDIP is a new promising detection technology in the recent years, physics of this material system was not understood completely yet. Several issues requiring attention are:

• Detector structure optimization

1. Selective quantum well material

Based on the results in chapter 6, our future work is to product the SML-QD with small base diameter, low interface diffusion and high crystal quality. Use InGaAs or InAlGaAs as QW to surround the InAs deposition will dramatically satisfied above acquirement due to the low interfacial-strain, mechanical diffusion barrier, and chemical diffusion retardant.

2. Engineering the band energy level of QW and barrier.

Based on the introduction in chapter 1, our future work is to involve various types of band energy engineering to decrease dark current, improve quantum confinement, product high performance, multi-spectral MWIR and LWIR for the 3rd generation FPA application.

- Growth condition optimization

Start with a new design and good PL spectra, we can optimize the growth condition one by one in the future. That including:

1. Growth temperature
2. III/V BEP flux ratio
3. Growth rate
4. Si dopping level at the InAs deposition materials

Since SML-QDs have advantages including small base diameter, better three-dimensional quantum confinement, large dot density, tailorable aspect ratio, and absence of the wetting layer, through optimizing the structure design and the growth condition, it is possible to product a SML-QD QDIP with improved normal incident absorption and the s-to-p ratio of the polarized spectral response larger than 1.

REFERENCES

Chapter 1 Reference:

[1] http://en.wikipedia.org/wiki/File:Infrared_spectrum.gif, Clemente Ibarra-Castanedo at Canada Research Chair in Multipolar Infrared Vision – MiViM

[2] http://commons.wikimedia.org/wiki/File:BlackbodySpectrum_loglog_150dpi_en.png

[3] http://en.wikipedia.org/wiki/Planck's_law

[4] http://en.wikipedia.org/wiki/Black_body

[5] Antoni Rogalski, 2011, Infrared Detectors, 2nd edition, CRC Press, Taylor & Francis Group, page 3.

[6] A. Rogalski, J. Antoszewski, and L. Faraone, "Third-generation infrared photodetector arrays" J. Appl. Phys. 105, 091101 (2009).

[7] D. Reago, S. Horn, J. Campbell, and R. Vollmerhausen, "Third generation imaging sensor system concepts", SPIE, 3701, 108–117 (1999).

[8] I. Vurgaftman, J.R. Meyer, and L.R. Ram-Mohan, "Band parameters for III-V compound semiconductors and their alloys," J. Appl. Phys. Vol. 89, Vol. 11, 5815, (2001).

[9] Gopal, V. 1998. Key issues of HgCdTe hybrid focal plane array technology. In Physics of Semiconductor Devices; Kumar, V. and Agarwal, S.K., Eds.; Norosa Publishing House: India, 729–737.

[10] A. Rogalski, Infrared detectors at the beginning of the next millennium, Proc. SPIE,

4413: 307–322. (2011).

[11] J.D. Vincent. "Fundamentals of Infrared Detector Operation and Testing". John Wiley and Sons Inc., New York, 1990. p.439

[12] S.D. Gunapala, S.V. Bandara, J.K. Liu, J.M. Mumolo, D.Z. Ting, C.J. Hill, J. Nguyen, B. Simolon, J. Woolaway, S.C. Wang, Li Weiping, P.D. LeVan, M.Z. Tidrow, Demonstration of Megapixel Dual-Band QWIP Focal Plane Array, IEEE Journal of Quantum Electronics, Volume: 46 Issue:2 page(s): 285 – 293 Feb. 2010

[13] Gail J. Brown, "Type-II InAs/GaInSb Superlattices for Infrared Detection: an Overview" Infrared Technology and Applications XXXI, Proc. of SPIE Vol. 5783 SPIE, Bellingham, WA, (2005)

[14] N. W. Ashcroft, N. D. Mermin, Solid State Physics, Thomson Learning, Inc, USA, first edition (1976).

[15] Bockelmann U and Bastard G. Phonon scattering and energy relaxation in two-, one, and zero-dimensional electron gases. Physical Review B 1990; 42: 8947-51

[16] Benisty H, Sotomayor-Torres CM and Weisbuch C. Intrinsic mechanism for the poor luminescence properties of quantum-box systems. Physical Review B 1991; 44: 10945-8

[17] Bhattacharya P, Kamath KK, Singh J et al.. In(Ga)As/GaAs self-organized quantum dot lasers: DC and small-signal modulation properties. IEEE Transactions on Electron Devices 1999; 46: 871-83

[18] Ohnesorge B, Albrecht M, Oshinowo J and Forchel A. Rapid carrier relaxation in self assembled InxGa1-xAs/GaAs quantum dots. Physical Review B 1996; 54: 11532-8

119

[19] Mukai K, Ohtsuka N, Shoji H and Sugawara M. Phonon bottleneck in self-formed InxGa1-xAs/GaAs quantum dots by electroluminescence and time-resolved photoluminescence. Physical Review B 1996; 54: R5243-R6

[20] Klotzkin D, Kamath K and Bhattacharya P. Quantum capture times at room temperature in high-speed In0.4Ga0.6As-GaAs self-organised quantum-dot lasers. IEEE Photonics Technology Letters 1997; 9: 1301-3

[21] Urayama J, Norris TB, Singh J and Bhattacharya P. Observation of phonon bottleneck in quantum dot electronic relaxation. Physical review Letters 2001; 86: 4930-3

[22] Klotzkin D and Bhattacharya P. Temperature dependence of dynamic and DC characteristics of quantum-well and quantum-dot lasers: a comparative study. Journal of Lightwave Technology 1999; 17: 1634-4

[23] D. Bimberg, M. Grundmann, and N. N. Ledentsov, Quantum Dot Heterostructures, John Wiley & Sons, 1998.

[24] M. Sugarawa, Ed., Self-assembled InGaAs/GaAs quantum dots, Academic Press, 1999.

[25] V. A. Shchukin, N. N. Ledentsov, and D. Bimberg, Epitaxy of nanostructures, Springer Verlag, 2004.

[26] J. Stangl, V. Holy, and G. Bauer, Structural properties of self-organized semiconductor nanostructures, Rev. Mod. Phys. 76, 725 (2004).

[27] N. W. Ashcroft, N. D. Mermin, Solid State Physics, Thomson Learning, Inc, USA, first edition (1976).

[28] P. Martyniuk, S. Krishna, and A. Rogalski, "Assessment of quantum dot infrared photodetectors for high temperature operation," Journal of Applied Physics, vol. 104, no. 3, p. 034314, 2008.

[29] W. Zhang, H. Lim, M. Taguchi, S. Tsao, B. Movaghar, and M. Razeghi, "High detectivity InAs quantum-dot infrared photodetectors grown on InP by metal–organic chemical–vapor deposition," Applied Physics Letters, vol. 86, no. 19, p. 191103, 2005.

[30] Andrea Lenz, Atomic structure of capped In(Ga)As and GaAs quantum dots for optoelectronic devices, Ph. D. Dissertation, Institut für Festkörperphysik, page 78, 11. February 2008

[31] H C Liu, Quantum dot infrared photodetector, Opto-Electronics Review 11(1), 1-5 (2003).

[32] F. Hopfer, A. Mutig, M. Kuntz, G. Fiol, D. Bimberg, N. N. Ledentsov, V. A. Shchukin, S. S. Mikhrin, D. L. Livshits, I. L. Krestnikov, A. R. Kovsh, N. D. Zakharov, and P. Werner, Single-mode submonolayer quantum-dot vertical-cavity surface-emitting lasers with high modulation bandwidth, Appl. Phys. Lett. 89, 141106 (2006)

[33] Germann, T. D. Strittmatter, A. Pohl, J. Pohl, U. W. Bimberg, D. Rautiainen, J. Guina, M. Okhotnikov, O. G. High-power semiconductor disk laser based on InAs/GaAs submonolayer quantum dots, Appl. Phys. Lett. 92, 101123 (2008)

[34] Ting, David Z.-Y. Bandara, Sumith V. Gunapala, Sarath D. Mumolo, Jason M. Keo, Sam A. Hill, Cory J. Liu, John K. Blazejewski, Edward R. Rafol, Sir B. Chang, Yia-Chung, Submonolayer quantum dot infrared photodetector, Appl. Phys. Lett. 94, 111107 (2009)

[35] J. Phillips, "Evaluation of the fundamental properties of quantum dot infrared detectors," Journal of Applied Physics, vol. 91, no. 7, pp. 4590–4594, 2002.

[36] P. Martyniuk, S. Krishna, and A. Rogalski, "Assessment of quantum dot infrared photodetectors for high temperature operation," Journal of Applied Physics, vol. 104, no. 3, p. 034314, 2008.

[37] W. Zhang, H. Lim, M. Taguchi, S. Tsao, B. Movaghar, and M. Razeghi, "High detectivity InAs quantum-dot infrared photodetectors grown on InP by metal–organic chemical–vapor deposition," Applied Physics Letters, vol. 86, no. 19, p. 191103, 2005.

[38] A. Stintz, G. T. Liu, A. L. Gray, R. Spillers, S. M. Delgado, and K. J. Malloy, "Characterization of InAs quantum dots in strained $In_xGa_{1-x}As$ quantum wells," vol. 18, no. 3. JVST B, 2000, pp. 1496– 1501.

[39] E.-T. Kim, Z. Chen, and A. Madhukar, "Tailoring detection bands of InAs quantum-dot infrared photodetectors using $In_xGa_{1-x}As$ strain-relieving quantum wells," Applied Physics Letters, vol. 79, no. 20, pp. 3341–3343, 2001.

[40] Z. Chen, O. Baklenov, E. T. Kim, I. Mukhametzhanov, J. Tie, A. Madhukar, Z. Ye, and J. C. Campbell, "Normal incidence $InAs/Al_xGa_{1-x}As$ quantum dot infrared photodetectors with undoped active region," Journal of Applied Physics, vol. 89, no. 8, pp. 4558–4563, 2001.

[41] K. Stewart, M. Buda, J. Wong-Leung, L. Fu, C. Jagadish, A. Stiff-Roberts, and P. Bhattacharya, "Strain relaxation in rapid thermally annealed InAs/GaAs quantum dot infrared photodetectors," Optoelectronic and Microelectronic Materials and Devices, 2002 Conference on, pp. 475–478, Dec. 2002.

[42] E. C. Le Ru, P. Howe, T. S. Jones, and R. Murray, "Strain-engineered InAs/GaAs quantum dots for long-wavelength emission," Phys. Rev. B, vol. 67, no. 16, p. 165303, Apr 2003.

[43] L. Fu, H. H. Tan, I. McKerracher, J. Wong-Leung, C. Jagadish, N. Vukmirovi´c, and P. Harrison, "Effects of rapid thermal annealing on device characteristics of InGaAs/GaAs quantum dot infrared photodetectors," Journal of Applied Physics, vol. 99, no. 11, p. 114517, 2006.

[44] J. Shao, T. Vandervelde, W.Y. Jang, A. Stintz, and S. Krishna, "High operating temperature InAs quantum dot infrared photodetector via selective capping techniques," Nanotechnology, 2008. NANO '08. 8th IEEE Conference on, pp. 112–115, Aug. 2008.

[45] S. Chakrabarti, A. Stiff-Roberts, P. Bhattacharya, S. Gunapala, S. Bandara, S. Rafol, and S. Kennerly, "High-temperature operation of InAs/GaAs quantum-dot infrared photodetectors with large responsivity and detectivity," Photonics Technology Letters, IEEE, vol. 16, no. 5, pp. 1361–1363, May 2004.

[46] Z. Ye, J. Campbell, Z. Chen, O. Baklenov, E. Kim, I. Mukhametzhanov, J. Tie, and A. Madhukar, "High-performance InAs/GaAs quantum dots infrared photodetector with/without $Al_{0.2}Ga_{0.8}As$ blocking layers," Materials Research Society Symposiam Proceedings, vol. 692, p. H.9.17.1, 2002.

[47] H. S. Ling, S. Y. Wang, C. P. Lee, and M. C. Lo, "High quantum efficiency dots-in-a-well quantum dot infrared photodetectors with AlGaAs confinement enhancing layer," Applied Physics Letters, vol. 92, no. 19, p. 193506, 2008.

[48] A. Stintz, G. T. Liu, A. L. Gray, R. Spillers, S. M. Delgado, and K. J. Malloy, "Characterization of InAs quantum dots in strained $In_xGa_{1-x}As$ quantum wells," vol. 18, no. 3. JVST B, 2000, pp. 1496– 1501.

[49] J. D. Phillips "Evaluation of the fundamental properties of quantum dot infrared detectors", J. Appl. Phys., vol. 91, p.4590 , 2002.

[50] S. Raghavan, D. Forman, P. Hill, N. R. Weisse-Bernstein, G. von Winckel, P.

Rotella, and S. Krishna, Normal-incidence InAs/In$_{0.15}$Ga$_{0.85}$As quantum dots-in-a-well detector operating in the long-wave infrared atmospheric window (8–12 μm). J. Appl. Phys. 96, 1036 (2004);

[51] Sanjay Krishna, Quantum dots-in-a-well infrared photodetectors, J. Phys. D: Appl. Phys. 38 (2005) 2142–2150

[52] R. V. Shenoi, J. Hou, Y. Sharma, J. Shao, T. E Vandervelde, and S. Krishna, Low strain Quantum Dots in a Double Well Infrared Detectors, Proc. of SPIE Vol. 7082 708207-1 2008.

[53] Z. Ye, J. Campbell, Z. Chen, O. Baklenov, E. Kim, I. Mukhametzhanov, J. Tie, and A. Madhukar, "High-performance InAs/GaAs quantum dots infrared photodetector with/without Al$_{0.2}$Ga$_{0.8}$As blocking layers," Materials Research Society Symposium Proceedings, vol. 692, p. H.9.17.1, 2002.

[54] P. Bhattacharya, X. H. Su, S. Chakrabarti, G. Ariyawansa, and A. G. U. Perera, "Characteristics of a tunneling quantum-dot infrared photodetector operating at room temperature," Applied Physics Letters, vol. 86, no. 19, p. 191106, 2005.

[55] A. V. Barve, S. Y. Shah, J. Shao, T. E. Vandervelde, R. V. Shenoi, W.-Y. Jang, and S. Krishna, "Reduc- tion in dark current using resonant tunneling barriers in quantum dots-in-a-well long wavelength infrared photodetector," Applied Physics Letters, vol. 93, no. 13, p. 131115, 2008.

[56] G. Ariyawansa, V. Apalkov, A. G. U. Perera, S. G. Matsik, G. Huang, and P. Bhattacharya, Bias-selectable tricolor tunneling quantum dot infrared photodetector for atmospheric windows, APPLIED PHYSICS LETTERS 92, 111104 2008

Chapter 2 Reference:

[1] A. Cho, "Film Deposition by Molecular Beam Techniques," J. Vac. Sci. Tech., Vol. 8, pp. S31-S38, 1971.

[2] A. Cho, J. Arthur, "Molecular Beam Epitaxy," Prog. Solid-State Chem., Vol. 10, pp. 157-192, 1975.

[3] M. Ohring, The Material Science of Thin Films, Academic Press, 1992.

[4] J. Harris, B. Joyce, P. Dobson, "Oscillations in the Surface Structure of Sn-Doped GaAs During Growth by MBE," Surf. Sci., Vol. 103, pp.L90-L96, 1981.

[5] J. Neave, B. Joyce, P. Dobson, N. Norton, "Dynamics of Film Growth of GaAs by MBE from RHEED Observations," Appl. Phys. A, Vol. 31, pp.1-8, 1983.

[6] P. Cohen, P. Pukite, J. van Hove, C. Lent, "Reflection High Energy Electron Diffraction Studies of Epitaxial Growth on Semiconductor Surfaces," J. Vac. Sci. Tech. B, Vol. 3, pp. 1251-1258, 1986.

[7] T. Block, K. Eyink, D. Neikirk, B. Streetman, "Diffraction Condition Dependence of RHEED Dampening During MBE Growth," SPIE Proceedings, Epitaxial Growth Processes, Vol. 2140, pp. 10-24, 1994.

[8] Robert A. Wilson and Heather A. Bullen, Introduction to Scanning Probe Microscopy (SPM)-Basic Theory Atomic Force Microscopy (AFM), Creative Commons Attribution-Noncommercial-Share Alike 2.5 License

[9] http://www.team-nanotec.de/

[10] J.-Y. Duboz, H. C. Liu, Z. R.Wasilewski, M. Byloss, and R. Dudek, "Tunnel current in quantum dot infrared photodetectors," Journal of Applied Physics, vol. 93, no. 2, pp. 1320–1322, 2003.

[11] U. Bockelmann and G. Bastard, "Phonon scattering and energy relaxation in two-, one-, and zero-dimensional electron gases," Phys. Rev. B, vol. 42, pp. 8947–8951, 1990.

[12] X. Lu, J. Vaillancourt, M. J. Meisner, "Temperature-dependent photoresponsivity and high-temperature (190K) operation of a quantum-dot infrared photodetector," Accepted for publication, Appl. Phys. Lett. (2007).

[13] P. Aivaliotis, S. Menzel, E. A. Zibik, J. W. Cockburn, L. R. Wilson, and M. Hopkinson, Energy level structure and electron relaxation times in InAs/In$_x$Ga$_{1-x}$As quantum dot-in-a-well structures Applied Physics Letters, 91, 253502, (2007).

[14] J. M. García, G. Medeiros-Ribeiro, K. Schmidt, T. Ngo, J. L. Feng, A. Lorke, J. Kotthaus, and P. M. Petroff, ntermixing and shape changes during the formation of InAs self-assembled quantum dots Appl. Phys. Lett. 71, 2014 (1997).

[15] J. Shao, T. Vandervelde, W. Jang, A. Stintz, and S. Krishna, High operating temperature InAs quantum dot infrared photodetector via selective capping techniques 8th IEEE Conference on Nanotechnology, (2008).

[16] H C Liu, Quantum dot infrared photodetector, Opto-Electronics Review 11(1), 1-5 (2003).

[17] R Attaluriand, S Krishna, M Matthews, R Steed, M Frogley and C Phillips, Transient photoconductivity measurements of carrier lifetimes in an InAs/In0.15Ga0.85As dots-in-a-well detector Appl. Phys. Lett. 90, 103519(2007).

[18] B. F. Levine, Quantum-well infrared photodetectors, J. Appl. Phys. 74, R1 (1993).

[19] H.C. Liu, Noise gain and operating temperature of quantum well infrared photodetectors.Appl. Phys. Lett., 61, 2703(1992).

[20] W.A. Beck, Photoconductive gain and generation-recombination noise in multiple-quantum-well infrared detectors, Appl. Phys. Lett., 63, 3589(1993).

[21] Michael A. Kinch, Fundamentals of Infrared Detector Materials, SPIE 2007, P6

Chapter 3 Reference:

[1] K. Stewart, M. Buda, J. Wong-Leung, L. Fu, C. Jagadish, A. Stiff-Roberts, and P. Bhattacharya, "Strain relaxation in rapid thermally annealed InAs/GaAs quantum dot infrared photodetectors," Optoelectronic and Microelectronic Materials and Devices, 2002 Conference on, pp. 475–478, Dec. 2002.

[2] T.E. Vandervelde, K. Sun, J. Merz, A.J. Kubis, R. Hull, and J.C. Bean, The effect of two-temperature capping on germanium/silicon quantum dots and analysis of superlattices so composed, J. Appl. Phys. Lett., 99, 124301 (2006).

[3] Nobuyuki Takeyasu[a], Hajime Asahi[a], Soon Jae Yu[a], Kumiko Asami[a], Tadaaki Kaneko[a] and Shun-ichi Gonda, Gas source MEE (migration enhanced epitaxy) growth of InP, Journal of Crystal Growth, Vol. 111, Issues 1-4, (1991).

[4] R Attaluria, S Krishna, M Matthews, R Steed, M Frogley and C Phillips, Transient photoconductivity measurements of carrier lifetimes in an InAs/In0.15Ga0.85As dots-in-a-well detector Appl. Phys. Lett. 90, 103519(2007).

[5] S. Krishna, S. Raghavan "Characterization of rapid-thermal-annealed InAs/In$_{0.15}$Ga$_{0.85}$As dots-in-well heterostructure using double crystal x-ray diffraction and photoluminescence" Appl. Phys. Lett., vol. 80, No. 21 pp. 3898–3900, May. 2002.

[6] H. C. Liu, C. Y. Song, A. Shen, M. Gao, Z. R. Wasilewski, and M. Buchanan, "GaAs/AlGaAs quantum-well photodetector for visible and middle infrared dual-band detection," Applied Physics Letters, vol. 77, no. 16, pp. 2437–2439, 2000.

[7] B. F. Levine, "Quantum-well infrared photodetectors," Journal of Applied Physics, vol. 74, no. 8, pp. R1–R81, 1993.

[8] Vines, P.; Tan, C.H.; David, J.P.R.; Attaluri, R.S.; Vandervelde, T.E.; Krishna, S.; Jang, W.Y.; Hayat, M.M.; Low strain multiple stack quantum dot infrared photodetectors for multispectral and high resolution hyperspectral imaging, IEEE LEOS Annual Meeting Conference Proceedings, 2009. LEOS '09. Oct. 2009

[9] J. M. García, G. Medeiros-Ribeiro, K. Schmidt, T. Ngo, J. L. Feng, A. Lorke, J. Kotthaus, and P. M. Petroff, Intermixing and shape changes during the formation of InAs self-assembled quantum dots, Appl. Phys. Lett. 71, 2014 (1997).

[10] J. Shao, T. Vandervelde, A Barve, W. Jang, A. Stintz, and S. Krishna, Enhanced normal incidence photocurrent in quantum dot infrared photodetectors, J. Vac. Sci. Technol. B 29,,3., May/Jun 2011

[11] H C Liu, Quantum dot infrared photodetector", Opto-Electronics Review 11(1), 1-5 (2003).

[12] A. M. Sanchez, R. Beanland, N. F. Hasbullah, M. Hopkinson, and J. P. R. David, J. Appl. Phys. 106, 024502 (2009).

[13] S. Chakrabarti, A. D. Stiff-Roberts, P. Bhattacharya, Fellow, IEEE, S. Gunapala, S. Bandara, S. B. Rafol, and S. W. Kennerly, High-Temperature Operation of InAs–GaAs Quantum-Dot Infrared Photodetectors With Large Responsivity and Detectivity, IEEE PHOTONICS TECHNOLOGY LETTERS, VOL. 16, NO. 5, MAY 2004

[14] Ling, H. S.; Wang, S. Y.; Lee, C. P.; Lo, M. C. Confinement-enhanced dots-in-a-well QDIPs with operating temperature over 200 K, Infrared Physics & Technology, Volume 52, Issue 6, p. 281-284. 2009

[15] Jarrod Vaillancourt, Andreas Stintz, Mark J. Meisner and Xuejun Lu, Low-bias, high-temperature operation of an InAs–InGaAs quantum-dot infrared photodetector with peak-detection wavelength of 11.7 μm, Infrared Physics & Technology Volume 52, Issue 1, January 2009,

[16] H. Lim, S. Tsao, W. Zhang, and M. Razeghia High-performance InAs quantum-dot infrared photodetectors grown on InP substrate operating at room temperature APPLIED PHYSICS LETTERS 90, 131112 2007

Chapter 4 Reference:

[1] F. Hopfer, A. Mutig, M. Kuntz, G. Fiol, D. Bimberg, N. N. Ledentsov, V. A. Shchukin, S. S. Mikhrin, D. L. Livshits, I. L. Krestnikov, A. R. Kovsh, N. D. Zakharov, and P. Werner, Single-mode submonolayer quantum-dot vertical-cavity surface-emitting lasers with high modulation bandwidth, Appl. Phys. Lett. 89, 141106 (2006).

[2] Germann, T. D. Strittmatter, A. Pohl, J. Pohl, U. W. Bimberg, D. Rautiainen, J. Guina, M. Okhotnikov, O. G. High-power semiconductor disk laser based on InAs/GaAs submonolayer quantum dots, Appl. Phys. Lett. 92, 101123 (2008).

[3] Ting, David Z.-Y. Bandara, Sumith V. Gunapala, Sarath D. Mumolo, Jason M. Keo, Sam A. Hill, Cory J. Liu, John K. Blazejewski, Edward R. Rafol, Sir B. Chang, Yia-Chung, Submonolayer quantum dot infrared photodetector, Appl. Phys. Lett. 94, 111107 (2009)